



Universität des Saarlandes
DISSERTATION

*Design of steel surface and
wetting properties by laser
patterning*

zur Erlangung des Grades des Doktors der Ingenieurwissenschaften der
Naturwissenschaftlich-Technischen Fakultät III Chemie, Pharmazie, Bio-
und Werkstoffwissenschaften der Universität des Saarlandes

von

Brice Raillard

Saarbrücken
2013

Tag des Kolloquiums: 06.06.2014

Dekan: Prof. Dr. Volkhard Helms, Universität des Saarlandes

Berichterstatter: Prof. Dr.-Ing. Frank Mücklich, Universität des Saarlandes

Prof. Dr.-Ing. Dirk Bähre, Universität des Saarlandes

Vorsitzende: Prof. Dr. rer.nat. Wulff Possart, Universität des Saarlandes

Akad. Mitarbeiter: Dr. Frank Aubertin, Universität des Saarlandes

Contents

Acknowledgments	6
Abstract	9
Zusammenfassung	10
Symbols and acronyms	12
1 Introduction	14
1.1 Motivation	14
1.2 Tasks of this work	16
2 State of the art and theoretical considerations: Laser and Wetting	18
2.1 Laser patterning: laser systems, modes, effects and applications	18
2.1.1 Laser systems: femtosecond versus nanosecond laser . .	18
2.1.2 Laser ablation mode	21
2.1.3 Continuous wave laser	33
2.1.4 Laser interference	35
2.2 Wetting phenomena and wettability: influences of the surface and fluid properties	49
2.2.1 Wettability models: Young, Wenzel, Cassie Baxter, de Gennes	49
2.2.2 Wetting on chemical surfaces	58
2.2.3 Wetting on textured surfaces	60
2.2.4 Effects of fluid properties	61
3 Experimental	62
3.1 Materials	62
3.1.1 100Cr6 steel, metallographic preparation	62
3.1.2 Fluids	63
3.2 Laser	63

3.2.1	Nanosecond Nd:YAG laser	63
3.2.2	Femtosecond Ti:sapphire laser	65
3.3	Characterization techniques	66
3.3.1	White light interferometer	66
3.3.2	FIB/SEM Dual beam workstation	67
3.3.3	X-ray photoelectron spectrometer	67
3.3.4	Raman spectrometer	68
3.3.5	Atom probe tomography	68
3.3.6	Transmission electron microscopy	68
3.3.7	Contact angle	69
4	Femtosecond laser structures	71
4.1	Results	71
4.1.1	Topographical analyses	71
4.1.2	Chemical analyses	77
4.1.3	Wetting properties	89
4.2	Discussion	92
4.2.1	Topographical analyses	92
4.2.2	Chemical analyses	94
4.3	Conclusions	98
5	Nanosecond laser structures	99
5.1	Results	99
5.1.1	Topographical analyses	99
5.1.2	Chemical analyses	101
5.1.3	Wetting properties	102
5.2	Discussion	108
5.2.1	Chemical analyses	108
5.2.2	Topographical analyses	108
5.2.3	Simulation analyses	110
5.3	Conclusions	113

6	Optimized structures: femto- and nanosecond structure combination	114
6.1	Results	114
6.1.1	Topographical analyses	114
6.1.2	Wetting properties	116
6.2	Discussion	118
6.3	Conclusions	121
7	Conclusions and outlook	122
7.1	Conclusions	122
7.2	Outlook	125

Acknowledgments

I would like to acknowledge the following persons for their help, advices and precious supports.

First, I would like to sincerely thank **Professor Frank Mücklich** for giving me the opportunity to successfully lead this thesis and to enhance my researches in such an interesting field. Then, I would like to acknowledge him for his precious and rich scientific supervision and finally his infinite, and doubtless trust in my qualities and abilities.

I sincerely acknowledge **Professor Dirk Bähre** for accepting the revision of this thesis and his precious and friendly collaboration as EEIGM coordinator.

My next sincere thanks go to **Doctor Carsten Gachot** and **Doctor Esteban Ramos-Moore** from the Universität des Saarlandes and Universidad Católica de Chile, respectively. They had the kindness and patience to help me for the publications and revisions of my work and advising me as colleagues and friends.

I thank **all my colleagues** from the chair of Functional Materials since my start in Saarbrücken in 2007 and especially my colleagues and friends **Mariela D'Alessandria, Agustina Guitar, Rodolphe Catrin, Michael Hans, Nicolas Jeanvoine, Flavio Soldera, Nicolas Souza** and **Sebastian Suarez** for their precious helps, corrections and advices.

I acknowledge **Doctor Frank Müller** and **Samuel Grandthyll** from the chair of Experimental Physics (Universität des Saarlandes), **Doctor David Horwat, Sylvie Migot-Choux** from the Institut Jean Lamour (Nancy) and **Lucille Gouton** and **Justine Remond**, the students that I supervised, for their contributions to this thesis.

I would also like to thank **Jennifer Collet** for her friendly help in proof reading of this thesis and **Julien Lacava** for his precious IT-help and the good times we had together each Monday and certain week-ends on the different "fields".

I am grateful to my friends **Flore, Charlotte, Céline, Nuria, Noémie, Ludo, Nico, Amaury, Bebert, Clem, JB, Hak, Julien, Michel, Max, Wiktor, Stéphane, Lluís, Guillaume, Daniel, Dominik** for the good moments together and their friendship.

I would like to thank **my family: Cécé, Man, Tach, Julien, Zbe, Martin, Francine, Antoine**, who supported me during all this time and especially my parents **Christiane** and **Francis**.

Finally, I am infinitely grateful to **Jo**, who highlights my life, for her support, faith and love.

Abstract

Nowadays, the actual industries require massive cost savings. Thus, it makes sense to improve basic materials. Various properties may be changed to design consumption-friendly materials and to enhance efficiency (e.g. improve heating and abrasive resistance), friction, adhesion and lubrication of materials. Hence, patterning techniques are useful tools to tailor the material properties according to a simple guideline: "*have the right property at the right place*". Numerous techniques are based on surface modifications and involve light sources. Since the achievement of modern laser systems, fast to ultrafast laser are used in labs and industrial groups. They have legion advantages in comparison to embossing techniques such as material patterning without mechanical contact and allow a sub micro-precision. During this thesis, two techniques were used in order to develop and enhance the surface properties of the 100Cr6 steel: the femtosecond laser ablation and laser interference metallurgy.

First, the bearing properties were enhanced by a smart and advanced design of the surface. Secondly, the hydro- and oleophilic properties of irradiated samples were studied and compared to non-irradiated. Finally, a combination of both techniques was performed in order to unite the wetting advantages of both patterning methods.

Various patterns were elaborated in order to determine an optimal structure design and the chemical and topographical properties were consistently evaluated and compared.

Zusammenfassung

Heutzutage müssen sowohl Forschung als auch moderne Industrie so kostengünstig wie möglich arbeiten. Deshalb ist es sinnvoll, Standard-Materialien bzw. deren Eigenschaften zu verbessern: Dies gelingt durch geringeren Brennstoff-Verbrauch, Erhöhen der Materialeffizienz (z.B. besserer Erwärmungs- und Verschleiß-Widerstand), Reibung und Adhäsion, Schmierung, usw. Texturierungsmethoden sind imstande, die Materialeigenschaften gemäß eines einfachen Prinzips auszubilden: "*die richtigen Eigenschaften an der richtigen Stelle*". Techniken auf Basis von Lichtquellen erlauben solches Design, weshalb kurze und ultra-kurze Laser-Systeme in Entwicklungsabteilungen genutzt werden. Gegenüber Prägungsmethoden ergeben sich zahlreiche Vorteile. Das Verfahren funktioniert ohne mechanischen Kontakt und mit einer submikron-Präzision. Zwei Lasermethoden wurden benutzt, um die 100Cr6 Stahl Eigenschaften zu verbessern: die Femtosekunden Laser Ablation und Laser Interferenz Metallurgie.

Zuerst wurde die Tragfähigkeit durch ein sinnvolles Design verbessert. Danach wurden das hydro- und oleophile Verhalten von texturierten Proben untereinander und mit unstrukturierten Proben verglichen. Abschließend wurden die beiden Laser-Prozesse miteinander kombiniert, um so die Vorteile der jeweiligen Methode zu erhalten.

Mehrere Muster wurden hergestellt, um ein optimiertes Design zu erzeugen. Die chemischen und topographischen Eigenschaften der Strukturen wurden stets charakterisiert und miteinander verglichen.

Symbols and acronyms

Symbols

A_{real}	real area
$A_{apparent}$	apparent area
Ca	capillary number
E_D	net energy
η	dynamic viscosity of the fluid
F	applied force
g	gravity acceleration
γ	surface tension
γ_{SL}	surface tension of the solid-liquid phase
γ_{SV}	surface tension of the solid-vapor phase
γ_{VL}	surface tension of the liquid-vapor phase
h	height
i	refractive index of the ambient atmosphere
I	intensity
k	propagation constant
κ^{-1}	capillary length
L	length
λ	wavelength
λ_{sp}	surface plasmon wavelength
μ	dynamic viscosity
ν_0	initial frequency
ν_1	double frequency
ω	angular frequency the wavelength
P	period
p_0	ambient pressure
p_d	droplet pressure
ϕ	total area of liquid-air interface
ψ	wavefunction
R	radius
Rf	roughness factor
ρ	density
S	spreading parameter
t	time
θ	angle between two incident beams
V	speed
z	coordinate in the propagation direction

Acronyms

AFM	Atom Force Microscopy
AKD	AlkylKetene Dimer
AOM	Acousto-Optico Modulator
APT	Atom Probe Tomography
CL	Correlation Length
cw	Continuous wave
ECAP	Equal Channel Angular Pressing
EDS	Energy Dispersive Spectroscopy
FIB	Focused Ion Beam
FWHM	Full Width at the Half Maximum
fs	femtosecond
IFAM	Institute for Manufacturing Engineering and Applied Materials
LASER	Light Amplification by Stimulated Emission of Radiation
LBO	Lithium Triborate
LEAP	Local-Electrode Atom-Probe
LIBS	Laser-Induced Breakdown Spectroscopy
LIPSS	Laser Induced Periodic Surface Structure
LIL	Laser Interference Lithography
LIMET	Laser Interference Metallurgy
LST	Laser Surface Texturing
NA	Numerical Aperture
Nd:YAG	Neodymium-doped Yttrium Aluminium Garnet
Nd:YLF	Neodymium-doped Lithium Yttrium Fluoride
Nd:YVO4	Neodymium-doped Vanadate
ns	nanosecond
ps	picosecond
RH	Relative Humidity
ROI	Region Of Interest
SAD	Selected Area Diffraction
SEM	Scanning Electron Microscopy
STEM	Scanning Transmission Electron Microscopy
TEM	Transmission Electron Microscopy
WLI	White Light Interferometry
XPS	X-ray Photoelectron Spectroscopy

1 Introduction

1.1 Motivation

In the present economical context, the financial crisis showed that the modern and more specifically the European industry requires a permanent and constant "*forward motion*" characterized by the research of efficiency and reduction of costs. Indeed, the steel suppliers such as Dillinger Hütte GTS© or automotive industries ZF Friedrichshafen© have based their survey and financial health despite the economical crisis on the elaboration of innovative and high-quality products such as the 43,000 tonnes of DI-MC 460 structural steel or the ZF 9-speed automatic transmission, respectively.

Multiple high-quality materials were elaborated by improving their properties. The nature mimicry is an infinite source of inspiration for the improvement of properties such as hardness, torsion resistance, lubrication and wetting. The industries involving tribology knowledges are probably one of the domains employing the highest quantity of systems inspired by nature. Indeed, it is known that wear and friction cost billions of dollars each year due to the degradation of materials and devices and for these reasons the reduction of friction is a major concern in many industry domains. Sharks are probably feared as the most dangerous aquatic predators and if its interesting dental anatomy [1] is still a topic of scientific researches, the study of their skin properties is crucial to explain their high velocity. The design of the shark skin is made of V-scale arrangements which significantly reduce the drag in water [2, 3]. Based on the knowledge of these unique pattern designs, applications were elaborated and are successfully used nowadays in different industrial domains. The manufacturing of body swimsuits inspired by shark skin became famous in 2008 for the Olympics in Beijing when Michael Phelps won his eight Olympic titles by wearing the Speedo Fastskin3©, while their efficiency is nowadays still discussed and no proof was found showing that they increase the velocity [4] as it could be affirmed by the manufacturers. Nevertheless, a consequent drag reduction is still observed in comparison with a flat silicon structure.

The shark skin composition has also successfully inspired researchers of the Fraunhofer Institute for Manufacturing Engineering and Applied Materials Research (IFAM) in Bremen, who developed a paint with an unique structure for airplanes [5]. Based on nature observations, Bechert *et al.* built shark skin replica with different surface patterns and studied the effects of their geometrical dimensions (distance between them, height, two- or three-dimensional structures) on the drag reduction [6]. The so called "riblet-paint" is elabo-

rated with precise geometrical dimensions and trapezoidal-shaped grooves. A reduction of 10 % of the turbulent skin friction is observed in comparison to the flat surfaces in addition to the extremely high environmental conditions related to the aircrafts (- 55 to +70 degrees Celsius) and no weight addition. Finally, IFAM estimates that 4.48 million tons of fuel could be saved if this nature-inspired paint would be applied to every airplane each year. Recently, numerous techniques for the functionalization of material surfaces have been proposed. Some of these methods have been inspired by nature such as gecko or shark skin which are, respectively, known for their adhesion and friction properties. This kind of scientific mimicry has been reported to produce beneficial effects [7]. The tribological behaviour can be improved using techniques based on mechanical (grinding, honing) [8, 9], lithographic [10], coating [11] and also patterning procedures [12, 13]. High-power pulsed laser beams interact with materials and provide a potent new process to modify the surface microstructure, topography and chemistry [14–16]. During the last few years, different patterning methods were developed in order to functionalize materials [17].

1.2 Tasks of this work

This work was originally motivated by the requests of an industrial partner to tailor the oleophilic behaviour of the industrial bearing steel 100Cr6 by means of the femtosecond laser structuration. The main goals were to improve the wettability i.e. to enhance the repartition of the oil on the surface of the material in comparison with a flat surface. The first contact angle measurements confirmed that the roughness is a parameter which drastically influences the wetting behaviour. Thus, the control of the roughness appears as the key to control the oil wettability. Ordered structures were then created using femtosecond laser irradiation and the contact angle measurements confirmed the former assumption. In order to improve this method to control wetting, other patterns were created using femto and nanosecond laser and a combination of both structures.

100Cr6 samples were prepared by metallographic procedure and then they were irradiated using laser ablation and laser interference metallography (LIMET). The LIMET and ablation procedures were performed using a Ti:sapphire femtosecond laser and a Nd:YAG nanosecond laser, respectively. Different structures and patterns were created by changing the geometrical parameters such as period, depth, etc. The pattern design was made in consideration of the technical abilities offered by the femto- and nanosecond laser at the Chair of Functional Materials. Moreover, the design of the structures was elaborated regarding their simplicity, efficiency and potential life duration to be created at the surface of the samples. For these reasons, the laser surface texturing (LST) was permanently related to the topographical studies.

The effects of laser irradiations on the chemical compositions of 100Cr6 were studied using Raman and X-ray photoelectron spectroscopy (XPS) and atom probe tomography (APT). Scanning transmission electron microscopy (STEM) and transmission electron microscopy (TEM) were also performed in order to study the impact of the laser irradiation on the microstructures. The topographies of the samples were analyzed using white light interferometer (WLI) and scanning electron microscopy (SEM). Their bearing properties and the homogeneity of the structures were then compared. These studies of the laser irradiations and especially in the case of the femtosecond laser offers a complete and multi-scalar cartography of the irradiated zones, which is the novelty and main point of interest of the present thesis.

Dynamic contact angle measurements were performed at the surface of laser structured samples using distilled water and an industrial oil under room conditions. The effects of the geometrical parameters of the patterns such as periodicity, depth, homogeneity, were studied and compared. These analyses allowed to determine the main parameters involved in the wetting with regards to the previous established models. This study brings forward important and decisive arguments crucial for the engineers and scientists for example in the lubrication community. In particular, this part of the thesis reports evidences and explanations on the choice of the design for the control of the lubrication regime i.e. the fluid film thickness for example. The limits of the different patterns have been reported and finally a combination of femto- and nanosecond laser structures was produced in order to create an "optimized pattern". The aim of this combination was to design a structure which allowed a fast and oriented wetting, fulling cavities which can act as lubricant *reservoir*.

2 State of the art and theoretical considerations: Laser and Wetting

2.1 Laser patterning: laser systems, modes, effects and applications

In the last decades, numerous techniques for the treatment of material surface have been proposed and multiple were inspired by nature observations. It has been reported that this kind of scientific mimicry has beneficial effects [7]. Laser texturing is a typical successful example of this mimicry and results in different applications depending on the system to be optimized. In the present chapter, different kinds of laser texturing will be presented taking into account the laser mode (ablation continuous wave and interference), their effects on the materials (chemical and/or topographical) and their potential applications. The attention of this chapter will be focused on the laser-matter interactions of femtosecond and nanosecond laser systems in order to help the readers of this thesis to understand the motivation and goals of this work.

2.1.1 Laser systems: femtosecond versus nanosecond laser

The term "laser" is nowadays a common acronym for Light Amplification by Stimulated Emission of Radiation which found its origin with the study of the stimulated emission of radiation by Albert Einstein in 1917. The stimulated emission can be shortly defined when an inversion of population of electrons occurs. An incident photon induces the jump of electrons in an excited state to lower energetic levels. In order to place the electrons in these higher energetic levels, a prior energetic source is used to pump i.e. to excite the atoms. This energetic source can be lamps or another laser as it will be described further. The state of the atoms matter defines the type of laser such as a gas (CO_2) or a solid (Nd:YAG). The laser can be defined as a high-intensity beam characterized by a highly-directional and a single frequency i.e. a wavelength. The laser is also characterized by spatial and temporal coherences. The spatial coherence is a property related to the propagation of parallel waves in one single direction. The spatial coherence is a typical laser property in opposition to common light sources such as filament lamps. The temporal coherence of the laser is related to its monochromaticity. Indeed, since the laser wave is perfectly monochromatic, it is correlated at any time.

Since in this thesis, the two laser systems used for laser irradiation are a

nanosecond Nd:YAG and a femtosecond Ti:sapphire laser, they are yet basically described and compared. The Nd:YAG laser or so-called solid state laser

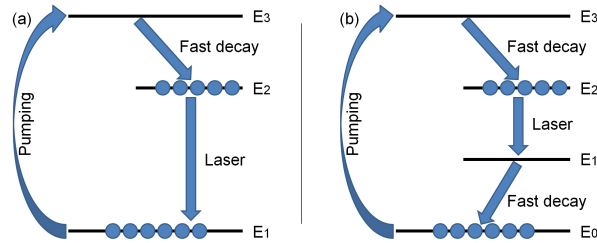


Figure 1: Schematic representations of the (a) three-level and (b) four-level transitions.

is made of three main components which are an active medium, a pumping source and an optical resonator. YAG referred to Yttrium Aluminum Garnet and is doped with Neodymium. In the present case, the pumping is made by flash lamps which induce the stimulated emission described above. The laser pumping results in populating higher energy levels by the emission of photons. Thus, the stimulated emission is maintained and amplified in the optical resonator usually made of one totally-reflecting mirror and a semi-reflecting mirror (output). The flash lamps and the resonator can have different geometries. It has to be noticed that the inversion of population required for the laser emission occurs at three or four-level transitions as it is schematically represented in the figure 1. In the present case of Nd:YAG laser, the laser transition occurs at $1.06 \mu\text{m}$.

The requirements for the emission of Ti:sapphire femtosecond laser pulses are more complex and the set-up implies different laser as it is yet presented. First of all, a so called *Empower* laser head contains a laser pump chamber, a lithium triborate (LBO) crystal and acousto-optico modulator (AOM also called Q-switch). The laser pump chamber is an array of diode laser plus Nd:YLF rod which means neodymium-doped lithium yttrium fluoride also called "yilf". The diode laser excites the electrons of the neodymium atoms in the YLF crystal, as described above and emits at the 1053 nm wavelength. This infrared laser light is "frequency-doubled" to 527 nm and energetic Q-switched pulses are emitted, which are ideal to pump the Ti:sapphire ultrafast amplifiers. The frequency-doubling is commonly used for generating laser lights with shorter wavelengths and can be defined as the phenomenon which transforms an incident wave with an initial frequency ν_0 into a wave with a double frequency ν_1 with $\nu_1 = 2\nu_0$. This transformation from fundamental infrared to harmonic green light is realized by passing through a nonlinear crystal, which is in the present case a LBO crystal. The AOM is used to

amplify the high energetic gain from the Nd:YLF and to deliver a powerful laser pulse. Basically, the role of the *Empower* is to energize the amplifier. A CW diode-pumped laser (Nd:YVO₄ neodymium-doped vanadate crystal) and a Ti:sapphire pulsed laser are combined in the *Mai Tai* laser system. Since the Ti:sapphire absorption range is in the blue and green domain, the output of the diode laser allows the stimulated emission of the crystal, which is a monocrystal of alumina doped with titanium ions (Ti³⁺). The crystal delivers wavelengths near the infrared domain from 750 to 850 nm and the maximum laser efficiency is generally obtained for 800 nm for pulses lower than 100 fs. The CW pump chamber provides green (532 nm) laser light with intensities higher than 5 W. The pulsed output chamber regroups the Ti:sapphire cavity i.e. Ti:sapphire rod, focusing mirrors, control elements and timing element.

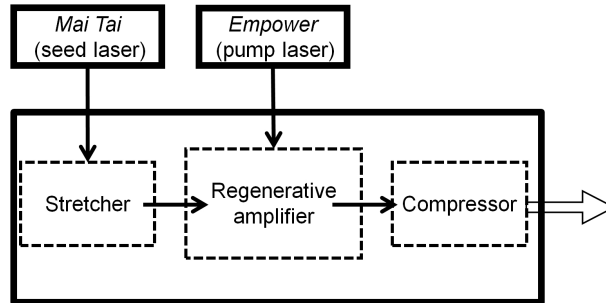


Figure 2: Schematic representation of the femtosecond laser system showing the *Empower* pump laser, *Mai Tai* seed laser and the *Spitfire Pro* system.

Finally, the *Spitfire Pro* system also described as "Ti:sapphire regenerative amplifier systems" amplifies the femtosecond pulses emitted by the *Mai Tai*. The typical output wavelength emitted by the *Spitfire Pro* is in the range from 750 to 840 nm. The amplifier can provide amplified pulses from 2 ps to less than 35 fs. The mode used during this thesis was preset by the manufacturer to deliver 1 kHz pulse repetition rate. The amplifier system contains an optical pulse stretcher and an optical compressor and a regenerative amplifier. According to the schematic representation (figure 2) based on the user's manuals delivered with the femtosecond laser, the *Mai Tai* delivers the input sub 100 fs pulses, which are stretched in duration using a combination of mirrors, then energetically amplified in the regenerative amplifier (titanium sapphire crystal). The *Empower* provides the energy to pump the amplifier.

The temperatures of both former systems are permanently controlled and maintained constant in order to provide optimum performances of the entire

laser system.

2.1.2 Laser ablation mode

The laser ablation process is a common topic in the field of laser surface engineering. In opposition to other methods - which will be presented later - the laser ablation procedure can be easily operated and requires less optical elements. The laser ablation can be applied to different types of materials and using different laser types. In the present thesis, most of the ablation studies which will be presented were performed using short or ultra short laser as it is related to the present PhD. Detailed examples of this procedure will be given at the end of this section.

De Lucia *et al.* studied the effects of femtosecond laser pulses in laser-induced breakdown spectroscopy (LIBS) on aluminium foils in comparison with nanosecond pulses, which are usually used for this technique [18]. They studied the differences in the plasma emission for the two former laser configurations and observed first that femtosecond pulses allow the plasma generation at lower laser fluences (nano: $30 \text{ J}\cdot\text{cm}^{-2}$ and femto: $10 \text{ mJ}\cdot\text{cm}^{-2}$). Here, this low fluence application offers advantages in comparison to conventional nanosecond laser systems: the energetic costs are reduced, the low energetic use allows to study non-stable materials such as explosives and less damage of the sample is induced.

The work of Stuart *et al.* focuses onto the ablation of multilayer dielectrics and gold-coated optics by using high-power short-pulse laser [19]. It compares the morphology of damages induced by laser pulse duration from 140 fs to 1 ns. The maximum value of the damage threshold measured onto the surface of gold films is found to increase from 0.5 to $1.5 \text{ J}\cdot\text{cm}^{-2}$, as the pulse duration varies from 600 fs to 800 ps as shown in figure 3.

Preuss *et al.* report the effects of laser ablation on different materials such as Nickel, Copper, Gold etc. by short laser pulses (0.5 ps) under different atmospheres (air and vacuum) [20]. As described previously, the femtosecond ablation of Indium leads to the creation of well-defined hole in comparison with nanosecond laser ablation, which induces rough and irregular spots. As shown in figure 4, the atmosphere used for the laser ablation is a real strong aspect onto the aspect of the irradiated zone. Under ambient conditions, the limits of the spots appear strongly irregular while under vacuum atmosphere, the border of the craters are well-defined.

Momma *et al.* performed laser ablation on metallic materials (copper and steel foils) using a commercial Ti:sapphire laser system at 780 nm wavelength

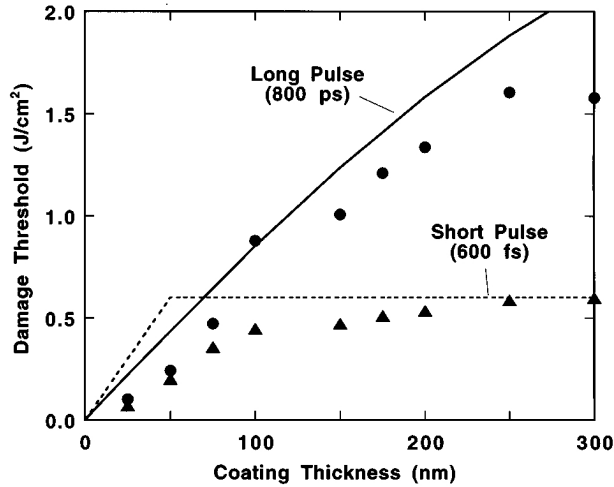


Figure 3: Predicted and measured damage thresholds for gold films [19]. By long laser pulse durations, the damage threshold significantly increases.

with a broad range of potential pulse duration (0.15 to 5000 ps) [21]. The ablation process performed using short laser pulses allows a precise control of the ablated geometry on the material in comparison with long laser pulses. Using a laser system with a 3.3 ns pulse duration, Momma *et al.* obtained chaotic and rough dot structures onto the surface of steel foils, while the crater appears regular with very precise boundaries when using a 200 fs laser pulse. Chichkov *et al.* studied and observed similar effects of irradiation using femto-, pico- and nanosecond laser on various metals and solids [22]. In addition to the elaboration of holes with precise borders, they showed that the pulse number has a strong influence onto the morphology of the crater at the surface of copper and steel samples.

The femtosecond laser ablation process is based on the unique interaction of short pulse laser radiation with metallic materials. Based on the works of Hirayama *et al.* [23] and Brorson *et al.* [24], the electron-lattice relaxation time of metallic materials varies from 1 to 10 ps. Then, if the pulse duration of the laser is shorter than the previous-mentioned electron-lattice relaxation time, no thermal ablation of the metal and no melted material will appear.

As the atmosphere influences the irradiation by femtosecond laser, the ablation mostly varies with the type of materials and can induce a topographical and/or a chemical modification of the material.

The possibilities offered by femtosecond laser systems are not limited to metallic materials. As Delobelle *et al.* show in their study, the laser ablation was successfully applied to borosilicate glass in order to create nano-craters

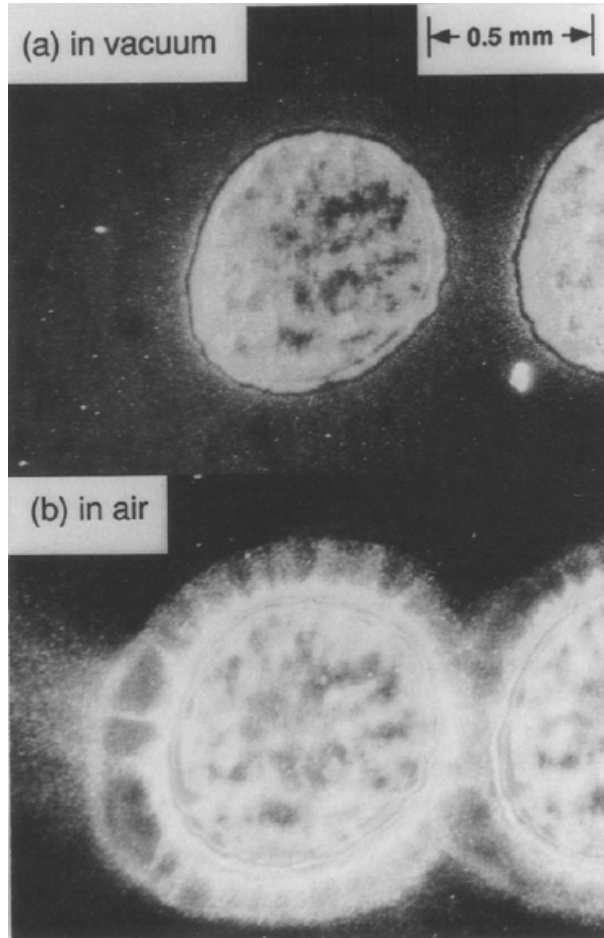


Figure 4: Optical micrographs of ablation sites on Ni in vacuum(a) and in air (b) after 50 ablation pulses [20].

[25]. The femtosecond laser irradiation induced patterns with single or double drilled craters depending on the set-up parameters chosen such as the polarization, the fluence and the numerical aperture (NA). The linearly- or circularly-polarization strongly affects the morphology of the craters as it is showed in the SEM micrographs in figure 6.

The effects of polarization are studied in the case of a single-shot ablation. The linear-polarized configuration leads to anisotropic patterns at the surface of the glass, while the circular-polarized configuration induces symmetrical nano-holes as shown in the figure 6. Nielsen and Balling study the effects of the s- and p-polarized ultrashort laser and observe that the polarized orientation has an influence onto the final hole shape [26]. Indeed, assuming that no multiple reflection process occurs and for certain threshold fluence

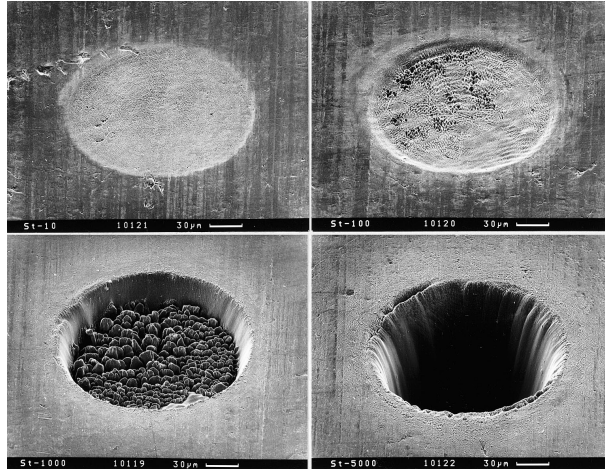


Figure 5: Femtosecond patterns onto steel surface with different pulse numbers: (a) 10, (b) 100, (c) 1000 and (d) 5000 [22].

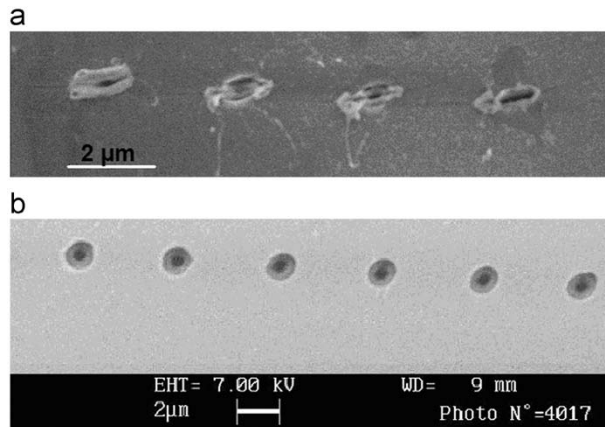


Figure 6: SEM views of nanocraters drilled by (a) linearly polarized femtosecond pulses. The anisotropy of the crater is directed along the polarization direction. (b) Circularly polarized pulses. These two pictures have been obtained with the same fluence [25].

conditions (i.e. adapted to the material), the p-polarization allows a more homogeneous ablation of the material, while under s-polarized irradiation no ablation is possible at the external boundaries of the craters.

Ihle *et al.* studied the effects of nanosecond and femtosecond excimer-laser on oxide ceramics (Al_2O_3 , MgO and ZrO_2) [27]. Two different behaviours were observed depending on the pulse-duration of the laser: the nanosecond laser shows a behaviour including plasma heating and inducing

thermal ablation while the femtosecond irradiation does not cause thermal ablation. Using nanosecond laser, residual heated zones occur around the irradiated zones, while with femtosecond, no thermally affected surrounding zone is observed and the structuring can be achieved with a micrometer resolution.

Kononenko *et al.* performed ablation tests on ceramics (Al_2O_3 , AlN, SiC and Si_3N_4) and on metals (steel and aluminum) under different controlled atmospheres (vacuum, air and argon) using nanosecond and picosecond laser [28]. They demonstrate that the ambient atmosphere has a significant role regarding the efficiency of the ablation process. Indeed, the ablation rate which was defined as "a ratio of a sample thickness to a number of laser pulses which was necessary to apply to produce a through hole" was found to be maximum under vacuum. Nevertheless, this behaviour appeared to be dependent on the fluence regime. For aluminum sample, the ablation rate was found to be significantly higher at low energy density regimes, while at high fluence regimes, the ablation ratio gradients have lower values.

The ripples are periodical structures arising from the femtosecond laser irradiation. Ripples are also described as laser induced periodic surface structures (LIPSS). LIPSS directly result from the femtosecond laser irradiation but are not related to the strictly defined ablation phenomenon. The different phenomena occurring during femtosecond laser irradiation will be explained later. The morphology of the ripples is a common research topic for the laser community since the achievement of the femtosecond laser systems. Their sizes and periods depend on the laser wavelength, the angle of incidence and the surface Plasmon. Huang *et al.* study the origin of these near-subwavelength structures onto the surface of dielectrics, semiconductors and metals and finally state that the surface-Plasmon-laser is the main process leading to their formation [29]. Multiple parameters have an influence on the period of ripples and is generally defined by the laser community as close or smaller than the laser wavelength. Hou *et al.* explore the elaboration of long-periodic and short-periodic ripples (with 530-600 nm and 260-300 nm periods, respectively) on stainless steel samples using femtosecond laser [31]. They observe that the pulse number and fluence have a strong influence on the aspect and period of the ripples as shown in the graph 8. These curves obtained by Hou *et al.* confirm first that the morphology of the ripples is controlled by a combination of set-up parameters.

In the study of Chakravarty *et al.*, the authors affirm that, depending on the experimental parameters, the period of the nano-ripples formed us-

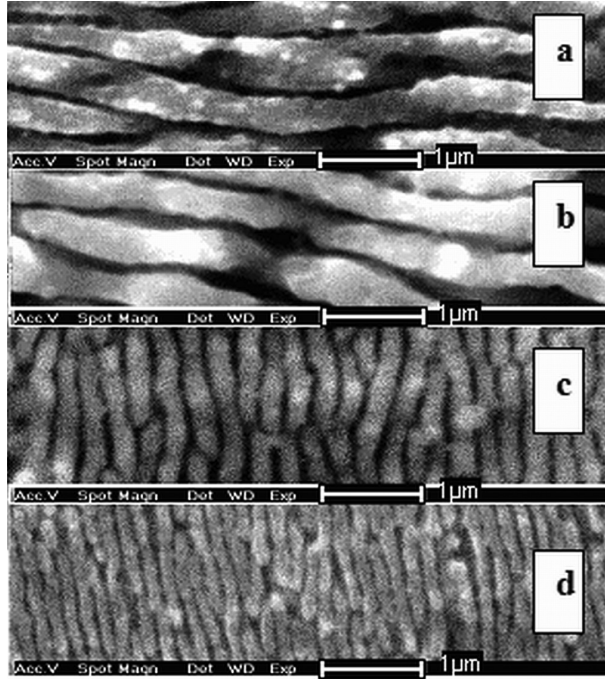


Figure 7: Nano-ripple formation using 800 nm pulses in narrow band gap semiconductors: (a) GaAs and (b) InP; and in wide bandgap semiconductors: (c) GaN and (d) SiC. The length of the horizontal bar is 1 μm in (a), (b), (c) and d) [30].

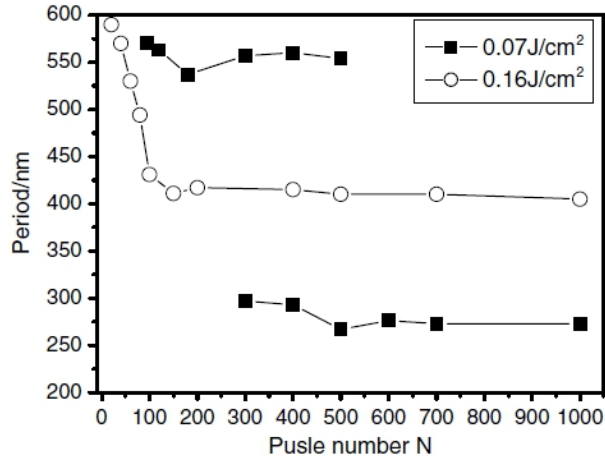


Figure 8: Dependence of ripple period on the pulse number N [31].

ing a Ti-sapphire laser (45 fs pulse duration, 800 nm wavelength) varies in the range: $\lambda/9 - \lambda$, where λ is the wavelength of the incident laser beam

[30]. Their experiments were performed onto the surface of semiconductors and authors attribute the formation of nano-ripples "*considering the transient metallic nature of the semiconductor surface on irradiation with intense femtosecond pulses*" and the surface plasmon which interferes with the incident laser light. The surface plasmon is defined by Jiri Homola [32] and based on the work of Wood [33] and Fano [34] as "*narrow dark bands in the spectrum of the diffracted light [...] referred as anomalies [...] associated with the excitation of electromagnetic waves on the surface of the diffraction grating*".

In the *Handbook of Surface Plasmon Resonance*, edited by Schasfoort and Tudos, Kooymani gives the definition of surface plasmon as "*propagating electron density waves occurring at the interface between metal and dielectric*" [35].

As the surface plasmon interacts with "*the incident laser light with the rough target surface*" [30], free electrons become excited by the multiphoton ionization of the laser irradiation and as the irradiation begins, the roughness is enhanced. When the surface properties are changed, it leads to a "*more efficient excitation of surface plasmon*". In consequence, the molten material is ordered according to "*the shape of a grating*" related to the incident beam and surface plasmon. Finally, during the cooling of the material (at the end of the laser pulse), nano-ripples are formed. Based on this explanation, Huang *et al.* [29], Han *et al.* [36] and Chakravarty *et al.* [30] proposed a formulation to calculate the period of the laser ripples (p) depending on the incident wavelength of the laser beam (λ), the surface plasmon wavelength (λ_{sp}), the refractive index of the ambient atmosphere (i) and the incident angle (θ).

$$p = \frac{\lambda}{\frac{\lambda}{\lambda_{sp}} \pm i \sin \theta} \quad (1)$$

Equation 1 clearly shows that the period of the ripples is influenced by the laser set-up (depending on the incident angle and laser wavelength), the atmosphere and finally the material properties (surface plasmon wavelength). However, the authors express special reasons resulting in the non-formation of ripples. The main reason is the value of the fluence chosen for the irradiation. Indeed, at low fluence, the surface of the material could not be molten or the laser energy could not activate the surface plasmon and then no ripple is formed.

Researches were also performed in order to determine the origin of the ripples-orientation. According to the literature, their orientation is perpendicular to the laser polarization and this is clearly observed by Huang *et al.* [29] and Her *et al.* [37]. While the use of circular-polarized laser should prevent

a preferential orientation for the formation of the structures, as Tran *et al.* expected and experimented it [38]. The light is defined as an electromagnetic wave meaning made of electric and magnetic waves. This electric wave (E) is decomposed according to the Maxwell's theory as:

$$E = E_0 e^{-i(kz - \omega t)} \quad (2)$$

with z as the coordinate in the propagation direction, t the time, ω is the angular frequency and λ the wavelength. k ($k = 2\pi/\lambda$) is defined as the propagation constant [39]. The polarization of the laser - which can be linear, circular or elliptical - corresponds to the oscillation of the electric field defined previously in equation 2 in a certain plane. The plane of incidence contains the incident beam and is perpendicular to the material surface. The different natures of the polarization are defined as long as the linear polarization is in a single plane, the circular polarization as the electric field regularly rotates along the direction of propagation. Finally, the elliptical polarization rotates with an elliptical shape along the propagation axis as E rotates with a constant angular velocity and also its absolute value of the field vector [40]. The circular polarization is a "derived configuration" of the elliptical polarization, as the value of the field vector is constant. The linear polarization can be differently described as E is perpendicular to the plane of incidence and is then defined s-polarized (s for *senkrecht* in German language). The p-polarized configuration corresponds to the presence of E in the incident plane (p for *parallel*) [40].

As most of the commercial laser systems are linear polarized [40], the attention is now focused onto s- and p-linear polarized laser. The formation of LIPSS is then dependent on the polarization as the electric field orientation varies and then influences the laser-matter interactions [40]. J. Reif affirmed that the laser polarization has a "*dominant influence*" onto the "*ripples formation*" but the "*effect is by far not yet understood*" [41]. The orientation of ripples is, typically, perpendicular to the electric field i.e. to the laser polarization as it has been reported in multiple studies [29, 31, 41–44] and as it is shown in figure 9. Hou *et al.* clearly demonstrate that the ripples orientation is orthogonal to the electric field vector represented in the left corner [31]. Moreover, Reif observes that change of the polarization orientation was not affected by the crystalline structure of the material [41].

The LIPSS topography was studied by atomic force microscopy (AFM) and SEM by different research groups [45, 46]. As the period of ripples varies, the height is also affected by certain laser parameters such as the fluence and polarization. Tan and Venkatakrisnan show in their study that the laser pulse energy applied onto the surface of crystalline silicon and varying from 70 to 100 nJ has a significant influence onto the depth of ripples [45]. Indeed,

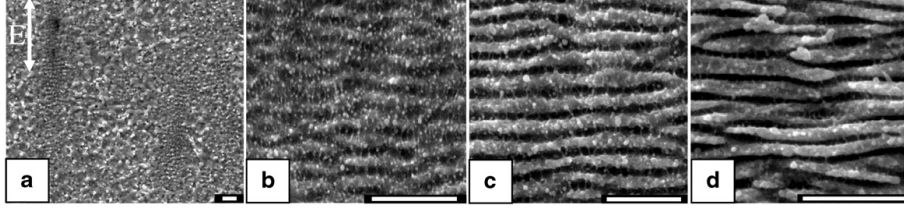


Figure 9: SEM images of the surface patterns by the laser irradiation at fluences of (a)–(d) $0.16 \text{ J}\cdot\text{cm}^{-2}$ and (e)–(h) $0.07 \text{ J}\cdot\text{cm}^{-2}$. The irradiation pulse numbers are (a) 10, (b) 50, (c) 100, (d) 500, respectively. E direction shows the laser polarization, and the scale bar is $2 \mu\text{m}$ [31].

the depth increases non-linearly with the fluence, from 42 to almost 95 nm depth, for 70 and 100 nJ, respectively (figure 10). Moreover, authors found that the type of polarization (linear or circular) and its orientation (s or p) influence the morphology of ripples as shown in the table 1. The depth was found to vary significantly as the laser was p- or s-polarized leading to an increase of 40 % of the depth.

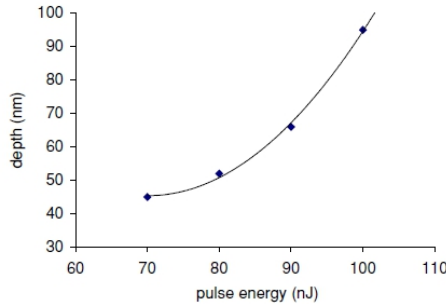


Figure 10: Ripple depth versus pulse energy (s-polarization) [45].

Laser polarization	Ripples depth [nm]
linear p-	101
linear s-	145
circular	122

Table 1: Depth calculated from cross-section profile of ripples formed by laser beam of 100 nJ pulse energy [45].

Momma and Chichkov *et al.* schematically detailed the long and ultra short laser mechanisms involved into the nano- and femtosecond laser irradiation of

solids [21, 22, 47]. As the ablation with femtosecond laser implies pulse duration shorter than the electron-lattice relaxation time, they consider a "*direct solid-vapor (or solid-plasma) transition*" without melting of the metallic target. It induces the formation of "*vapor and plasma phases*" and the thermal conduction can be neglected. On the opposite, in the case of long pulses (nanosecond pulses) the metal is heated and molten. In the literature, the plasma is defined as: "*a wide variety of macroscopically neutral substances containing many interacting free electrons and ionized atoms or molecules, which exhibit collective behavior due to the long-range coulomb forces*" by J.A. Bittencourt in his book *Fundamentals of Plasma Physics* [48]. A more simple definition of plasma is given by U. Schumacher, as "*an ionised gas, consisting of free electrons and atoms or molecules [...] characterized by its collective behaviour*" [49]. A plasma occurs when a material is heated and atoms or molecules become sufficient thermal kinetic energy "*to overcome the binding potential energy*". The plasma is often defined in the literature as the fourth state of the matter, besides solid, liquid and gas. Bonse *et al.*

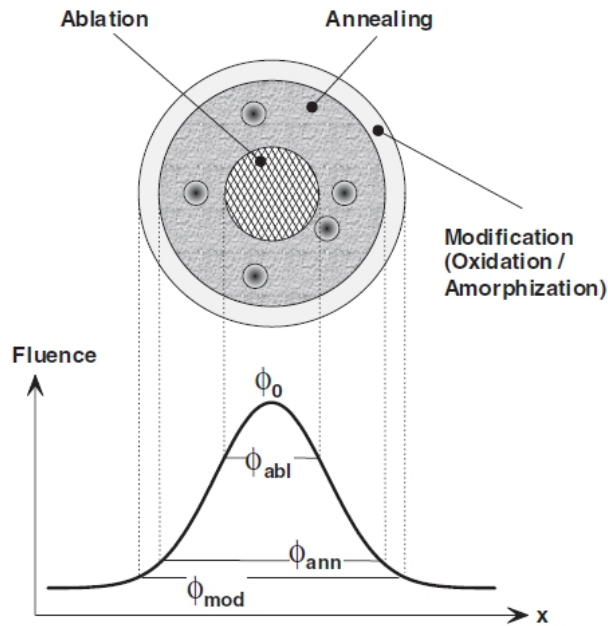


Figure 11: Physical processes during the modification of silicon with femtosecond laser pulses and their threshold fluences [50].

published the "cartography" schematically presented in figure 11 [50]. The previously mentioned ablation and ripples occur in the ablation and annealing regions. Then, a third zone appears at the border of the irradiated zone i.e. at the extreme limit of the laser intensity distribution. In this region, the

morphology of the sample is not significantly affected but processes resulting from oxidation and amorphization occur. Finally, Bonse *et al.* propose a schematic representation (figure 12) summarizing the morphological and microstructural influences of the increasing pulse number and laser fluence on the silicon surfaces [50]. Indeed, it shows that the presence of ripples and spikes (cones) only occurs at high pulse number and high fluence (above the ablation threshold), respectively. Tran *et al.* published a similar schematic

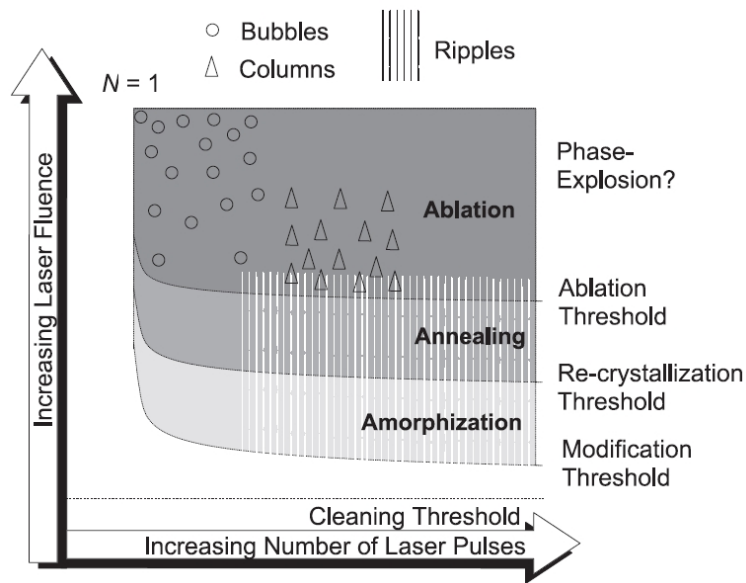


Figure 12: Scheme of the different morphological phenomena after irradiation of the silicon surface with linearly polarized femtosecond laser pulses of typically 100 fs duration [50].

illustration (figure 13) to the Bonse's scheme (figure 11) with additional zones influenced by the laser irradiation [38, 51]. As shown in figure 13, the first zone at the border with the non-irradiated region results from the diffraction of the beam and is described as "*outer modification*" region with possible phase transformations. The presence of diffraction has to be carefully considered as it is strongly dependent on the homogeneity of the beam. Thus, an area (corresponding to the lowest laser intensity region) with "*no phase change*" surrounds the area hit by the maximal laser intensity. This area is then divided into three different zones: in the middle the ablation zone, where authors noticed the presence of linear ripples and no columnar structure or spike. Surrounding it, there is the modification region resulting from the resolidification of materials (melting) leading to amorphous and polycrystalline silicon. Inside this zone, authors report the presence of a circular zone

made of re-deposited materials, which results from the pure ablation process. Authors assumed that the presence of columnar patterns is controlled by the number of pulses used for the patterning. The previous section shows the

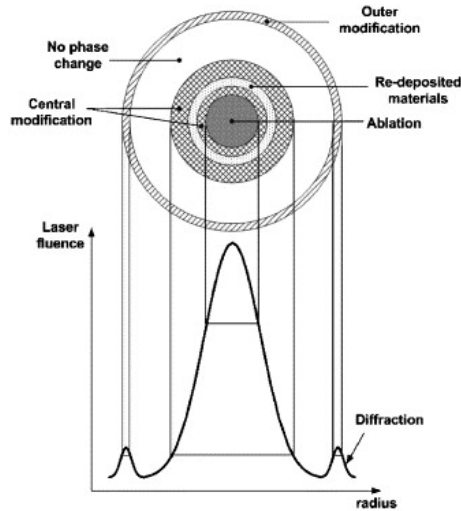


Figure 13: Schematic illustration of different annulus regions of surface damage morphologies and ablation observed on silicon by multiple sub-threshold ultrashort laser pulses [38, 51].

multiple physical effects and phenomena related to the laser ablation and involved in the surface texturing by means of femtosecond laser irradiation. This former state-of-art demonstrated that all these parameters have to be carefully considered regarding their complex and interconnected effects.

2.1.3 Continuous wave laser

Laser in the continuous-wave (cw) mode are used worldwide for the treatment of materials but are employed in different ways. Cw-mode implies that the operating laser is continuously pumped and the laser beam is continuously emitted. Laser assisted machining (LAM) is an extension of the plasma assisted machining, this method is used for the cutting of materials, which can be ceramics, hard steels and alloys [52]. The continuous laser is used as a heat source. By heating the material with the laser, the strength of the material is reduced and the workpiece can be easily cut using a traditional cutting tool, as it can be seen on the figure 14.

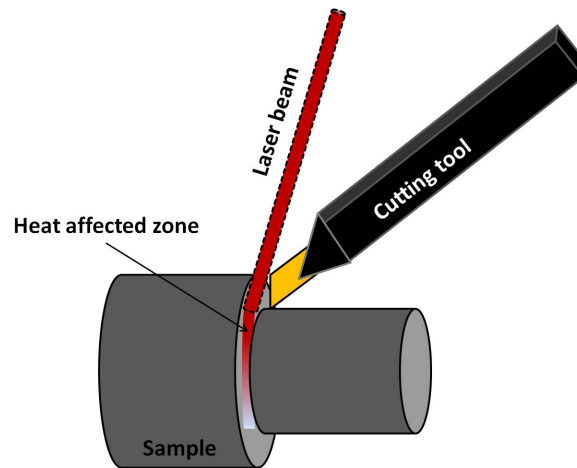


Figure 14: Schematic representation of a LAM procedure during the cutting operation.

Different types of laser can be used for this method: the CO₂-, diode- and Nd-YAG- (neodymium yttrium-aluminium-garnet) laser. CO₂-laser (carbon dioxide) are gas laser and have been the first type of laser used for the LAM process due to their high energy range. The average power varies between few watts to many kilowatts. CO₂-laser operate at a wavelength of 10.6 μm and are commonly used in industry because of their low operating costs and reliability. Taking into account these advantages, the CO₂-laser is widely used for cutting materials such as plastic, metallic and organic materials (e.g. wood) , welding and laser writing [53].

In comparison with CO₂-laser, the diode laser, with a wavelength between 800 nm and 920 nm , have a better absorption for metallic samples. They have been developed in the eighties and were only able to deliver low laser power. In the last few years, they have been improved and can reach power

of about 4 kW in the continuous mode. Diode laser have several application domains as developed in the Fraunhofer IWS Dresden, where diode laser in cw-mode are used for hardening and welding of metallic samples [54]. Diode laser can also be used as pumping laser for solid-state laser such as Nd:YAG-laser.

Nd:YAG-laser is actually the most common solid-state laser in industry used in cw-mode. Nd:YAG laser is a solid-state laser using neodymium-doped YAG for Nd^{3+} :YAG. This type of crystal is favorable for high-power laser and pulsed laser emitting at 1064 nm. In the beginning of the 21st century, Nd:YAG laser could deliver power of 5 kW and now they can reach values of 10 kW [55]. They have an important role in many industries for different applications such as welding, heating, cutting etc. This common presence in the industrial field is obviously related to the qualities of the laser such as the precision of the laser beam and the intensity that it can deliver and which can be adapted depending onto the nature of the materials involved. Laser in cw-mode are also used for the surface tailoring of materials. Zum Gahr and Schreck used a Nd:YAG laser in the cw-mode in order to structure their 100Cr6 samples because they observed that the pulsed mode induced ragged topographies in comparison to regular structures induced by the cw-mode (figure 15) [56].

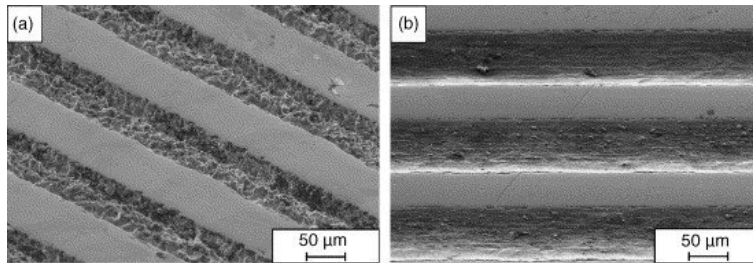


Figure 15: SEM micrograph of a laser structured 100Cr6 sample performed using the (a) Q-switch mode and (b) cw-mode by Schreck and Zum Gahr [56]. These two modes clearly create structures with different aspect.

They produced different cross and line structures in order to study the effect of laser pattern and structure density. It has been shown that increasing the structure fraction led to a decrease of the friction coefficient. Authors demonstrated that for two different configurations (pairing 100Cr6/100Cr6 and 100Cr6/ Al_2O_3), the lowest coefficient of friction was obtained for cross patterns.

2.1.4 Laser interference

As written in the PhD thesis of Andres Lasagni, optical patterning processes are one of the major procedures for the texturing of materials [57]. These techniques differ from their respective energy sources, which can be light, electrons or ions and are generally described as lithography. Lasagni reported the four “indispensable steps” for the lithographic technique: a “*pre-designed set of pattern, a mean to transfer the pattern (e.g. laser light), a responsive medium and tools which ensured appropriated metrology*” and finally the application itself. In the following chapter, different procedures based on the laser interference principle are described considering the final application and their ability to be produced for industrial goals.

The demonstration of the interference of light was first made by Thomas Young (1773-1829), physicist, Egyptologist and doctor [58]. He started his studies on this topic around the begin of the ninetieth century. He reported his experiments in year 1800 in *Experiments on Sound and Light*, in *On the Theory of Light and Colors* (1801) and in *Experiments and Calculations Relative to Physical Optics* (1803). By “making experiments on the fringes of colors accompanying shadows”, Young “found a simple and demonstrative proof” of the interference of light. His experiments resulted in the creation of interference fringes when two portions of light interfere.

Fayou Yu considered in his PhD thesis two laser sources: monochromatic and linearly polarised plane waves with the following wavefunctions [59]:

$$\psi_1 = \sqrt{I_1}e^{i(kr_1+\phi_1)} \quad (3)$$

$$\psi_2 = \sqrt{I_2}e^{i(kr_1+\phi_2)} \quad (4)$$

Assuming that the two beams interfere coherently, the sum of these functions are:

$$\psi = \psi_1 + \psi_2 = \sqrt{I_1}e^{i(kr_1+\phi_1)} + \sqrt{I_2}e^{i(kr_1+\phi_2)} \quad (5)$$

$$\bar{\psi} = \sqrt{I_1}e^{-i(kr_1+\phi_1)} + \sqrt{I_2}e^{-i(kr_1+\phi_2)} \quad (6)$$

Where $\bar{\psi}$ is the complex conjugate of the sum of the wavefunctions and the intensity I can be written as:

$$I = |\psi|^2 = \psi\bar{\psi} \quad (7)$$

$$I = I_1 + I_2 + \sqrt{I_1 I_2} e^{i(k(r_1 - r_2) + \phi_1 - \phi_2)} + \sqrt{I_1 I_2} e^{-i(k(r_1 - r_2) + \phi_1 - \phi_2)} \quad (8)$$

$$I = I_1 + I_2 + 2\sqrt{I_1 I_2} \cos \delta \quad (9)$$

With δ :

$$\delta = k(r_1 - r_2) + \phi_2 - \phi_1 \quad (10)$$

Considering two similar laser sources, their intensities I_1 and I_2 are equal to the intensity amplitude of the partial beams and the equation 9 becomes:

$$I = 2I_0(1 + \cos \delta) = 4I_0 \cos^2 \delta/2 \quad (11)$$

Then the maximum and minimum intensities are: $I_{max} = 4I_0$ and $I_{min} = 0$.

The periodicity of the pattern in the two beam configuration is given by the equation 12 depending on the wavelength of the laser λ and the angle between the two incident beams θ :

$$P = \lambda/2 \sin \theta \quad (12)$$

and the intensity distribution for the two laser beam configuration is then given by:

$$I(x) = 2I_0(1 + \cos(2\pi x/P)) \quad (13)$$

A schematic representation of the intensity distribution in an ideal case is represented in the figure 16

The maximum of intensity corresponds to a minimum of laser structure profile due to the melting and ablation phenomena. As reported by Gachot *et al.* for metallic samples, this intensity distribution leads to a temperature difference varying from 1800 K to 3000 K between the minima and maxima intensity positions [16]. Quenching rates during laser treatment can reach

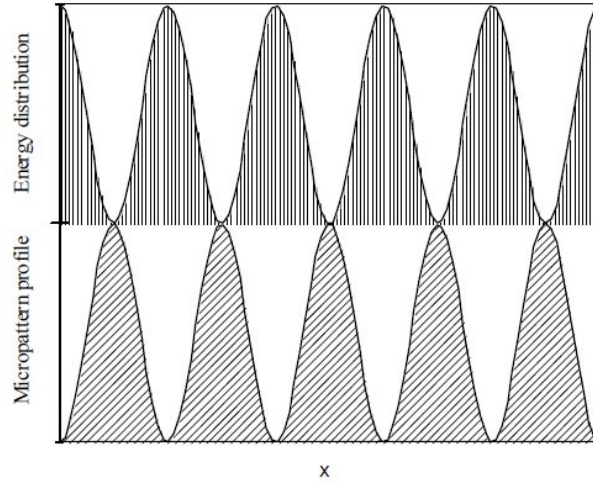


Figure 16: Schematic representation of the energy distribution on the interference pattern and the induced microstructure [59]. Depending on the nature of the material (polymer, bulk metal, thin film), the pattern distribution can be different.

values up to $10^{10} \text{ K}\cdot\text{s}^{-1}$. In the case of metallic samples, these high temperature gradients induce the formation of periodical structures according to the Marangoni convection.

The Marangoni convection is a thermo-capillary flow which is induced by surface tension gradients. These gradients can be induced by irregular temperature distribution or compositions of the system. Marangoni (1840-1925) was an Italian scientist, who studied the wetting of one liquid on another. Considering two liquids A and B composing a certain system, with the surface tensions γ_A and γ_B (with $\gamma_A > \gamma_B$), the surface tension gradient induces a flow at the contact surface. The convection is directed from regions with lower surface tension (γ_B) towards areas with higher surface tension (γ_A) as described by the schematic representation figure 17.

Depending on the sign of the surface tension gradient ($d\gamma_{LV}/dT$), the welding pool can have two different forms (figure 18). When the surface tension decreases, with an increasing temperature $d\gamma_{LV}/dT < 0$, the welding pool is broad and shallow.

On the contrary ($d\gamma_{LV}/dT > 0$), when the surface tension increases along with the temperature, the welding pool is deep and narrow. The presence of certain elements (for example oxygen and sulphur) can drastically change the convection mode. When the concentration of these surface active elements overpasses a certain threshold, the surface tension gradient sign is changed

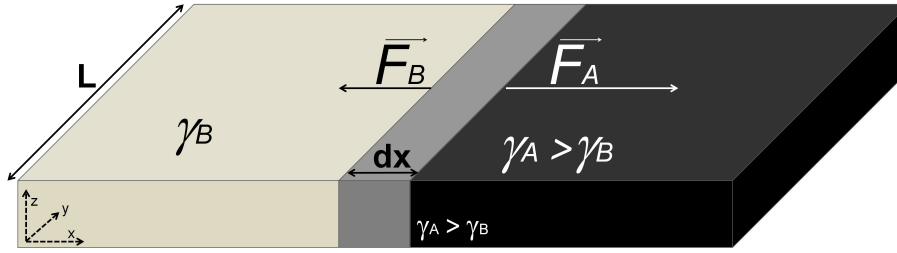


Figure 17: Schematic illustration of the forces acting when two fluids with different surface tensions are brought into contact. A convection is generated (on the surface $S = Ldx$) by this difference from regions with lower surface tension (γ_B) towards areas with higher surface tension (γ_A).

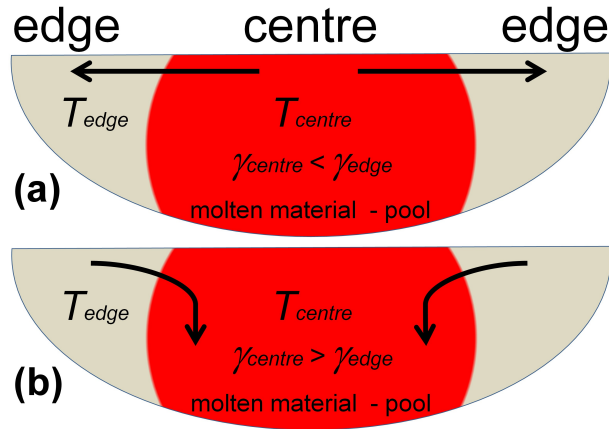


Figure 18: Schematic representation of the Marangoni convection in the case of a welding pool. The temperature of the centre is higher than the temperature at the edges (in the case of a laser e.g.). The surface tension of the centre (γ_{centre}) is the highest (a), which leads to a flow of the molten material towards the edges. Inversely, when the surface tension of the edges (γ_{edge}) is the highest (b), the flow direction changes.

and the Marangoni flow is directly affected [60]. Lu *et al.* performed bead-on-plate welding experiments on stainless steel samples. By changing the concentrations of O_2 and CO_2 (up to 0.6 vol %) in the working atmosphere, they show that the oxide layer (10 μm thickness) at the surface of the stainless steel samples acts as a barrier for oxygen absorption into the molten material and partially prevents the Marangoni convection.

Lu *et al.* also used direct laser patterning methods in order to structure silicon samples. The Marangoni convection has been reported as an effect

controlling the structuring using laser sources [61]. They used a 248 *nm* excimer laser with a Gaussian distribution in order to irradiate samples. The Gaussian profile of the intensity distribution induced a Marangoni effect in the molten area. Two effects have been observed, a thermocapillary effect which drives the matter from the hottest center to the border of the irradiated zone and a chemicapillary effect moving the material inward towards the center.

The Belgian department of metallurgy and materials engineering used selective laser melting for the fabrication of dense iron-based samples [62]. They demonstrated with their experiments and the work of Keene [63] that the surface tension of melted iron and thus the Marangoni convection were not automatically affected by the oxygen content in atmosphere.

Depending on the nature of the material, the temperature and the surface tension, the Marangoni convection can have different behaviours but clearly has an important role in the laser structuration of metallic samples.

Interference lithography is a patterning modus widely used for the structuring of thin films and bulk materials. This method permits to create periodic patterns according to a simple process where a laser beam is divided into two coherent beams which interfere in order to structure the sample. Laser interference lithography (LIL) has been combined with metal-assisted etching by a group in the Max Planck Institute of Microstructure Physics in order to produce nanowires [64]. They used the two beam configuration (the incident beam and a reflected beam) to create a sinusoidal pattern at the surface of their photoresist film. After that, the whole sample (silicon and photoresist film) was recovered by a 20 nm gold film and the photoresist and the metal were removed. Finally, the nanowires were obtained by etching process. Using this method, they experimentally developed nanostructures

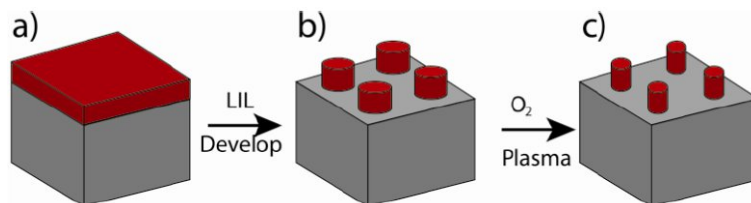


Figure 19: Laser interference lithography (LIL) combined with O_2 plasma etching is employed to produce arrays of photoresist posts [64].

with a periodicity varying from 140 nm to 1500 nm. A similar procedure was used by a group of American and Korean scientists to elaborate nanowires using laser interference lithography [65]. A polymer mask was created by using

laser interference holography in the two- or multiple-interference beam configuration. Using this periodic mask with a combination of physical vapour deposition (PVD) and chemical removal process, nanowires of different materials have been created such as Titanium, Copper etc. Authors developed a simple method of high quality for the production of nanowires in industrial quantities.

The LIL process offers numerous advantages for the surface treatment of materials. Based on the principle of interference of laser beams, almost all kinds of samples can be structured by this technique. Moreover, the LIL can be combined with others techniques such as lift-off [66] and etching techniques. The LIL procedure leads to a multiple of structure geometries (line [67], dot [68], etc.).

In the first years of this century, the laser interference metallography has been developed as an extension of the laser interference lithography. The goals of the LIMET was to reproduce patterns observed in nature on metallic materials. The tasks of the LIMET patterns were to have positive effects on the topography and micro-structure of samples [69]. It was demonstrated that the LIMET could be applied to all other types of materials: polymers [70], semiconductors [68], ceramics [71] and composites [72]. The effects of the laser interference structuring can be classified into two different categories: the topographical and the micro-structural effects. These effects have different influences: they depend on the material properties (e.g. roughness, mechanical properties) and the laser set-up (e.g. fluence, pulse number). In order to introduce the LIMET procedure and to prove its importance in the material science field, all the previous-mentioned effects are detailed in the following paragraphs.

By irradiating Ni-Al thin films using laser interference metallurgy, Liu *et al.* asserted that the laser irradiation changed the hardness of the samples [73]. Nano-indentations measurements were performed in the laser treated and untreated zones. They revealed that, in the laser-intensity-maximum area, the hardness is more than twice higher than in the untreated area. These results, which are in agreement with experiments performed in a vacuum furnace [74], confirmed that a material with periodical hard and soft properties was created.

As to micro-structural effects induced by the laser interference patterning, it has been reported that the formation of intermetallics occurs [72]. Metallic multilayer samples based on NiAl (Ni_3Al and NiAl) and RuAl materials

have been irradiated by the two beam configuration. TEM cross sections and FEM simulations showed that the melting zone of the materials was periodically distributed in the top layers according to the laser intensity profile. Due to the laser irradiation, the residual stresses and the texture distribution have been changed drastically [75]. After the laser structuring (20 pulses), the texture of the samples presents a strong orientation which is tilted in comparison with the unstructured samples. Furthermore, an evolution of the residual compressive stress is found and is dependent on the number of laser pulses as presented in figure 20.

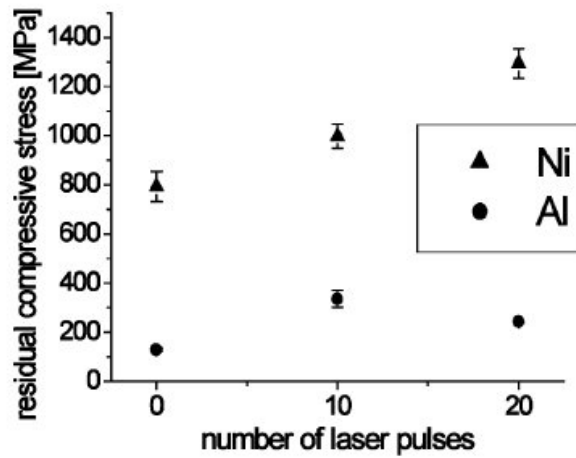


Figure 20: Calculated stress evolution in the Al and Ni phases as a function of the number of structuring laser pulses [75].

Gachot *et al.* studied the grain size and orientation evolution in thin films after LIMET process [16]. Two fluence regimes have been applied to the samples. It has been observed that significant differences appeared in the crystallization process. Three fluence regimes are distinguished: for low laser energy density, a partial melting of the sample occurs ; for high fluences, the metallic layers were completely melted. Between these two regimes, a super lateral growth phenomenon appeared: grains grew from the laser intensity minimum to the intensity maximum. Inverse pole figure maps and grain size distributions have been performed using EBSD (figure 21). They revealed that in the super lateral growth zone, a preference orientation appeared. Moreover, a significant grain growth was induced in this zone in comparison with the as-deposited state, where it was not possible to measure the grain sizes. By FEM simulation, it was established that the temperature gradient could be 3000 K broad due to the laser irradiation. This precise periodical heat distribution permitted a control of the grain orientation and grain size

distribution.

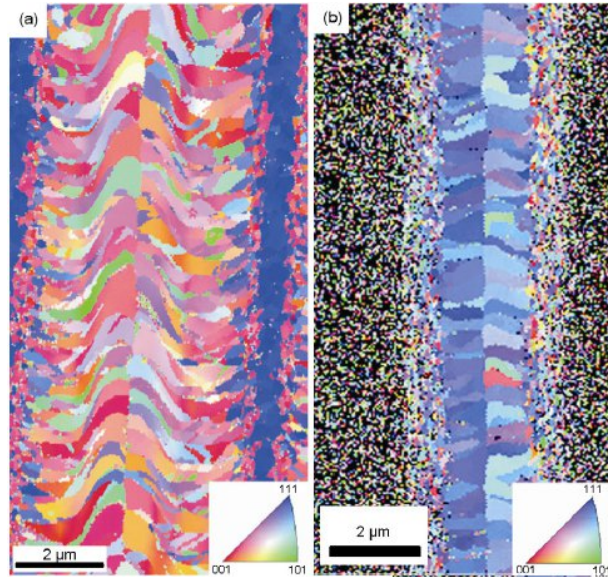


Figure 21: Inverse pole figure maps of the 300 nm thick Au (a) and Pt thin films (b) determined by electron backscatter diffraction (EBSD). The color coding goes along with the inserted orientation triangle [16]. The periodic control of the laser intensity allows a periodic grain orientation and grain size distribution on Au and Pt thin films.

In addition to the benefit of the microstructures tailoring, the LIMET procedure has been successfully used to pattern the chemical behaviour of aluminum foils by D'Alessandria [76]. Aluminum foils were textured using the two beam configuration in order to study the effect of laser irradiation depending on the laser intensity and on the laser fluence. It appeared first that by increasing the laser energy density, the oxide layer becomes thicker. Two fluence regimes can be distinguished: for low laser fluences ($< 500 \text{ mJ}\cdot\text{cm}^{-2}$), the oxide layer thickness is unchanged for laser energy minima and maxima. For high laser fluences ($> 500 \text{ mJ}\cdot\text{cm}^{-2}$), oxide layer becomes thicker at the location of laser intensity maxima. Thermal simulations reveal that oxide layer growth is proportional to the maximal laser temperature reached.

Duarte *et al.* showed in 2008 that the LIMET has also relevant effects on wear behaviour of bulk stainless steel [77]. They studied the evolution of friction coefficient under lubricated conditions for structured samples depending on the laser-pattern (line, dot, grid-patterns) and the structure depth. Compared with non-treated surfaces, the lifetime of the lubricant

layer has consistently been improved in the case of the laser structuring. Moreover, the deep structures improved more significantly the frictional behaviour than the shallow structures. Authors explained that the difference between friction coefficients for each pattern was due to the *reservoir* effect that does not exist for line-like structures. Topographical calculations of the *reservoir* density were performed using an interferometer and proved that cross patterns presented a cavity three times higher than dot structures.

Experiments performed by Hans *et al.* have demonstrated the ability of LIMET to tailor the wetting behaviour of titanium and polyimide samples [15]. The laser interference structuring has permitted to increase the statistical values of contact angles drastically: the wetting behaviour changed from hydrophilic for the initial state to hydrophobic for laser irradiated surfaces. Assuming that there was no critical influence from the surface chemistry, this behaviour can be explained by the Cassie's and Baxter's model, which consider that there is a heterogeneous wetting due to the air trapped in the pockets between the fluid and the material.

The pattern dependency for reducing friction was also demonstrated using LIMET [78]. Bulk copper samples have been structured using LIMET in order to compare the frictional behaviour of laser irradiated samples and unstructured samples: line and grid structures were generated as shown in figure 22.

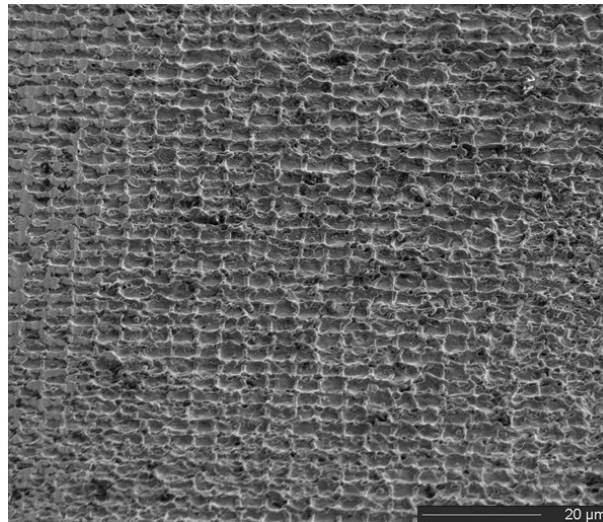


Figure 22: Grid patterns over bulk copper surfaces. The sample has been irradiated with the two-beam interference plus a sample rotation [78].

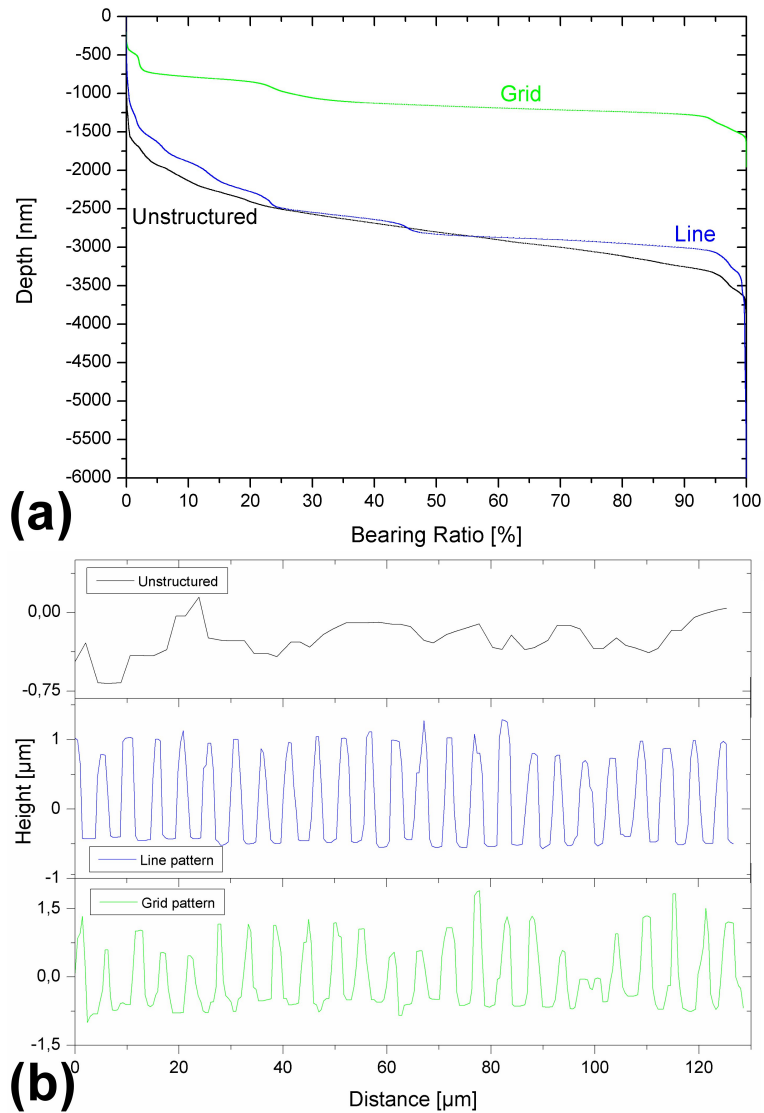


Figure 23: (a) Abbott-Firestone curves of laser structured and unstructured copper samples. They show that line structured and unstructured copper samples have a similar behaviour: line structures and asperities of the unstructured samples bear the load in a similar way. Grid patterns have a higher load-bearing capacity, which confirms frictional tests and SEM observations. (b) Profiles of unstructured and laser patterned surfaces [78].

Abbott-Firestone curves (figure 23) of structured and unstructured samples show that the grid pattern surface has a higher load-bearing capacity than the line pattern and unstructured surfaces which have a similar be-

haviour. Indeed, line patterns act as unstructured samples for bearing load due to the geometry similar to asperities. This means that the grid structure has a better load-bearing capacity and it implies that grid patterns should be less exposed to wear and friction than the other two surfaces.

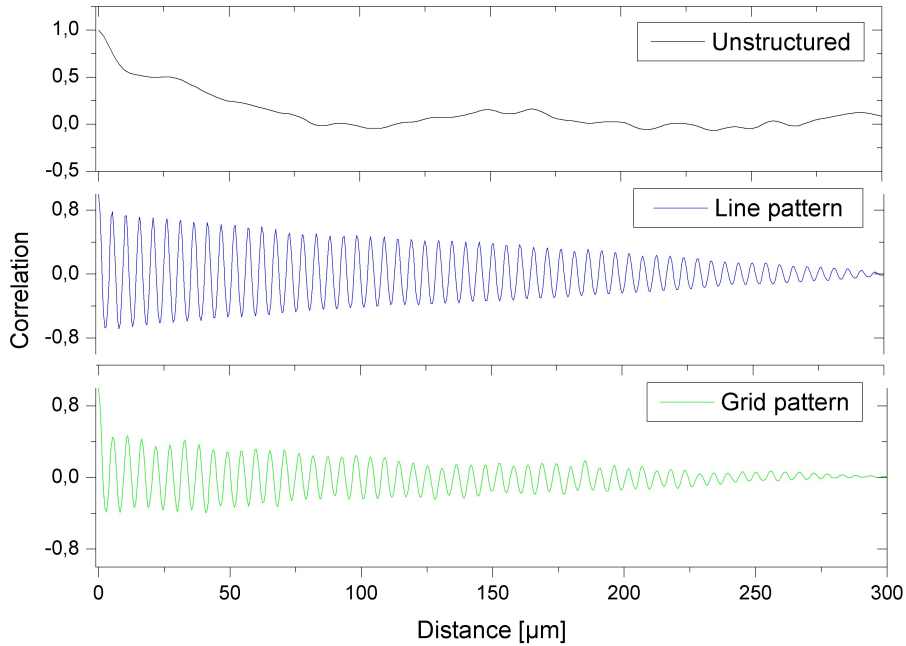


Figure 24: Autocorrelation functions of unstructured and laser structured samples. The laser structure topography oscillates homogeneously and periodically in comparison with untreated samples. The CL is shorter for grid patterns than line structures due to the double laser irradiation, which induce more irregularities in grid profiles [78].

Figure 24 represents the autocorrelation functions of line and grid patterns and unstructured samples. According to the autocovariance curves, the unstructured surface presents an irregular topography compared to the laser structured surfaces. The correlation curves of the line and grid patterns present periodic oscillations (typical for long-range-ordered structures). Hence, the laser patterns will be homogeneously deformed compared to untreated surfaces. It can be assumed that the topography of the second pass will be highly dependent on the first pass topography, only for untreated samples. The correlation length (CL) of the grid patterns is lower (2.02 mm) than that of the line patterns (3.24 mm), meaning that this configuration is less homogeneous than the line structures. This can be explained by the second irradiation necessary for grid patterns, which renders structures more

irregular.

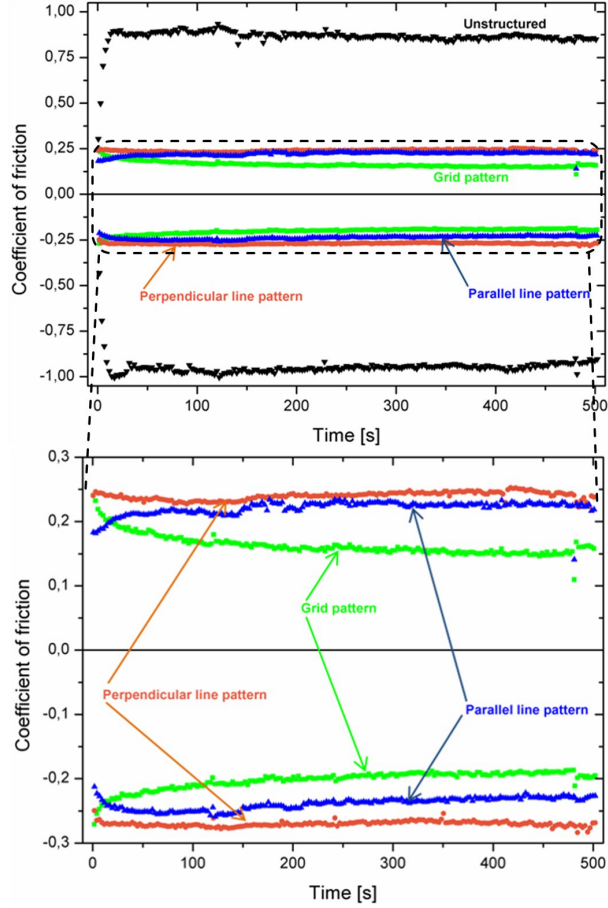


Figure 25: Friction coefficients of Cu samples depending on the structure geometry, measured in linear reciprocating mode (constant half-amplitude, load (2 mN), acquisition rate, linear speed (0.5 mm/s), stop conditions and at room temperature and humidity). Geometrical parameters (pattern and orientation) have a severe influence on the friction coefficient of copper samples [78].

Figure 25 shows the friction coefficients of non-structured and laser-structured copper samples over the sliding time. It appears that laser structures strongly decrease the friction coefficient of copper samples. Of course, it was precisely observed (figure 25) that geometrical parameters of the structures have a strong influence on the friction coefficient. Perpendicular and parallel patterns have an averaged friction coefficient of about $\mu_{perpendicular} \sim 0.26$ and $\mu_{parallel} \sim 0.23$, respectively, compared to

unstructured samples $\mu_{unstructured} \sim 0.91$. Grid patterns induce an averaged friction coefficient of $\mu_{grid} \sim 0.18$. It means that friction is reduced up to 70 % for parallel and perpendicular patterns, and grid structures reduce dry friction of copper against alumina up to 80 % in comparison with non-structured copper surfaces. Each laser structure stabilizes the friction behaviour of copper samples and provides low and constant values of the friction coefficient compared to untextured surfaces.

Wear tracks have been studied using WLI and profiles of laser structures before and after the wear tests have been plotted in figure 26. Obviously, laser patterns are in part plastically deformed by friction. The plastic deformation of the laser pattern leads to crushing and lateral expansion of laser tips. The averaged profile area of laser tips before and after friction tests has been calculated by integration in table 2. A slight difference between volumes before and after the friction test exists but has no influence on the previous observations considering the error. By multiplying this area and the constant length of the wear track (0.2 mm), the volume of the laser structure does not change due to friction. These results confirm that there is no material loss due to friction phenomena, and that the periodical structure induced by laser interference bears the load.

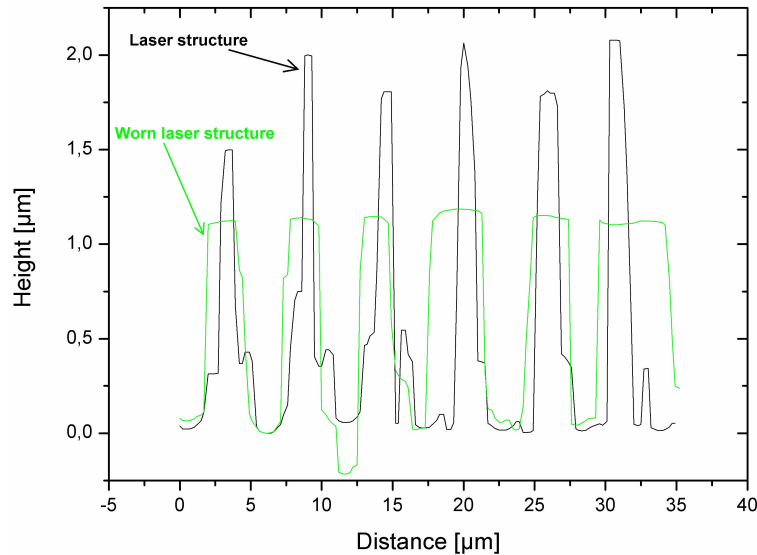


Figure 26: Surface profile comparison of laser structured samples in line configuration before and after friction measurements. Crushing and lateral expansion of the laser structure appear without material loss [78].

Figure 27 shows SEM images of worn grid structures. As reported before,

	Laser tip surface [μm^2]	Error [μm^2]	Volume of a single laser tip [μm^3]
Before friction test	3.6	1	720
After friction test	3.4	1.1	680

Table 2: Areas of laser profiles before and after friction measurement. The areas have been determined by integrating laser profiles as presented in figure 26. The volume of a laser line has been calculated by multiplying the areas by the length of the wear track. This means friction only induces plastic deformation of laser structures [78].

no wear debris is visible on the wear track. The part of the laser structure which has been plastically deformed appears in both directions: parallel and perpendicular to the sliding direction. This means that the grid structure carries the load isotropically.

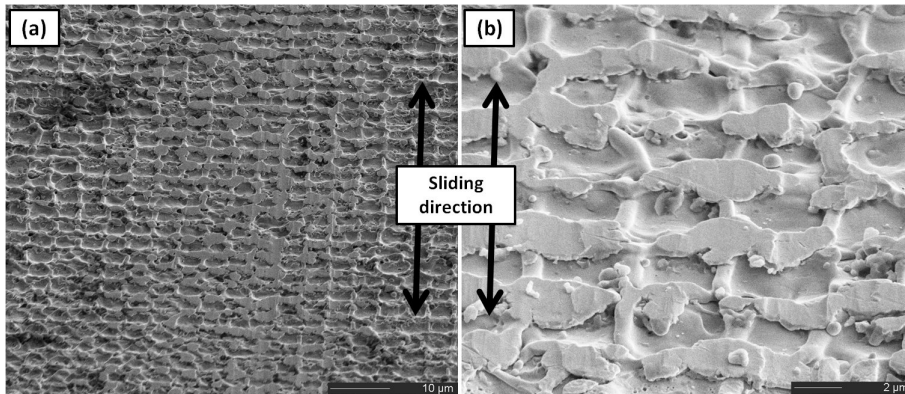


Figure 27: SEM images of grid patterns after friction testing. There is no wear debris on the surface after friction. Grid structures are in part plastically deformed parallel and perpendicular to the sliding direction. The grid structure carries the load isotropically [78].

The previous descriptive paragraphs prove that the laser interference metallurgy is a patterning method which allows a multitude of application possibilities. In addition to these advantages, the LIMET shows its ability to produce functionalized surfaces at a relative big scale in a short time and under room conditions.

2.2 Wetting phenomena and wettability: influences of the surface and fluid properties

2.2.1 Wettability models: Young, Wenzel, Cassie Baxter, de Gennes

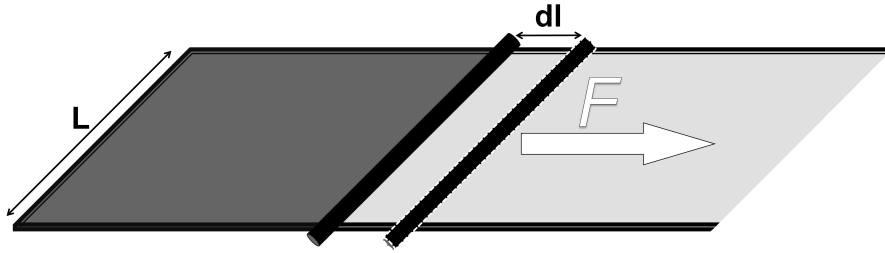


Figure 28: Schematic representation of a soap water mixture. The mixture is trapped but when the free side moves, it reduces the film area and a force F is applied to keep the film surface constant. This experiment shows the surface tension phenomenon.

Figure 28 shows a soap water mixture trapped inside a quadratic channel with a free side to move. When the free side of the film moves, it tends to reduce the film area. Then a certain force F , proportional to the channel width L is necessary to keep the film surface S constant. In order to increase this surface of $dA = Ldl$, an energy dW is necessary and corresponds to:

$$dW = Fdl = 2\gamma Ldl = 2\gamma dA \quad (14)$$

γ is the surface tension and is exprimed in $\text{N}\cdot\text{m}^{-1}$ or $\text{J}\cdot\text{m}^{-2}$ in SI.

Using the equation 14, the surface tension is expressed as:

$$\gamma = \frac{F}{2L} \quad (15)$$

The surface tension of water at 20 °C is $\gamma = 72 \text{ mN}\cdot\text{m}^{-1}$.

Most of the interfaces are naturally curved and the equilibrium of the system can be achieved only if there is a pressure gradient which permits to pass through the curve. In the middle of the 18th century, a German medical scientist showed that when a water droplet gets in contact with a straw, the water droplet raises up. He understood that a certain pressure permitted

the movement of the droplet. Around fifty years later, Laplace could calculate this pressure. Considering a spherical droplet at the equilibrium on a surface, the droplet has a pressure p_d higher than the ambient pressure p_0 . The droplet does not have a perfect round shape like it was schematically represented on the figure 29. The equilibrium of the pressure and the ten-

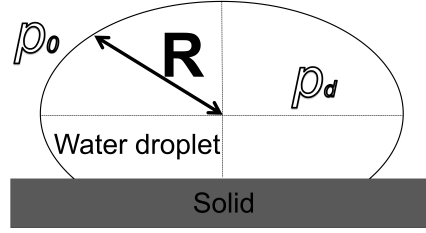


Figure 29: Schematic representation of a water droplet at the equilibrium (radius R and pressure p_d) on a solid surface. The equilibrium of the pressures and forces allows the calculation of the Laplace pressure.

sion forces acting on the droplet have to be calculated. So the equilibrium between external dW_0 and internal dW_d forces is given by the equation 16 as:

$$dW_{ext} = dW_{int} \quad (16)$$

With the pressure forces given by:

$$dW_{ext} = -F_0 dR + F_d dR = 4\pi R^2 dR (p_d - p_0) = 4\pi R^2 dR \Delta p \quad (17)$$

and the increase of surface tension energy:

$$dW_{int} = 8\pi\gamma R dR \quad (18)$$

Indeed if the radius R of the droplet increases of dR , the surface increases of $8\pi R dR$.

So the equation 16 becomes:

$$4\pi R^2 dR \Delta p = 8\pi\gamma R dR \quad (19)$$

and the gradient of pressure between the droplet and the atmosphere is:

$$\Delta p = \frac{2\gamma}{R} \quad (20)$$

This equation 20 gives the Laplace equation. For a general case, it becomes:

$$\Delta p = \gamma \left(\frac{1}{R_d} + \frac{1}{R_{surf}} \right) \quad (21)$$

where γ is the surface tension and R_d and R_{surf} are the curvature radii of the droplet and the surface respectively. The Laplace equation is the gradient of pressure in a point at the interface.

The wetting of a liquid on a surface can be described using the *spreading parameter* S which compares the surface energies of a system. It permits to define if the wetting is total or partial. Marangoni was the first to compare the surface energies. S is given by the following equation:

$$S = \gamma_{SV} - \gamma_{SL} - \gamma_{LV} \quad (22)$$

γ_{SV} , γ_{SL} and $\gamma_{VL} = \gamma$ are the surface tensions of the solid-vapor, solid-liquid and liquid-vapor phases respectively.

Two cases can be distinguished:

- $0 < S$, means that the spreading is total, $\gamma_{SL} + \gamma_{LV} < \gamma_{SV}$, the liquid covers the maximum of the solid surface.

- $S < 0$, the spreading is described as partial: $\gamma_{SV} < \gamma_{SL} + \gamma_{LV}$. In this case the solid has a low surface energy, which does not allow the liquid to wet the surface.

In the case of a partial wetting ($S < 0$) of a small droplet on a surface, it can be observed that the gravity force does not affect its shape profile. Considering that a droplet does not completely wet the surface, its pressure p_d is given by the Laplace equation 23:

$$p_d = p_0 + \frac{2\gamma}{R} \quad (23)$$

A certain contact angle exists at the triple line location as represented on the picture 30. This contact angle is given by Young's law which uses the projections of the three surface tensions γ_{SV} , γ_{SL} and γ_{LV} as represented on

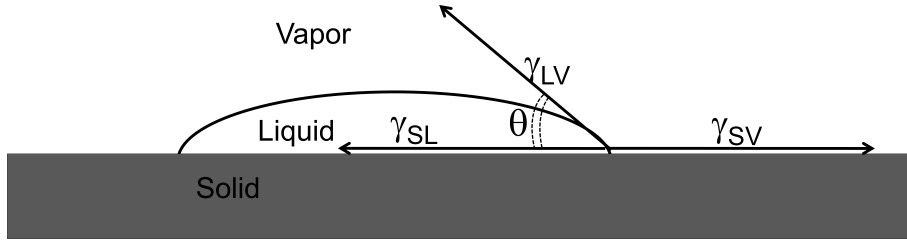


Figure 30: Representation of the surface tensions at the triple line location related to the equation of Young.

the previous picture.

At this point, the equilibrium is:

$$\gamma_{SL} + \gamma_{LV} \cos \theta = \gamma_{SV} \quad (24)$$

so the contact angle θ is related to the surface tensions by:

$$\cos \theta = \frac{\gamma_{SV} - \gamma_{SL}}{\gamma_{LV}} \quad (25)$$

The contact angle can also be described using the spreading parameter as:

$$\cos \theta = 1 + \frac{S}{\gamma_{LV}} = 1 + \frac{S}{\gamma} \quad (26)$$

In the case of a partial spreading, certain systems can be affected by gravity. In this case, the profile of the droplet is not spherical anymore but becomes flat and can be described as a puddle as schematically represented in figure 31. The droplet is flat except at the edges (location of the triple line). This profile is due to the simultaneous action of the gravity forces to spread the liquid and the surface tensions which prevent the wetting.

The equilibrium of these forces can be written as:

$$P = -S \quad (27)$$

with P the pressure or gravity force tending to flatten the droplet

$$P = \frac{1}{2} \rho g h^2 \quad (28)$$

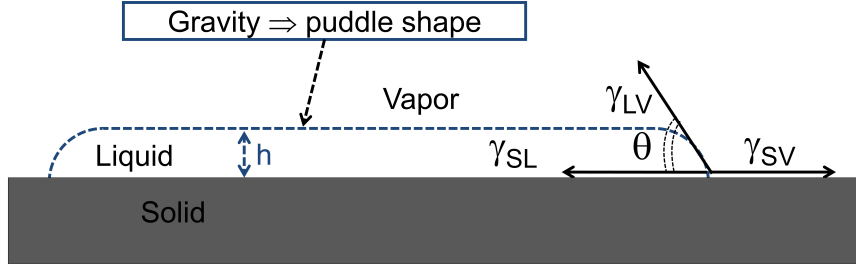


Figure 31: Representation of a droplet affected by the gravity. The droplet has a puddle shape profile due to the gravity. h is the thickness of the puddle and can be calculated at the equilibrium.

with ρ the density of the liquid expressed in $[kg/m^3]$, g the gravity acceleration in $[m/s^2]$ and h the thickness of the puddle in $[m]$.

The thickness of the puddle can be calculated as:

$$h = \sqrt{\frac{-2S}{\rho g}} \quad (29)$$

and using the equation 26, h becomes:

$$h = 2\kappa^{-1} \sin \frac{\theta}{2} \quad (30)$$

with κ^{-1} the capillary length given by the following equation:

$$\kappa^{-1} = \sqrt{\frac{\gamma}{\rho g}} \quad (31)$$

The capillary length permits to determine which force is dominant in a system submitted to the capillary and gravity forces.

The extreme case opposed to the total wetting is the so-called *non-wetting*. This case corresponds to the surfaces described as superhydrophobic. Figure 32 shows an example of a superhydrophobic surface achieved by Onda *et al.* [79]. They produced fractal surfaces made of alkyketene dimer (AKD), which present a super-water-repellent behaviour leading to a 174° contact angle. The non-wetting of surfaces can be interesting for

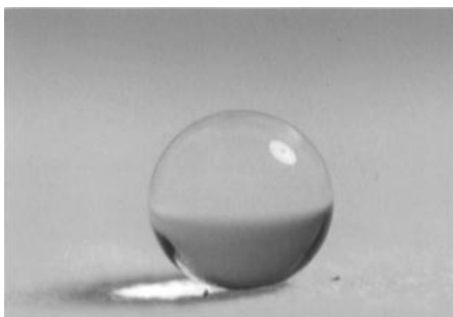


Figure 32: Water droplet on fractal AKD surface ($\theta_f = 174^\circ$), the fractal AKD surface achieved by Onda *et al.* has a superhydrophobic behaviour [79].

certain systems such as a water droplet on a tissue surface. In order to trigger this behaviour, the substrate has to be hydrophobic first ($\theta < 90^\circ$). The roughness of the surface is also a crucial point, which permits to trap air and create a composite surface as it has been described by Cassie-Baxter in 1944 [80]. The Cassie-Baxter model will be developed in a further paragraph.

In 1936, Wenzel proposed a model to explain and understand the influence of a rough surface on the spreading of liquid [81]. He affirmed that "*the wetting properties of a solid substance should be directly proportional to the roughness of the surface wetted*". He explained that a solid with asperities offers more surface than a flat sample and "*therefore a greater intensity of surface energy*".

Considering a liquid deposited on a chemical-homogeneous and rough surface, the apparent contact angle is given by Young's law (calculated in the equation 25). The dimensions of the asperities have to be considered as very small in comparison to the droplet dimensions. The roughness-factor Rf is introduced as the ratio of the real area A_{real} on the apparent area $A_{apparent}$ and is related to the interface solid-liquid.

$$Rf = \frac{A_{real}}{A_{apparent}} \quad (32)$$

When Rf equals 1 ($Rf = 1$), the solid can be considered as perfectly smooth and the apparent contact angle (θ_{app}) is equal to the real contact angle (θ_{real}). In this case, Young's law is correct:

$$\gamma_{SL} - \gamma_{SV} = \gamma_{LV} \cos \theta_{real} \quad (33)$$

When Rf becomes higher than 1 ($Rf > 1$), the real area is higher than the apparent area and the roughness-factor has to be introduced as:

$$Rf(\gamma_{SL} - \gamma_{SV}) = \gamma_{LV} \cos \theta_{app} \quad (34)$$

The Wenzel equation is then given by the combination of the equations 33 and 34:

$$\cos \theta_{app} = Rf \cos \theta_{real} \quad (35)$$

This theory is not available for all systems: a rough surface with a superhydrophobic behaviour cannot be explained by the Wenzel model. The Cassie-Baxter model developed in the next paragraph proposes a better approach.

In 1944, Cassie and Baxter published their study *Wettability of porous surfaces* which extends the work of Wenzel [80]. Their model described the wetting behaviour of chemical or topographical heterogeneous surfaces. In the equation of energy, they introduced the roughness-factor and a similar factor (ϕ) for the liquid-vapor interface defined as the "*total area of liquid-air interface in a plane geometrical area of unit parallel to the rough surface*". This factor can also be described as the surface fraction of solid under the liquid. By adding these two factors, "*the net energy, E_D , expended in forming unit geometrical area of the interface*" is given by the equation 36:

$$E_D = Rf(\gamma_{SL} - \gamma_{SV}) + \phi\gamma_{SV} \quad (36)$$

The Cassie-Baxter model introduces in the calculation of the apparent contact angle of Wenzel, the surface fraction of solid under the liquid as:

$$\cos \theta_{app} = Rf \cos \theta_{real} - \phi \quad (37)$$

The parameters Rf and ϕ presented in the Cassie-Baxter model can be changed in order to control the wetting behaviour. The design of certain geometrical parameters such as, structure pattern, depth, periode etc. and the distribution of chemical species such as oxides (e.g. aluminum, iron, chromium oxides) can influence these Rf and ϕ parameters.

When a liquid wets a surface, the wetting behaviour can be static or dynamic. This section will focus on dynamic wetting. The dynamic wetting

can be easily described as the triple line which is moving at a certain speed on the surface and leads to a non-equilibrium state.

In 1975, Hoffman found an empirical relation between the dynamic contact angle and the spreading speed of the fluid [82]. He studied the advancing liquid-air interface in a glass capillary for various oils. He expressed the contact angle θ in function of the capillary number Ca given by the following equation:

$$Ca = \frac{\eta V}{\gamma} \quad (38)$$

with η the dynamic viscosity of the fluid, γ the surface tension and V the speed.

This equation reveals that the contact angle increases according to a logarithmic function and depends on the speed of the triple line.

In 1985, Pierre Gilles de Gennes published a review called *Wetting: statics and dynamics* describing the hysteresis of the contact angle and the spreading of liquids due to physical and chemical effects such as the orientation of the surface roughness and the presence of impurities [83]. Given a rough surface with periodic line patterns, the lines are considered

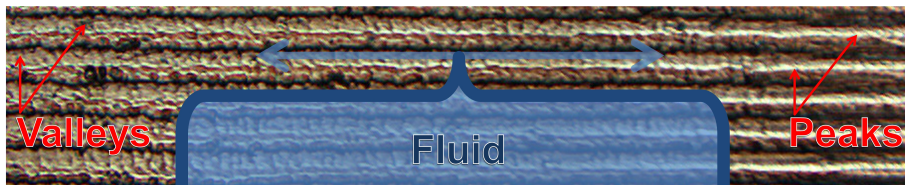


Figure 33: Overlapping process proposed by Pierre Gilles de Gennes [83]. When the triple line is parallel to the periodic grooves, the triple line gets over the peak in a single point only. Then, the liquid spreads inside the groove (valley) as represented.

to be infinite in a direction as schematically presented in figure 33. First of all, the liquid is spreading in the direction perpendicular to the periodic lines (i.e. the triple line is parallel to the periodic grooves). In this case, the triple line is partially trapped in the parallel grooves and "*it is pinned*" as exposed by de Gennes. The overlapping of the structures is shown in the schematic representation in figure 33. As described by de

Gennes, "*the optimal method [...] is not an overall jump*" along the infinite length of the grooves because this would imply a "*huge barrier energy*" to overtake. The triple line gets over the groove only in a single point, where it costs the less energy (this point can be a defect in the structure such as a lack in a physical pattern or in a chemical barrier), this is the cost-efficient energy solution. Once the groove is passed, the liquid spreads in orthogonal direction inside the groove without any pinning.

This case is the other extreme configuration which takes place when the triple line forms a 0° angle with the line patterns. It has been studied and shown by Mason in 1978 [84].

It has to be noticed that for certain geometrical configurations such as deep grooves and a short pattern period, a composite interface can appear being in agreement with the Cassie-Baxter model described previously.

2.2.2 Wetting on chemical surfaces

The chemical species presented on a surface can have a strong influence on the spreading behaviour of the fluid. In the case of a homogeneous flat surface (i.e. without any influence of the roughness), the space distribution of chemical species is the key parameter to understand the wetting phenomena. The presence of chemical elements has different origins: they can be generated, for example, due to the elaboration of the material, due to the ambient atmosphere, due to a reaction between the fluid and the substrate etc. The impact of chemical active surfaces on the surface tension is proven fact. It has to be affirmed that, as pointed out by Berg "*only the uppermost surface [...] governs wetting behaviour*" [85]. In this case, the study of the first surface layer is essential. In the present paragraph, the previous mentioned origins and their potential applications will be described in detail.

In 1999, Abbott *et al.* published a work based on the wettability of pyrimine-coated surfaces [86]. Gold substrates (99.99 %) were coated with photoresponsive pyrimidine-terminated molecules and they were irradiated by UV light at 280 and 240 nm resulting in a reversible photodimerization. Contact angles were determined using the sessile drop method and these measurements revealed a fluctuating behaviour of the contact angle depending on the irradiation state.

In a similar way, Lahann *et al.* reported the elaboration of gold surfaces (Au(111)) covered with (16-Mercapto)hexadecanoic acid (MHA) molecules [87]. They observed a change in the wetting behaviour of their samples when applying an electrical potential. Indeed, the electrical potential induces the attraction of negatively charged carboxylate groups to the gold substrate leading to a transition from the hydrophobic to a hydrophilic behaviour of the chains.

As described previously, the chemical elements that exert influence on the spreading of fluids have different origins, Landry and Eustathopoulos studied the wetting behaviour of a drop of molten aluminum (99.99%) on vitreous carbon substrates [88]. The experiments consisted of measuring contact angles by the sessile drop method in a controlled atmosphere (high vacuum metallic furnace). Results showed that the basis-size of the droplet was varying in time according to different regimes. Authors found that these kinetics of spreading were due to the growth of aluminum carbide (Al_4C_3) at the triple line. Indeed, the formation of aluminum carbide induced an increase

of the roughness compared to the initial state, which was also responsible for the variation in spreading kinetics.

The pore filling of carbon samples was studied by László *et al.* using a small-angle X-ray scattering [89]. Activated carbons samples were filled using polar (water) and non-polar (n-hexane) molecules. While the hexane molecules uniformly fill the pores, water filling is partial. The authors established that the presence of adsorbed molecules changes the pore filling depending on the nature of the fluid and is logically influenced by the relative humidity. While Kietzig *et al.* focused on structuring the surface of metallic samples, they detected an increase of carbon after the laser irradiation procedure using XPS. Indeed, carbon appears at the surface by the femtosecond laser treatment of metallic alloys. Authors suggested that the carbon presence is due to the fast decomposition reaction. Because of the transition from hydrophilic to superhydrophobic behavior, it is assumed that the amount of carbon plays a significant role in this time-dependent behaviour. Finally, it is important to notice that the presence of carbon and the dual scale roughness leads to a combined effect on the wetting behavior.

The effects of roughness and topographical textures are described in detail in the next section.

2.2.3 Wetting on textured surfaces

As previously described, the spreading mechanisms and kinetics of fluids can be controlled by the presence of chemical-active elements at the surface of samples. In the present section, different effects of topographical patterns on the surface of samples will be presented. In 1980, Oliver and Mason studied the influence of roughness on the wetting of liquids on aluminum and stainless steel samples [90]. They used ethylene glycol and silicone oil as lubricant in order to study the spreading behaviour on naturally rough and structured metallic surfaces and were prepared using lathe-machining, universal-grinder, polishing- and etching-procedures. Assuming that the contact angle hysteresis was attributed to surface roughness, authors proved that the "*orientation and texture of roughness*" induced by the common practical procedure have a strong influence on the spreading and wetting behaviour acting as capillary channels. Moreover, they also supposed that microscopic roughness asperities play a determinant role in the extensive wetting hysteresis during drop retraction.

2.2.4 Effects of fluid properties

In this section, a short state-of-the-art will describe the effects of fluid properties having an influence on the wetting behaviour.

Fluid properties such as viscosity and chemical composition have a strong influence on tribological behaviour. As a simple example, the dynamic viscosity of a fluid used for tribological experiments has to be taken into account for the calculation of the so called *Stribeck curve* [91]. The chemical composition of lubricant also plays a very important role in the case of lubricated friction. Indeed, the additives present in engineering oils (most of them are motor oils) have strong effects on the behaviour of the system, such as increase of the bearing performance, decrease of the friction coefficient, cleaning engine internals, reduction of heat phenomena and of the fuel consumption [92].

The influence of liquid viscosity was studied by Yang *et al.* [93]. They performed static contact angle measurements on three different substrates with different surface roughness: silicon wafer ($0.047 \mu\text{m}$), aluminum ($0.326 \mu\text{m}$) and wax ($1.284 \mu\text{m}$). Five different liquid mixtures composed of water and glycerol were used. Final images of contact angles performed with deionized water (dynamic viscosity: $\mu = 0.89 \text{ mNs}\cdot\text{m}^{-2}$) show that contact angle increases with the roughness. Experiments performed with pure glycerol, which has a higher viscosity ($\mu = 916.2 \text{ mNs}\cdot\text{m}^{-2}$) and a lower surface tension ($\gamma = 63.5 \text{ mN}\cdot\text{m}^{-1}$) showed that the droplets present "*almost the same contact angles on all three substrates*". This static behaviour is mainly due to the viscous dissipation and was described as proportional to the liquid viscosity by de Gennes [83]. As the viscosity increases, more energy is required for the spreading of the fluid.

Recently, Keller *et al.* studied the dynamic contact angle of petroleum hydrocarbons and silicon oils [94]. Viscosities of the fluids ($T = 25 \text{ }^\circ\text{C}$) varied from $14 \text{ mNs}\cdot\text{m}^{-2}$ to $487 \text{ mNs}\cdot\text{m}^{-2}$ for the hydrocarbons and were $50 \text{ mNs}\cdot\text{m}^{-2}$ and $975 \text{ mNs}\cdot\text{m}^{-2}$ for the oils. With their experiments authors found that at low velocity (below $150 \mu\text{m}\cdot\text{s}^{-1}$), the variation of the advancing contact angle is proportional to the oil viscosity, while at higher advancing velocities (175 and $275 \mu\text{m}\cdot\text{s}^{-1}$), the contact angles are stable for almost all the fluids. The spreading behaviour of *HydroCal 300* oil presented stable contact angles values (up to $80 \mu\text{m}\cdot\text{s}^{-1}$) at the temperature $T = 25 \text{ }^\circ\text{C}$ when the velocity was increasing. Authors attributed this wetting stabilization to the chemical composition of the oil. Indeed, as the *HydroCal 300* oil is a commercial product, its lubrication properties were improved by adding some additives.

3 Experimental

The 100Cr6 bulk metallic samples studied in this thesis were delivered by the factory-service of the faculty of Materials Sciences. The fluids and their properties used in this study for the contact angle measurements were also briefly described. The metallographic preparation and the laser structuring procedures are reported in the present chapter. For reliability reasons, details on the optics and parameters used for the laser patterning of the sample are given below. The topographical and microstructural effects produced by the laser irradiation were characterized using White Light Interferometer (WLI), Scanning Electron Microscopy (SEM), X-Ray Photoelectron Spectrometer (XPS), Raman spectrometer and Atom Probe Tomography (APT). Finally, the wetting behaviours of the specimens were characterized by measuring the corresponding surface tension and the contact angles.

3.1 Materials

3.1.1 100Cr6 steel, metallographic preparation

The 100Cr6 bearing steel provided by the factory service has the following chemical composition reported in table 3. This composition was checked and confirmed by means of Electron Dispersive X-ray Spectroscopy (EDX/EDS) at the chair of Functional Materials.

Elements	Measured concentrations	Saarstahl concentrations
	[wt.%]	[wt.%]
C	0.93 - 1.05	1.00
Cr	1.35 - 1.60	1.50
Mn	0.25 - 0.45	0.35
Si	0.15 - 0.35	0.25

Table 3: Chemical composition of the 100Cr6 steel estimated by a standard energy dispersive spectroscopy (EDS) and given by the steel producer Saarstahl AG.

Due to the as-delivered-state of the samples, which presented an important and randomly distributed roughness, the surfaces have to be prepared by metallographic methods. The samples were grinded and polished using diamond suspensions. The surfaces have to be as flat as possible regarding the laser structuring and the wetting analyses which are described in detail in the following chapters.

3.1.2 Fluids

The wetting measurements were performed using two different fluids: distilled water and FVA 2 oil.

The distilled water used was a standard water delivered by the faculty service for chemical experiments.

The FVA 2 oil is provided by BP and is described as a reference-oil for friction measurements. The FVA 2 is a mineral, solvent-refined oil and its PAC (polycyclic aromatic compounds) content is lower than 3% according to the IP 346 method developed by the Institute of Petroleum. The properties of these two fluids are given in the table 4. The cinematic viscosity and density values are given by the literature, while the surface tensions were measured with a standard drop shape analyzer (Krüss DSA 100) [95]. The measurements were performed in air under room conditions ($T \sim 20$ °C, $RH \sim 25$ %).

	Distilled water	FVA 2 oil
Cinematic viscosity (@ 40 °C), [mm^2/s]	0.661	32
Density (@ 15 °C), [kg/L]	0.999099	0.870
Surface tension (@ 20 °C), [mN/m]	71	30

Table 4: Properties of the water and FVA 2 fluids. The properties of the FVA 2 are given according to the BP data. The surface tension of the liquids was measured before each measurement under room conditions at a constant temperature.

3.2 Laser

In the present section, the structuration principles and set-up used with the nanosecond and femtosecond laser are described.

3.2.1 Nanosecond Nd:YAG laser

LIMET is based on the interference principle of laser beams from a high-power pulsed laser. The period (P) of the line pattern structure is a function of the angle between the laser beams (2α) and the wavelength (λ) as described by the figure 35 and written in the equation 39.

$$P = \lambda/2 \sin \alpha \quad (39)$$

Laser interference experiments were conducted using a high-power pulsed Nd:YAG laser (Quanta-Ray PRO 290, Spectra Physics). Four different wavelengths can be generated, the fundamental 1064 nm and three harmonic wavelengths: 532, 355 and 266 nm. The samples were irradiated with the 355 nm wavelength (figure 34) in order to reach the absorption range of our materials and to prevent excessive reflection. The pulse duration is 10 ns and

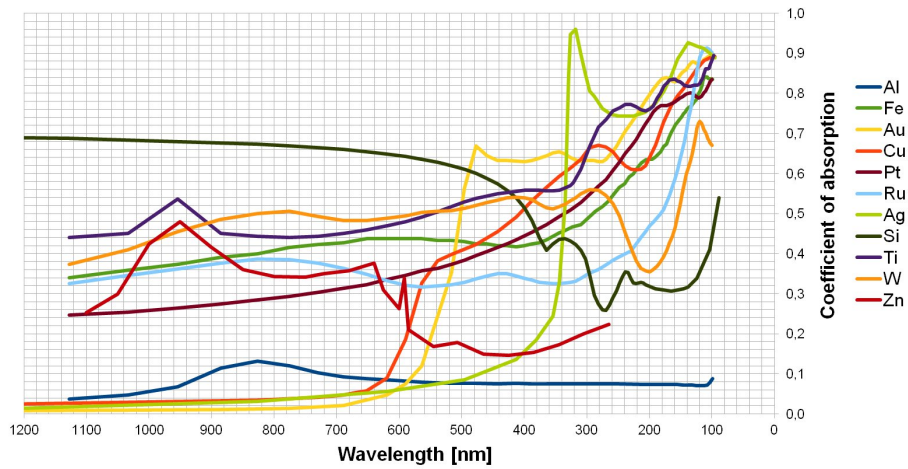


Figure 34: Curves of the absorption coefficients for different materials depending on the wavelength [96]. The 355 nm wavelength was set-up for the laser irradiation of all the samples.

the repetition rate is 10 Hz. The typical spot area is between 2 and 4 mm² with a beam diameter of 10 mm at the source. Each sample was treated under room temperature and atmosphere. In figure 35, the laser interference experimental procedure is shown. The emitted laser beam first goes through a tunable attenuator in order to control the power of the laser beam. A lens permits to focus the beams at a desired focal length. The mask allows to modify the size and the form of the irradiated area. The beam splitter divides and directs the main laser beam into two similar sub-beams. The two former beams are finally focused at the surface of the sample using mirrors. The two beam configuration provides line patterns.

The laser experiments were conducted at different laser fluences (energy per unit area), which were varying from about 1500 to 2500 mJ·cm⁻². For all the produced structures, a single pulse was used.

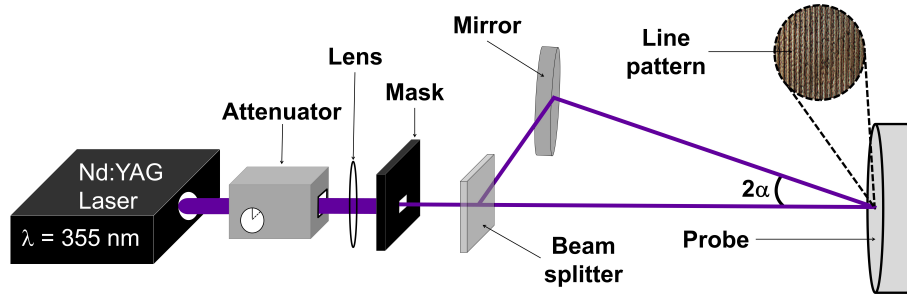


Figure 35: Schematic representation of the LIMET set-up in a two-beam interference configuration. The primary laser beam is focused by a lens, and then split into two different sub-beams and reflected on a mirror forming an 2α angle. Finally, both of them interfere on the sample surface and in the two beam configuration it leads to the formation of the line patterns as shown in the light microscope micrograph.

3.2.2 Femtosecond Ti:sapphire laser

Femtosecond laser ablation has been performed in air using a linear p-polarized Ti-sapphire laser (Spitfire Pro, Spectra Physics). The pulse duration of the laser was estimated using an optical autocorrelator and was approximately 470 fs. The laser wavelength was 800 nm and the repetition rate 1 kHz. The femtosecond laser was used in order to create precise and periodic hole patterns. The set-up for the laser irradiation is presented in the figure 36. The laser beam passes through a standard shutter (Uniblitz) and an aperture with definable diameter. It is then focused with a planoconvex lens with focal length (FL) of 74.3 mm and a diameter of 25.4 mm. The power of the laser beam was measured using a power meter and the sample was moved using a 2-axis stage (Newport). The fluence was kept constant at about $27.4 \text{ J}\cdot\text{cm}^{-2}$ for each structure configuration, and the number of pulses was varied in order to achieve different hole-depths. The diameter was fixed by adjusting the aperture and the period was set with the 2-axis stage.

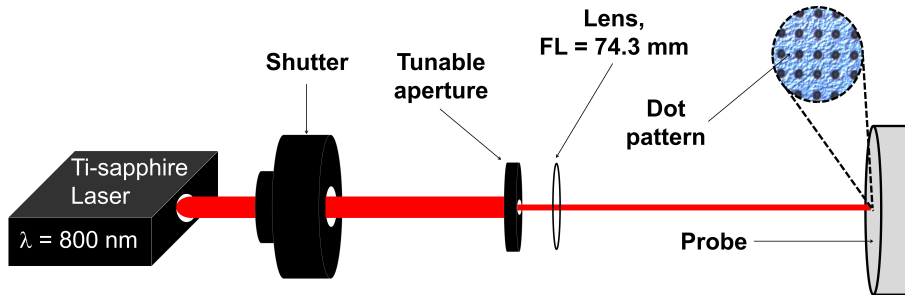


Figure 36: Femtosecond laser set-up for the ablation process. The laser power is controlled by a power meter. The main laser beam goes through a standard shutter, the diameter of the irradiated zone is controlled by a tunable aperture. The laser beam is focused by a lens with a focal length (FL) of 74.3 mm. The number of pulses is changed depending on the desired depth of the structure [78].

3.3 Characterization techniques

3.3.1 White light interferometer

The topography of the samples was first performed using a white light interferometer provided by Zygo (NewView 200) and mounted with a *3D Imaging Surface Structure Analyzer*. The WLI is equipped with different objectives (5, 10, 20, 40) and several magnification values are available (0.5, 0.75, 1, 1.5, 2). The WLI is a profilometer (three-dimensional optical surface profiler) based on the Michelson's interferometer. The geometrical parameters such as depth, period etc., the roughness parameters and the bearing properties (Abbott Firestone curves, core roughness depth e.g.) were characterized using the WLI. Root-mean-square roughness (R_q /rms) was used to characterize the roughness of the sample. R_q is defined as:

$$R_q = \sqrt{\frac{1}{L} \int_0^L z^2(x) dx} \quad (40)$$

with L the sampling length, z the variable height and x the variable position on L .

Bearing ratio parameters and Abbott-Firestone curves characterize bearing properties of surfaces and successfully simulate the effects of wear [97]. Figure 37 shows an ideal representation of the Abbott-Firestone curve and the main parameters for the characterization of the bearing behaviour. The load-bearing capacity and the oil retention ability of the structures can be compared for each configuration. Zygo defines the bearing ratio as "the ratio

of the length of the bearing surface at any specified depth in the evaluation area. It simulates the effect of wear on a bearing surface". R_k is the core roughness depth and as its value increases, its load-bearing capacity decreases. R_{pk} and R_{vk} are the reduced peak height and reduced valley depth, respectively. R_{pk} gives information on the erosion of peaks and R_{vk} on the ability of the surface to retain lubricants. The WLI allows clear and precise characterizations of the sample surfaces due to a sub-nanometer vertical resolution. Two-dimensional profiles of the laser patterns were also performed using the WLI.

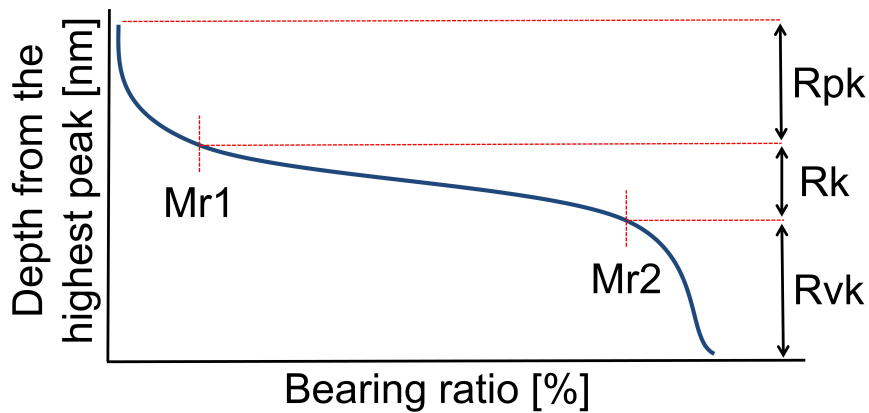


Figure 37: Schematic representation of an Abbott-Firestone curve. The bearing ratio varies as a function of the depth from the highest peak.

3.3.2 FIB/SEM Dual beam workstation

Two FIB/SEM (focused ion beam/scanning electron microscope) dual beam workstations which are a combination of a FIB and a SEM were used for the site-specific milling and imaging of the samples. Imaging, electron backscatter diffraction (EBSD) and the preparation of atom probe specimens (perpendicular to the surface) using FIB were carried out in a FEI Strata DB 235 system and a FEI Helios 600.

3.3.3 X-ray photoelectron spectrometer

X-ray photoelectron spectrometer (XPS) measurements were performed at the chair of Soft Condensed Matter Physics of the Saarland University. Due to its high-surface sensitivity (1-2 nm), XPS was used to study the elemental

composition of the samples and combined with surface ion etching it was possible to get depth profiles of the elemental composition (stoichiometry) and the valences of the elements [98, 99]. The XPS data was recorded with an ESCA Lab Mk II photoelectron spectrometer (by Vacuum Generators, Hastings, England) using Al-K α radiation ($h\nu = 1486.6$ eV) in normal emission mode (take-off angle along the surface normal) in ultra high vacuum ($\sim 10^{-10}$ mbar).

3.3.4 Raman spectrometer

Confocal Raman spectroscopy was performed with a LabRAM ARAMIS instrument from HORIBA using a 532 nm laser beam without a filter. The Raman microscope uses a backscattering geometry, where the incident beam is linearly polarized and the spectral detection unpolarized. The slit and hole sizes were 100 and 1000 μm , respectively. The Olympus Mplan objective lenses were used. The information depth depends on the optical lens used in the microscope, thus, by using confocal geometry it is possible to obtain information from only the first few micrometers.

3.3.5 Atom probe tomography

The samples structured with femtosecond laser were analyzed using atom probe tomography (APT). The APT is defined by Larson and Kelly as "the highest spatial resolution analytical technique in existence" [100]. The APT allows three-dimensional reconstruction of samples at the atomic scale. For the APT measurements, the ions were detected using a CAMECATM LEAP(local-electrode atom-probe) 3000X HR system in laser pulsing mode with 250 kHz pulse frequency and a specimen base temperature of about 50 K. It was critical to have the specimens stable during field evaporation along the transition zone (Ni-to-steel), therefore thermal pulsing was used to reduce induced mechanical stresses inside the specimen [101]. Laser pulse energies of 0.8 - 1 nJ were applied with a 532 nm wavelength laser.

3.3.6 Transmission electron microscopy

Transmission electron microscopy analyses were performed using a CM 200 electron microscope (Philips, Netherlands) operating at 200 keV at the department CP2S of the Institute Jean Lamour, Nancy, France. This study was performed on non-irradiated samples and femtosecond laser treated samples

in order to study the cristallinity of the different zones. The TEM lamellae were prepared by FIB in situ lift-out technique. The matter was milled at different speeds (i.e. different currents) in the sample zone of interest until getting a thin and fine lamella. This lamella was then extracted and set on the sample holder.

3.3.7 Contact angle

The contact angle (CA) and interfacial tension (IFT) measurements were performed with a standard drop shape analyzer (Krüss DSA 100). CA experiments were performed in static and dynamic modes for distilled water and FVA 2 oil, respectively. Room temperature (~ 20 °C) and relative humidity (~ 50 %) were stable and constant. The experimental parameters used for the two fluids were different due to their surface tensions. The drop volume was 7 and 6 μL and the deposition rate used was 100 and 200 $\mu\text{L}\cdot\text{min}^{-1}$ for water and oil, respectively. The samples were all ultrasonically cleaned in cyclohexane, acetone and ethanol before assessing their hydrophobic and oleophilic wettability. Once the droplet was deposited on the sample, videos were recorded. In both cases (distilled water and oil), the contact angle was calculated each second during 6 s. The measurement duration was chosen after experimental considerations: the water droplets were in a steady state after 6 s and it was almost impossible to determine the profile of the oil after 6 s. The interfacial tension of FVA 2 oil was estimated: $\text{IFT} = 30.01 \text{ mN}\cdot\text{m}^{-1}$. Each measurement (CA and IFT) was performed at least six times in the similar conditions in order to obtain statistical results. It is important to note that the water and oil measurements were performed on the same samples (i.e. exactly the same topography) after complete cleaning of the samples. In order to study the effects of the structure orientation, the contact angles were measured parallel and perpendicular to the line patterns as it is represented on the figure 38.

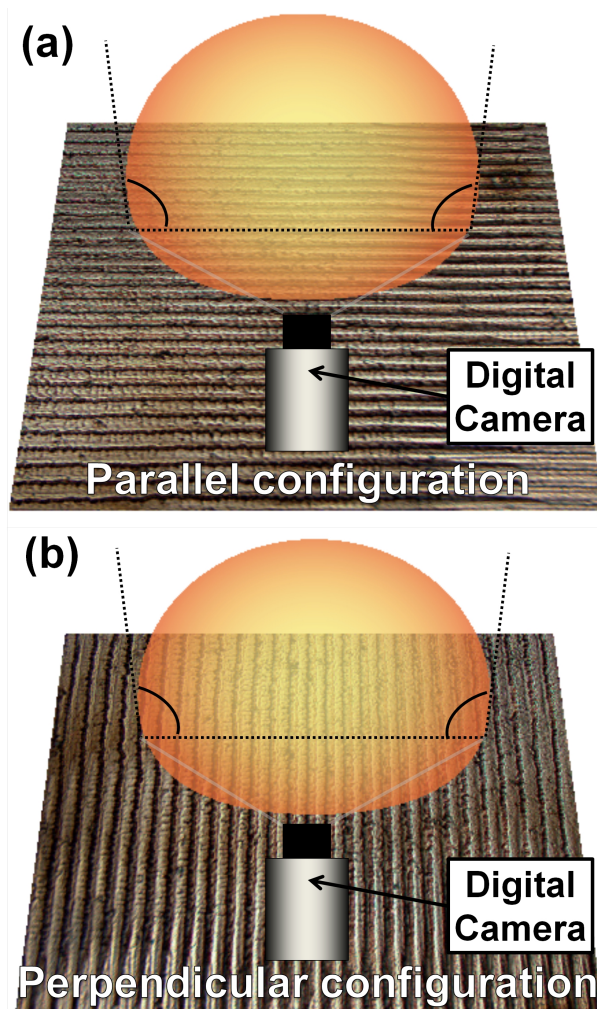


Figure 38: Schematic representation of the contact angle measurement in the case of the perpendicular (a) and parallel (b) structure orientation [102].

4 Femtosecond laser structures

4.1 Results

4.1.1 Topographical analyses

The topography of all the structures created using femtosecond laser surface texturing are reported in the present section and were analyzed by white light interferometry and scanning electron microscopy.

A cavity-profile comparison of the different structures are represented in figure 39. By increasing the number of pulses, the depth and the profile of the hole drastically change. Depending on the number of pulses, two types of laser profiles could be identified. For holes with 9 and 20 pulses the profile is homogeneous, while for a higher number of pulses, the topographical profile is divided into two distinct zones. The center consists of very steep peaks and valleys, with a very strong gradient in the transition to the flatter surrounding ring. The maximum depth is reached in the center, but only a weak percentage of the initial diameter is located at this depth: 28.4 % and 30.8 % for 5 μm and 10 μm depth, respectively. From the WLI data,

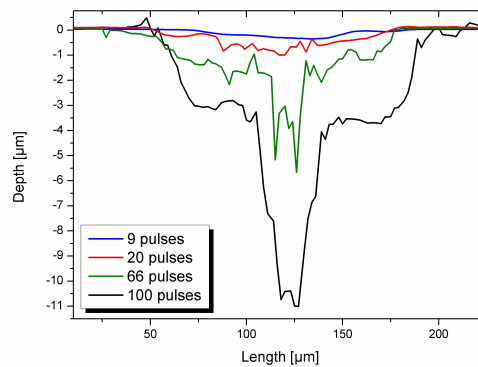


Figure 39: Profiles of the different laser cavities. For 9 and 20 pulses, the averaged maximal depths are respectively 0.4 and 1 μm . For higher pulse counts (66 and 100 pulses), the profiles are more irregular and two distinct zones can be recognized [103].

Abbott-Firestone curves (AFC) were acquired [104]. Bearing ratios simulate the effects of wear and the ability of a structure to carry a load assuming that a surface with irregular asperities in height will be more exposed to wear and

friction. The AFC plotted in figure 40 show that the ability of the structure to resist wear, decreased when increasing the number of pulses. The flatness of the AFC indicates that the surface area ($1410 \mu\text{m} \times 1060\mu\text{m}$) used for the estimation is regular for all the number of pulses. This simulation takes into account the air to material ratio by considering the highest peak and the lowest valley heights of the topography. For this reason, the estimated depths of the AFC are higher than the values of the maximal depths calculated from the depth profile shown in figure 39. As demonstrated in table 5, the cavity depth and the potential volume of retained lubricant (V_2) estimated by WLI increase with the number of pulses. Moreover, the core roughness depth (R_k) varied with the number of pulses and showed a minimum value of $53.3 \pm 1.8 \text{ nm}$ for 20 pulses. Laser cavities of the four different configurations have

Pulse count/ Max. depth	R_q [nm]	R_q-err [nm]	R_k [nm]	R_k-err [nm]	V_2 [$10^4 \mu\text{m}^3$]	V_2-err [$10^4 \mu\text{m}^3$]
Unstructured	23.5	0.4	53.9	1.4	1.9	0.1
9/0.4	99.8	1.0	72.2	5.2	13.7	0.5
20/1	179.3	5.6	53.3	1.8	24.5	11.1
66/5	886.4	6.9	73	4.2	114	0.8
100/10	1289.7	12.1	241.5	12.2	283	3.4

Table 5: Core roughness depths (R_k) and potential volumes of retained lubricant (V_2) determined using WLI. V_2 values increase with the number of pulse. The minimum of R_k is found for samples structured with 20 pulses ($1 \mu\text{m}$ depth) [103].

been characterized using SEM (figure 41). As the number of pulses increases, the surface morphology evolves as it is clearly visible on the work of Chichkov *et al.* [22]. In figure 41 (a) (9 pulses) and (b) (20 pulses), two different zones can be identified: the ablated zone in the middle of the laser cavity and the ring of ripples situated all around the ablated area. These zones were observed in all of the irradiated samples, independent of the number of pulses. Different distributions and sizes of the ripples were observed as shown in figure 41. According to the literature, their orientation is perpendicular to the laser polarization (figure 41) which in the present case is p [29, 37]. The transition between the ablated area and the ripples cannot be clearly defined. A third zone outside of the laser spot becomes visible at 20 pulses (figure 41 (b)) and can be clearly observed at 100 pulses (figure 41 (d)). At this point, a forth ring appears between the ablated zone and the ripples which presents no orientation. The ablated area is very rough and the material in this zone does not show any preferential orientation. The ablated zones (figure 42)

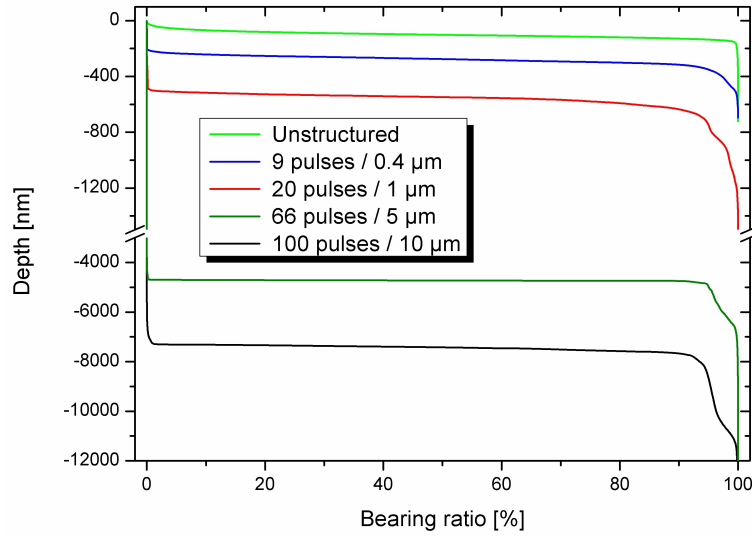


Figure 40: Abbott-Firestone curves of femtosecond laser structured 100cr6 samples. The samples irradiated with low number of pulses (9, 20 pulses) have a bearing behavior similar to the unstructured samples. For high number of pulses (66, 100 pulses), the bearing properties decrease [103].

of these samples correspond to the maximum depth presented in the WLI profiles (figure 39). Figure 43 shows the ripples corresponding to the samples irradiated with the previously mentioned pulses. The period of the ripples was estimated for these samples. The calculation of the periodicity was difficult for the low pulse count (9 pulses) due to the irregularities of the ripples (figure 43 a). For the highest pulse number, the formation of ripples was more regular but zones with different ripple morphologies were recognized as it is visible on the figure 41 (d). In the SEM picture 43 (d), two different morphologies can be clearly identified: the fine ripples at the border region (between irradiated and unstructured zones) have a period of about 355 nm while more in the center of the spot, the period increases until 555 nm. For all structured samples, the period varies approximately from 360 nm to 690 nm depending on the number of pulses used for the laser irradiation. In figure 44, the volume of each single laser cavity and the root mean square (R_q) values are plotted in function of the number of laser pulses. In the top left corner of figure 44, a 3D surface view (calculated with WLI) is represented. This square mask was used for the calculation of the previous values. In order to observe a clear evolution of these volumes, other spots were structured with pulse counts of 29, 40, 50, 80 and 90 leading to cavity depths of 3, 3.2, 4, 7 und 8.5 μm respectively. As the number of pulses increases, the ablated

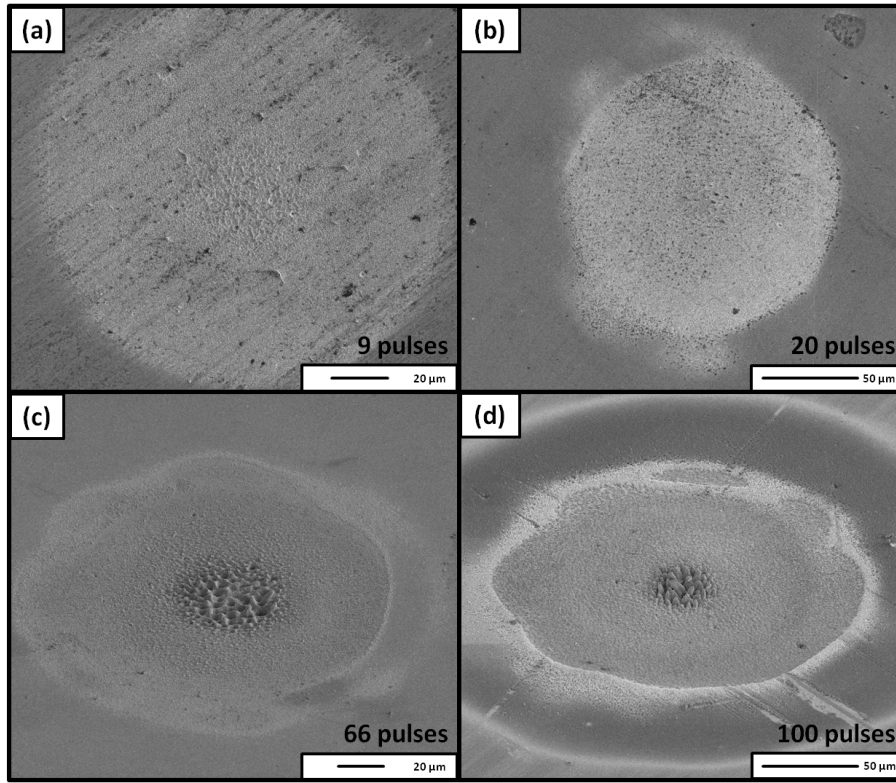


Figure 41: SEM images of the four different laser cavities depending on the number of pulses: (a) 9, (b) 20, (c) 66 and (d) 100 pulses. In each image, two zones can be clearly identified: the ripples and the ablated zone. In (c) and (d), four zones are visible: transition zones between the ablated zone and the ripples zone and between the ripples and the unstructured area [103].

volume (below the unstructured surface) increases parabolically ($R^2 = 0.963$) while R_q increases linearly ($R^2 = 0.975$).

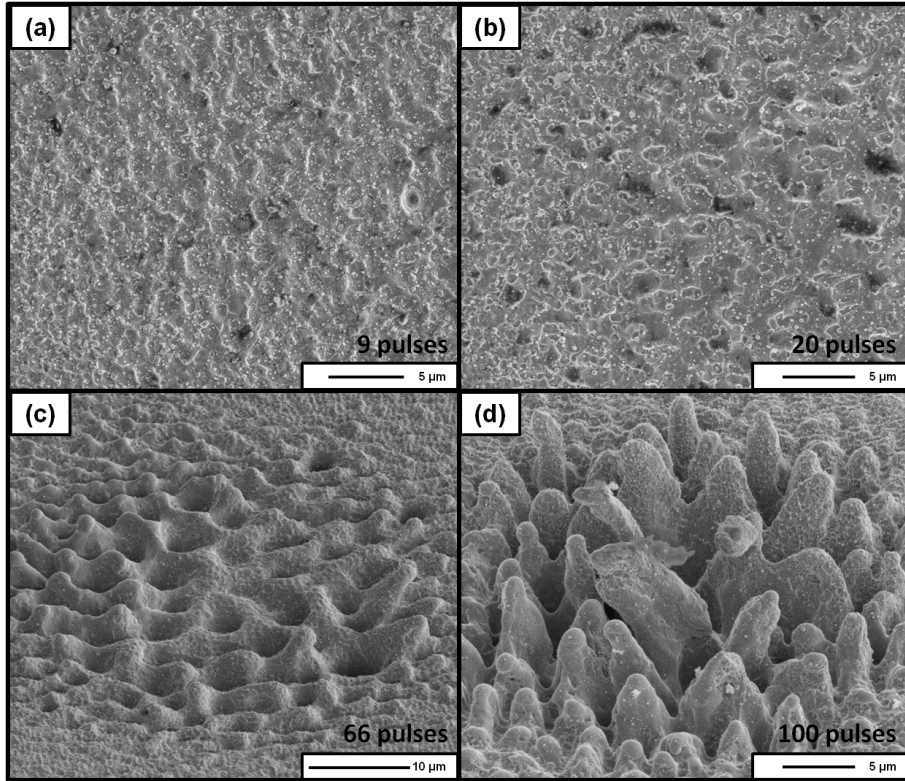


Figure 42: SEM images of the four ablated areas in the laser cavities depending on the number of pulses: (a) 9, (b) 20, (c) 66 and (d) 100 pulses. For a low number of pulses (9, 20 pulses) the ablated zone is almost flat, while for higher pulse counts (66, 100 pulses) it becomes rough and irregular. The ablated area is very rough and the material in this zone does not show any preferential orientation. The ablated areas of these samples show zones corresponding to the maximum depth represented in the WLI profiles (figure 39) [103].

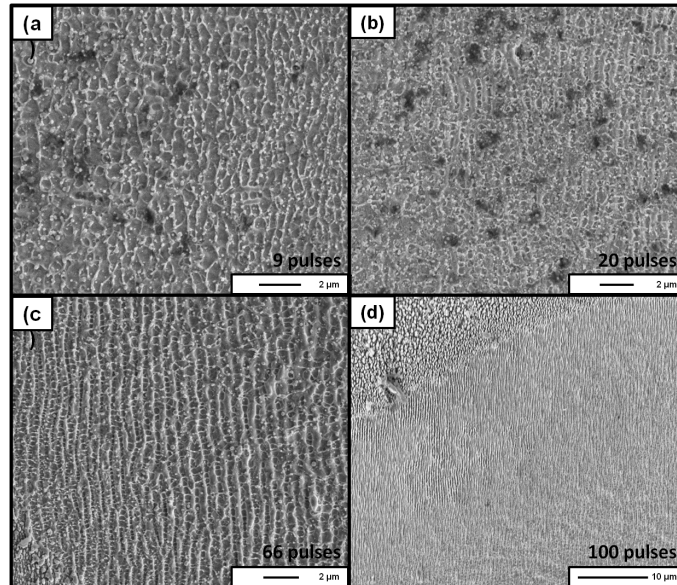


Figure 43: SEM images of the four ripple zones in the laser cavities depending on the number of pulses: (a) 9, (b) 20, (c) 66 and (d) 100 pulses. The period of the ripples was estimated and is in the sub-wavelength range, varying approximately from 360 nm to 690 nm [103].

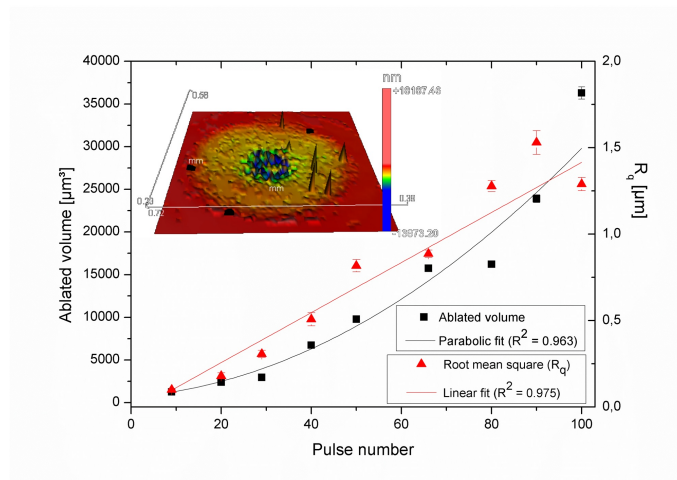


Figure 44: Ablated volume and root mean square values of the laser cavities (R_q) plotted as function of the laser pulse counts. A 3D representation of a WLI mask is shown in the left corner. Both ablated volume and roughness increase according to a parabolic ($R^2 = 0.963$) and linear ($R^2 = 0.975$) relationship, respectively [103].

4.1.2 Chemical analyses

In the present section, the attention is focused on the chemical composition of the surface of the metallic samples before and after femtosecond laser irradiation. The chemical composition of materials was studied using x-ray photoelectron (XPS) and Raman spectroscopy and atom probe tomography. In the following paragraphs, only the samples structured using femtosecond laser were studied. XPS analyses were performed on the irradiated and non-irradiated samples in order to study the chemical effects of the ultrafast laser ablation on the surface of 100Cr6. The density of irradiated spots (irradiated surface per total area) was increased to 50 % in order to collect sufficient information. Ion (Ar^+) etching was used to perform depth profile analyses in the sub-nm range and in order to get a reliable depth scale. The calibration of the etching rate was performed similar to the procedure described in the work of Müller *et al.* [98]. The information for oxygen, carbon and iron was determined by recording the signals of the O-1s, C-1s and Fe-2p core levels, respectively.

Figure 45 shows the evolution of these signals as a function of the etched depth, starting with the adventitious layer (surface), which typically contains O-H, C-H and C-O groups.

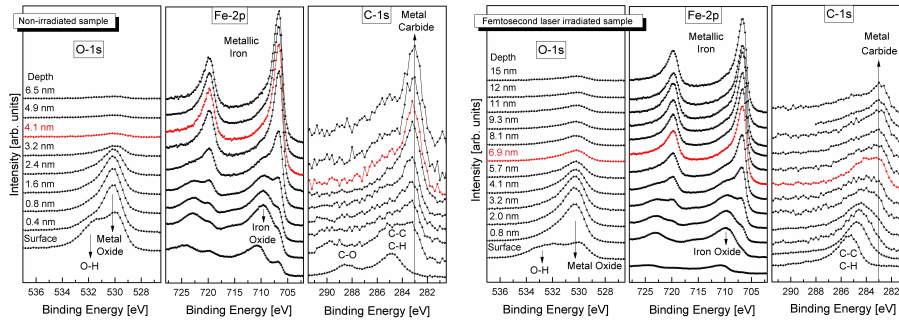


Figure 45: XPS signals of oxygen (O1-S), iron (Fe-2p) and carbon (C1-S) of the (left) non-irradiated and (right) femtosecond laser-irradiated samples. The thickness of the surface layer containing iron oxide is defined by the depth at which the oxide satellite contribution vanishes (red line) [103].

Since the presence of iron in oxide or metallic states is not necessarily correlated to the amount of detected oxygen, the characteristic satellite structure in the Fe-2p spectra (~ 710 eV) was used as an experimental fingerprint for oxide formation [105]. The thickness of the surface layer containing iron oxide is defined by the depth at which the oxide satellite contribution vanishes. Thus, the iron-oxide layer was estimated to disappear at 4.1 nm

and 6.9 nm depths in the non-irradiated and laser-irradiated samples, respectively (red line in figure 45). Moreover, while at 6.5 nm the oxygen 1s peak (~ 530 eV) almost disappears in the non-irradiated sample, it is still present in the irradiated sample at 15 nm [106]. This suggests two possibilities between 6.9 nm and 15 nm: traces of oxide that cannot be separated as Fe-2p satellites or that may result from chromium may be present or oxygen species (e.g. from adsorbates) were created on the surface of the 100Cr6 due to the ablation process. Moreover, since the C-1s peak starts to shift to lower binding energies around 283 eV [107] it is evident that carbon forms a metal carbide in the bulk of the steel matrix. This evidence indicates a chemical modification of the carbon bonds in function of the depth due to the ablation process. The carbon atoms experience an average charge distribution from the surrounding atoms, which produces chemical shifts in the binding energies [108]. Confocal Raman spectroscopy was performed in order to obtain information of the elemental composition on the modified surfaces. The vibrational spectra from treated and non-treated zones were acquired for samples irradiated with 9, 20 and 66 pulses. Figure 46 shows raw Raman spectra of the unstructured and ablated zones, and the ripples measured on the sample with 20 pulses using a magnification of 50 x. Iron oxide and chromium oxide bands were observed irrespective of the location due to the composition of the 100Cr6 steel, in the $200 - 700 \text{ cm}^{-1}$ range and around 1320 cm^{-1} [109], and in the $900 - 1100 \text{ cm}^{-1}$ range [110–115], respectively. The Raman intensities of these bands are more than one order of magnitude higher in the structured than in the unstructured zones, indicating an abundance of these compounds after the ablation process. Moreover, the carbon D (disorder), sp² and G (graphite) bands were only observed in the ripple and ablated zones at around 1350 , 1500 and 1600 cm^{-1} , respectively. Similar values of the D and G bands have been observed [116–118] in amorphous carbon spectra. Normalized Raman spectra of the ripple and ablated zones are compared for the different samples in figure 47. In the ripple zone, similar spectra within the 9, 20 and 66 pulse samples are observed, whereas in the ablated zone of the latter the fluorescence signal increases as well as the size of conical spikes. In order to study the crystallinity of the carbon observed in the structured zones, Raman mapping was performed using an optical magnification of 100 x from the center to the border of the circle. For each spectrum, a non-linear background subtraction and a Gaussian fit of all the observed peaks (figure 46) were performed. Figure 48 shows the amplitude of the D and G bands of the carbon in the Raman signals as a function of the radial distance measured on the sample with 20 pulses. The ratio of the amplitude of these two bands (I_D/I_G) is usually used to state the degree of order of the detected carbon [112, 119–122]. Thus, if $I_D > I_G$ then the car-

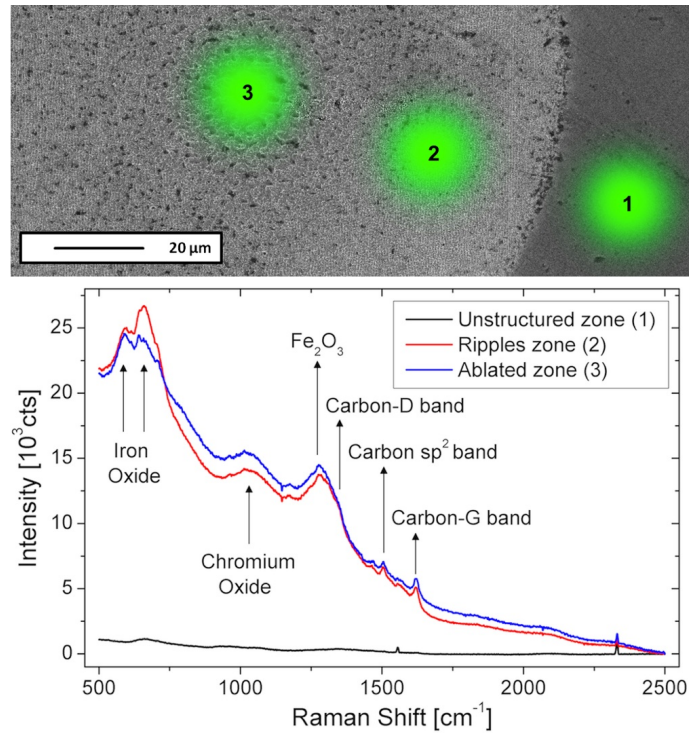


Figure 46: Raw confocal Raman spectra of the unstructured (1), ripples (2) and ablated (3) zone measured on the 20 pulses sample, using an optical magnification of 50 (spot size shown in green). Iron and chromium oxides were observed in all the zones, whereas the carbon D, G and sp² bands were observed in the modified zones [103].

bon is predominantly in the amorphous state, which is otherwise crystalline ($I_D < I_G$). As shown in the plot of figure 48, I_D is always higher than I_G , which indicates the presence of amorphous carbon in all the structured areas. Nevertheless, the global tendency shows an increase of the crystallinity of the carbon towards the center of the structured zone.

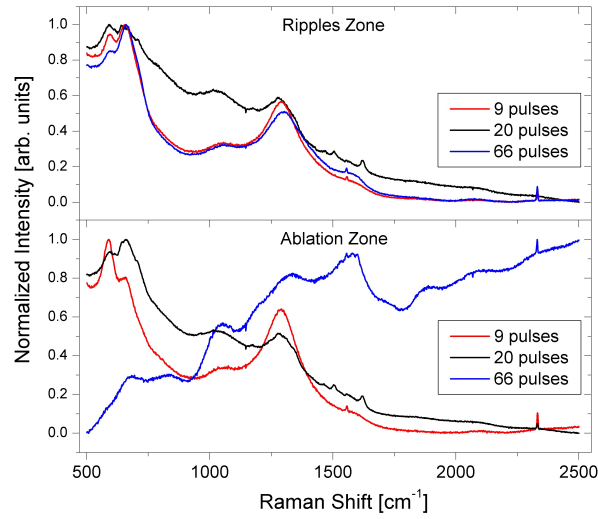


Figure 47: Normalized Raman spectra measured on the (top) ripples and (bottom) ablated zones of the samples structured with 9, 20 and 66 pulses, using an optical magnification of 50. The ripples zones showed similar spectrum, while the ablated zone showed higher fluorescence signal for higher number of pulses [103].

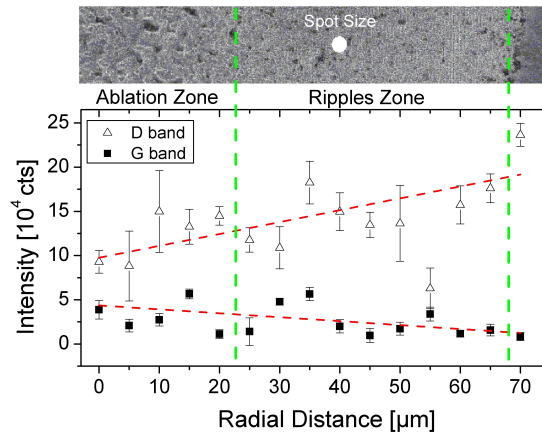


Figure 48: Fitted amplitude of the Raman peaks corresponding to the carbon D and G bands measured on the 20 pulses sample using an optical magnification of 100 which corresponds to about $1 \mu m$ information depth. The global tendency shows an increase of the crystallinity of the carbon towards the center of the structured zone [103].

Atom probe tomography (APT) was performed on the three zones: non-irradiated, ripple and ablation areas. APT data are shown in the present section as 3D reconstructions created from the recorded sequence of field-evaporated ions hitting a position-sensitive delay-line detector [123]. The reconstructions shown here represent the evaporated volume of the ions below the Ni cap. In this study, the attention was focused on the iron oxides (FeO and Fe_2O) and the decomposed carbon.

The APT analyses of the data were carried out exactly after the Ni layer. The Ni ions from the capping layer were evaporated first in each specimen. Figures 49 and 50 show the applied DC standing voltage as a function of the number of ions (depth) collected from a ripple zone specimen, and the mass spectrum obtained from the ablation zone, respectively. No significant difference from the curves presented in these figures was observed within the analyzed zones.

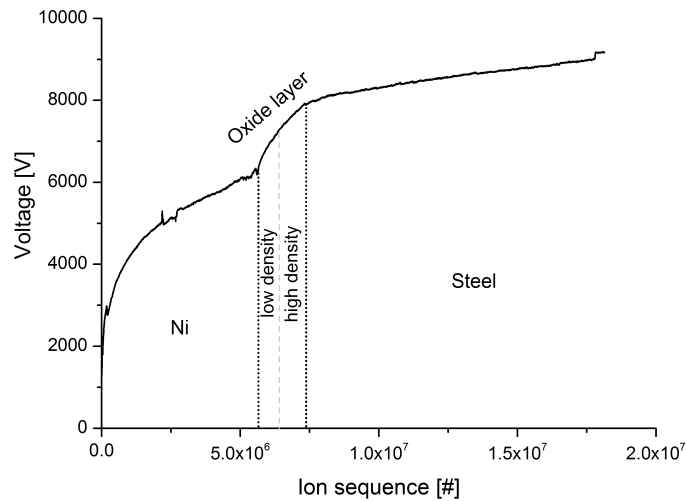


Figure 49: Applied DC standing voltage vs number of ions (depth) collected from a ripple zone specimen. The oxide region is marked between the black dotted lines. The low and high density regions of the oxide are indicated and separated by the grey dashed line.

Several iron molecular species were detected on the mass spectrum from the oxide layer (FeO , Fe_2O , Fe_2O_3 , FeO_2). For decomposition of concentrations the background level was removed using the built-in routine in IVAS software. The most oxide species were detected from the ablation zone (see figure 50) due to the large oxide layer. Oxygen concentration values in oxides are generally difficult to analyse, which is a common issue in the APT community [124, 125]. The possibility of the peak at 16 amu to be an O_2^{++}

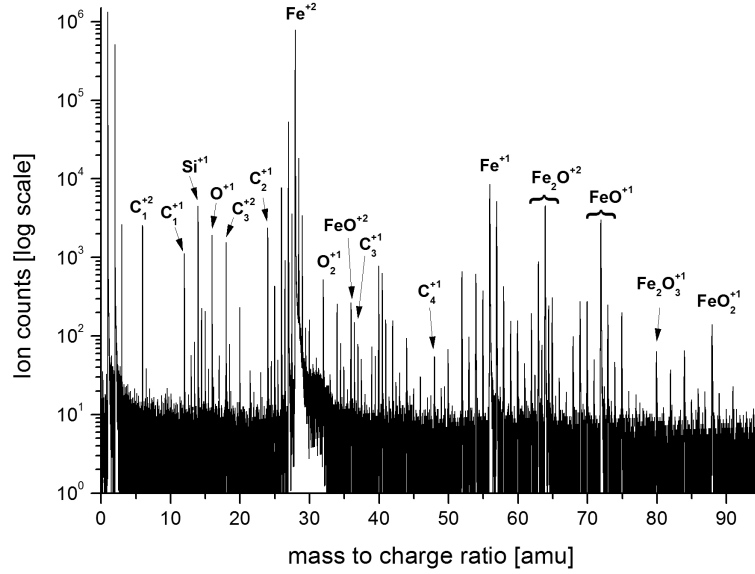


Figure 50: Laser assisted mass spectra of 100Cr6 sample extracted from the ablation zone.

or O^+ is a matter of debate for example [124–128], which would strongly affect the calculated stoichiometry. Moreover, oxygen has a high probability to evaporate as a multiple event which leads to lower concentrations of oxygen detected than actual value [129, 130].

The investigations on multiple events have shown relatively higher peaks of oxygen compared to other elements in the mass spectrum. Oxygen at 16 amu was assumed here to be O^+ and at 32 amu as O_2^+ . The value from these two peaks was added to the proper weightage from all iron oxide molecular constituents. This lead to a decomposed concentration value of $72.22 \pm 0.3\%$ Fe - $27.78 \pm 0.8\%$ O, which slightly shows less oxygen enriched than Fe_2O_3 . Oxygen forming complex ions with other elements during evaporation was not included in this calculation (such as: CO, CO_2 , HO, H_2O , and CrO). Moreover, the natural isotopic ratio of oxygen 18 (0.2 %) was not taken into account since it is less than the background noise due to hydroxide ion evaporation. For these reasons, it could be understood that oxygen would have a slightly lower measured value in the oxides.

Several complex ion evaporations were detected in the measurements, most likely due to the high laser intensities used [131]. C has showed several molecular ions, such as, C_2^+ , C_3^{++} , C_3^+ , and C_4^+ . Similar to O evaporation, adjacent C atoms also have a high tendency to field-evaporate during the same pulse leading to higher multiple events. Multiple events for all the

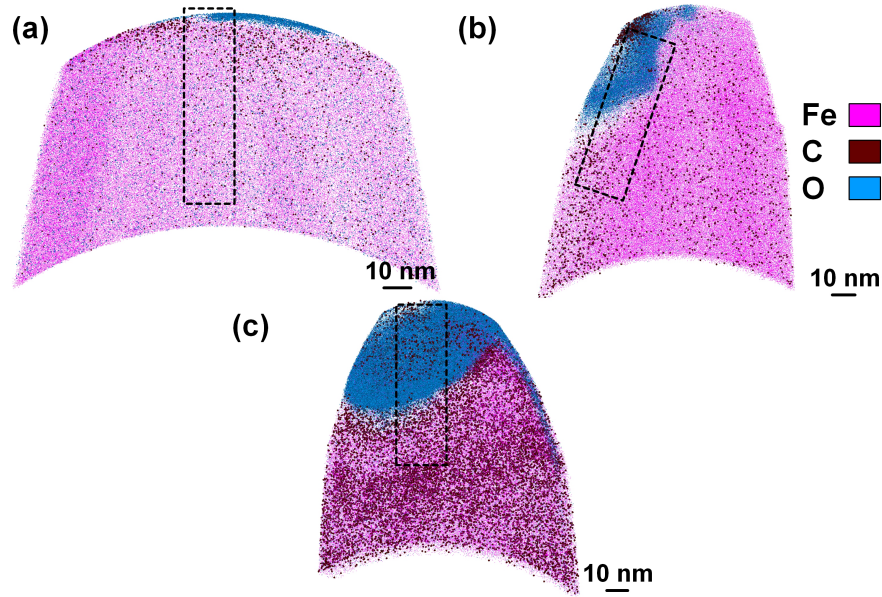


Figure 51: APT reconstructions performed in the (a) non-irradiated, (b) ripple and (c) ablation zones. The three slices are 50 nm thick. The concentrations of O and C increase from the non-irradiated to the ablation zone.

Concentration [at.%]	Non-irradiated	Ripple	Ablation
C (decomposed)	0.044	0.091	1.67
O (decomposed)	0.179	1.264	3.137
Total number of ions	$26.6 \cdot 10^6$	$21.5 \cdot 10^6$	$25.1 \cdot 10^6$

Table 6: Concentrations of decomposed C and O species and total number of ions in the three different zones. The atomic error is 0.001 at.% for all the values.

C molecular ions were almost twice as much as single events. It is also believed that the occurrence of molecular ions is dependent on the temperature increase in the sample (thermal pulsing) [132]. Therefore, the decomposed C values calculated represent a rough estimation of the actual C value in the specimen (C values from complex ions were decomposed based on the natural abundance of isotopes [133]). Table 6 shows the decomposed O and C values for each of the three sample conditions measured. A significant increase for O and C concentrations is shown for the ablation zone, probably due to the higher laser irradiation.

For each of the three zones, an iron oxide layer was found on the bulk steel. As observed in the former work [103], the oxide layer thicknesses varied for

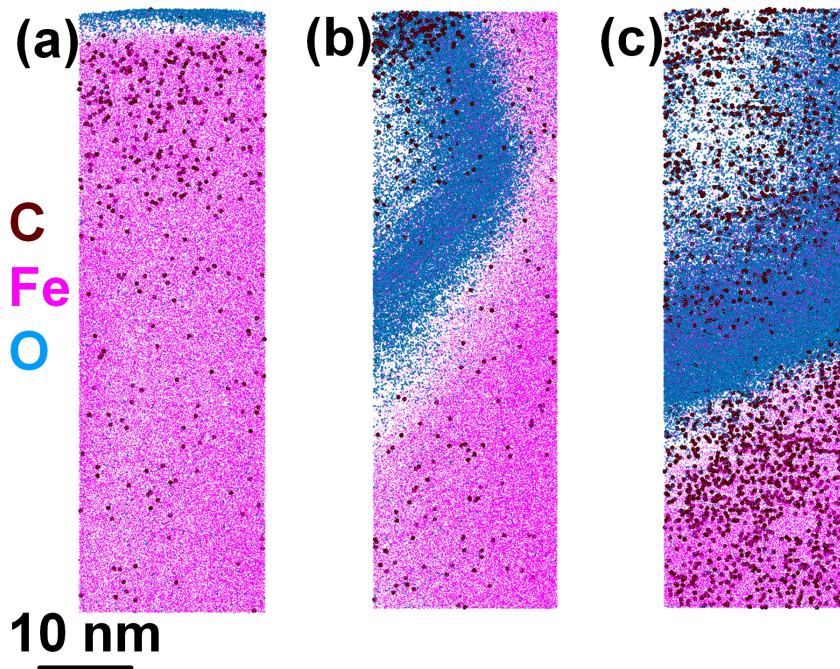


Figure 52: Region of interest (ROI) taken from the (a) non-irradiated, (b) ripple and (c) ablation zones. The concentrations of O and C atoms clearly increase with the laser intensity.

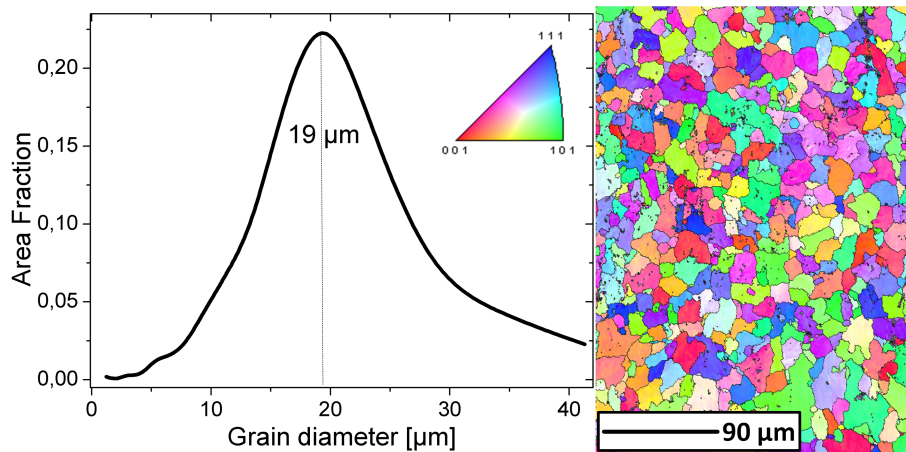


Figure 53: Grain size distribution and inverse pole figure map obtained through EBSD at the surface of the non-irradiated sample. No preferential orientation is observed, and the average grain diameter is around 19 μm .

each zone (figures 51 and 52). For the non-irradiated specimens, a very thin

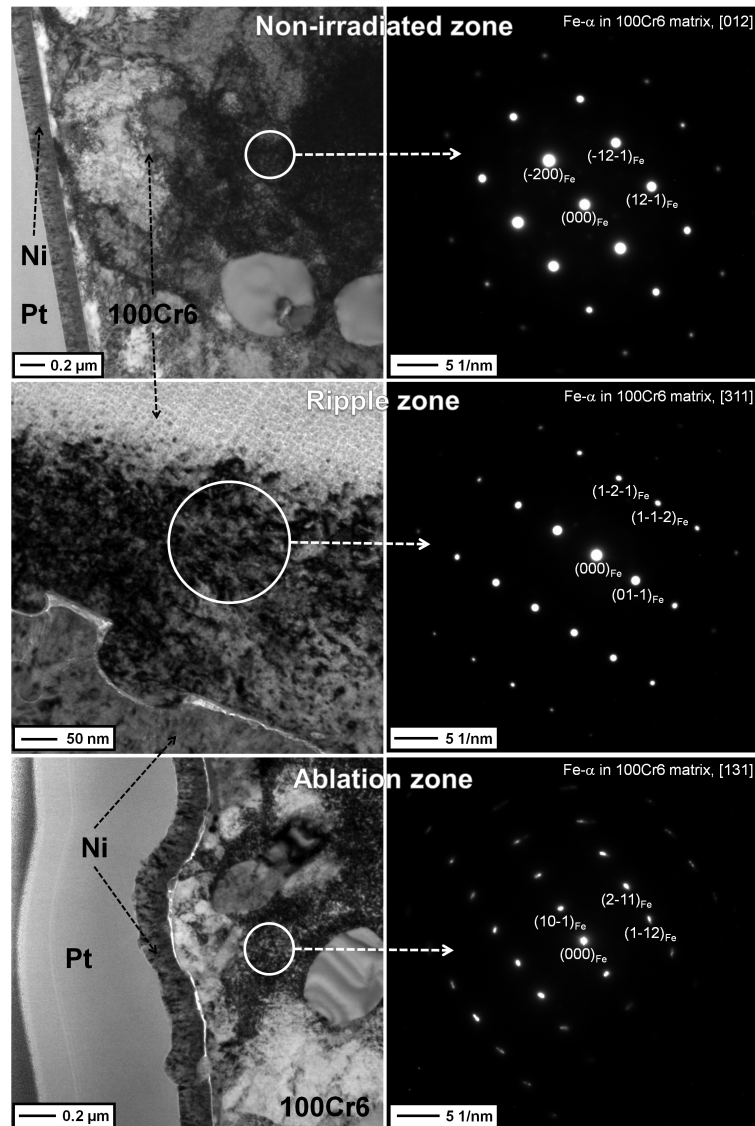


Figure 54: TEM micrographs and corresponding selecting area diffraction (SAD) patterns of BCC iron in the 100Cr6 steel bulk of the three zones presented in the figure 41. Only in the ablation zone, near the surface, the shape of diffraction spots are lengthened.

layer of oxides was detected (~ 3 nm), while the ripple and ablation zones have shown thicker layers (22 - 34 nm). In the ripple zone, the oxide layer was asymmetrically distributed in the specimen. This asymmetry is probably due to the roughness of the ripple zone (as observed in the figure 41) which reaches a depth of about 100 nm depending on the working conditions [134]. However,

the oxide layer density in the reconstructions was inhomogeneous. They have showed low to high-density regions from top to bottom, respectively. This most likely has happened due to slight retention of the oxides (low density part) on the surface of the tip during evaporation, leading to a reconstruction artefact. The data was reconstructed using the standard algorithm developed by Bas *et al.* [135] which assumes a constant field evaporation sequence from the tips. In the case of high evaporation-field species, low density zones appear in the reconstructions as an introduced artefact. Metallic oxides require slightly higher electric field to evaporate as compared to bulk metal atoms [136], which in the present case is observed for iron oxide as compared to Ni (figure 49). As the standing voltage increases and approaches the required field for evaporation the oxides start evaporating at a slightly higher rate (higher density part).

A region of interest (ROI) was extracted from each 3D reconstruction (figure 51) to show the distribution of C, O, and Fe atoms. It can be seen that the concentrations of O and C atoms increase with the laser intensity, which is consistent with the former observations [103]. The 1D concentration profiles of C (decomposed) and O were calculated from the ROI shown in the figure 52 and plotted in figure 55. Fixed counts (4000 ions) per sampling step were used in calculating the profiles in order to reduce statistical errors due to the ion density variation. For the non-irradiated zone, the O concentrations are very low (< 0.05 at.%) and most of the C species detected were concentrated near the surface with almost 0.5 at.%. The ripple zone shows a slight variation in the C content, whereas the O value in the oxide was almost 3.5 at. %. Apart from the oxide region, the bulk has the same solute concentrations as for the non-irradiated zone. The oxide layer in the ablation zone was thicker than in the ripple zone but had almost the same O content. However, the C concentration in the ablation zone was uniquely different. High C content was estimated to reach values of almost 4.2 at.% in the oxide layers and in the steel bulk. The distribution of C is inhomogeneous, which likely reflects the influence of the high laser irradiation in these regions. The total concentrations of the species were calculated in each APT specimen and are summarized in table 6. The microstructure of the non-irradiated zone was analyzed using EBSD. The ripple and ablation zones presented rough surfaces that were not suitable for EBSD analysis. The measurements are presented in figure 53 and were performed with the normal to the sample surface pointing towards the CCD camera. The analysis did not reveal any preferential crystallographic orientation and the grain size distribution was Gaussian, with an average diameter of approximately $19 \mu\text{m}$ (figure 53). The TEM micrographs presented in the figure 54 show the microstructure

of the bulk of 100Cr6 steel in the non-irradiated, ripple and ablation zones. Diffraction measurements were performed below the surface in each area and the corresponding selected area diffraction (SAD) patterns are shown. In order to obtain a reference diffraction pattern, the measurement in the non-irradiated zone was performed deep in the bulk of the 100Cr6 matrix. The indexing analysis showed a α -Fe pattern with a [012] zone axis and 0.286 nm of lattice parameter. The SAD patterns allowed to recognize the bcc pattern of the α -Fe as the non-irradiated state. In the ripple zone, the measurements were performed closer to the surface of the lamella, which showed a α -Fe pattern with a [311] zone axis. In the ablation zone, diffraction measurements were performed at the surface as the former case and below the surface at around 500 nm depth. Contrary to the patterns observed in the former zones, the measurements on the ablation zone show a diffraction pattern with lengthened spots (figure 54) because in this area, a high density of dislocations was observed, which means that the plans are strongly deformed. The indexing analysis showed the α -Fe phase with a [131] zone axis, and no grain refinement could be observed.

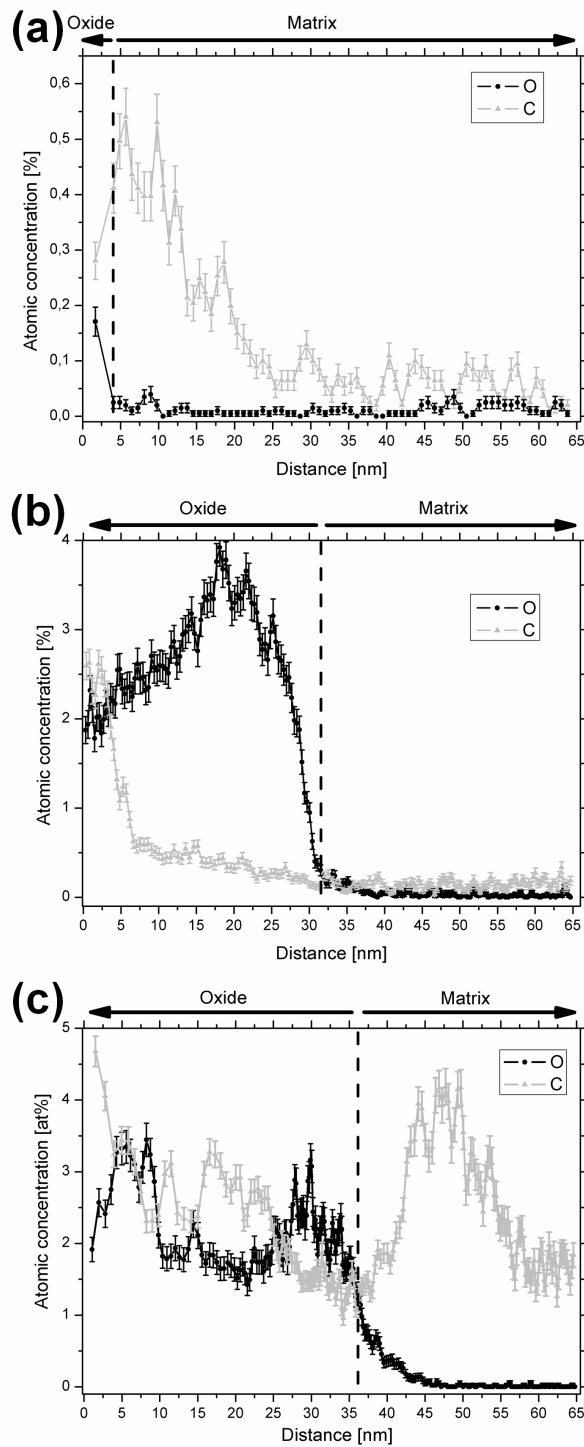


Figure 55: O and C 1D concentration profiles in the ROI in (a) non-irradiated, (b) ripple and (c) ablation zones shown in figures 51 and 52. The amounts of C and O significantly increase after the laser irradiation.

4.1.3 Wetting properties

In this section, the wetting behaviour of surfaces irradiated by means of femtosecond laser is studied in order to determine how the pattern design can influence the wettability of the metallic surface. CA measurements were performed on the surface of the femtosecond laser irradiated samples. The effects of two different geometrical parameters (maximal depth of the cavity and period between the holes) were studied using the FVA 2 oil as fluid. The effects of the diameter were not studied and it was kept constant ($\sim 110 \mu\text{m}$) for all the results presented in this section. In order to observe the influence of the laser structures, the CA of a non-irradiated surface was measured about $13.6^\circ \pm 0.4$, 6 seconds after the drop deposition. In figures 56 and 57, the entire contact angle evolution is shown from the starting point of the measurement (0 s: droplet deposition onto the surface) until the most stabilized CA value measured (6 s after droplet deposition). In the figure 56, the effect of the maximal depth of the laser cavity is studied with three different configurations 1, 3 and 5 μm . First of all, the final CA values of all the patterned surfaces have an average value lower than the unstructured configuration proving the effects of the laser patterning to increase the wetting of a metallic surface. The curves show that the 5 μm configuration has provided the highest contact angles during the complete measurement. At the deposition time ($t = 0 \text{ s}$), it is clear that as the structure becomes deeper, the CA increases during the initial phase until the stabilization (starting at $t = 2 \text{ s}$). The 3 μm configuration induces the smallest CA after 6 s by 10.8° . Finally, the 1 μm depth configuration provides a medium CA of 11.7° and the most stabilized wetting behaviour as it shows the smallest error bar in comparison with the two other structures.

The period of the femtosecond laser patterns was changed in order to obtain three different configurations and their influences on the wetting behaviour are shown on figure 57. It was decided to keep the diameter and the depth of the cavities constant regarding the previous results (figure 56) and for reasons, which will be further detailed in the *Discussion* part. Then, the depth was chosen to be 1 μm for these patterns. The distance between the laser cavities is defined as "period" of the structure. Then, since the period varies, the structure density (ratio of the laser irradiated area on a global area) changes as well. Three distances were chosen to study their influence: 250, 500 and 1000 μm leading to structure densities of 7.3, 2.5 and 0.8 %, respectively. The choice of these distances i.e. these densities is related to the previous geometrical parameters (diameter and depth) and thus to the laser texturing process itself and the cost and use of the

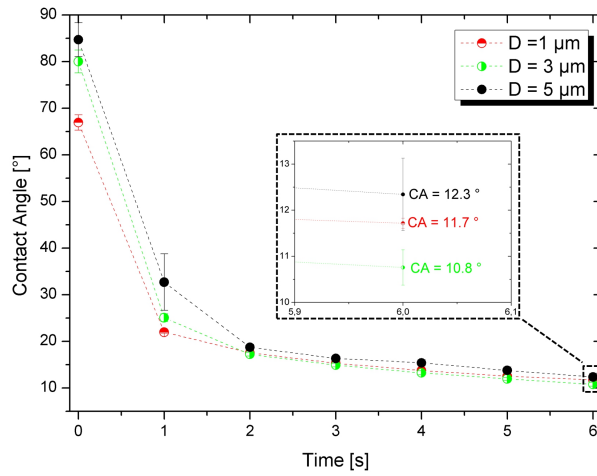


Figure 56: Time evolution of the contact angle using FVA 2 oil as a function of the depth of the femtosecond patterns. The inset clearly shows the effects of the depth. The diameter and period of the cavities were kept constant (110 and 500 μm , respectively).

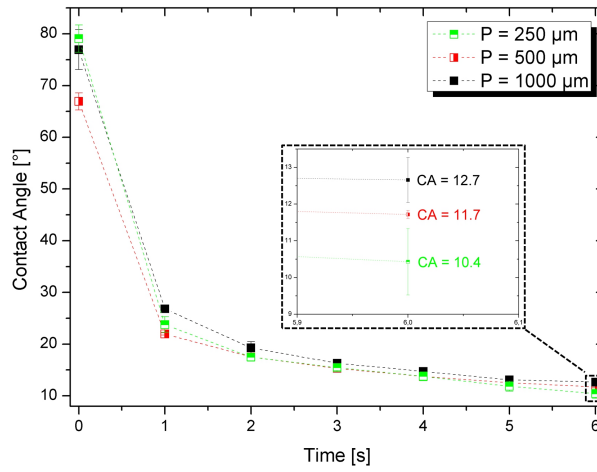


Figure 57: Time evolution of the contact angle using FVA 2 oil as a function of the period between the femtosecond patterns. The inset clearly shows that as the distance between the cavities increases, the contact angle increases too. The diameter and depth of the structures were kept constant (110 and 1 μm , respectively.)

femtosecond laser. These considerations will be discussed in the *Discussion* part. In the present curves, the CA provided after the wetting of the laser patterned surfaces are, as previously, lower than for the non-irradiated

surface. Nevertheless, the CA evolution varies until 4 s after the drop deposition, and then a tendency appears showing that the CA decreases with the shrinking distance between cavities. The lowest error bar after 6 s appears, as in the case of the depth study, for the 500 μm distance and 1 μm depth.

4.2 Discussion

4.2.1 Topographical analyses

In the present work, it was observed that the femtosecond-laser cavity profiles drastically change by increasing the number of pulses. The depth profiles observed with low pulse counts are less steep compared to the ones with high pulse counts. This fact suggests that a lubricant might homogeneously and more efficiently wet the surface of the shallow laser structures because it would require less energy to spread and would not be trapped in the deep cavities of the ablated zone. Thus, the estimated volume of retained lubricant would be lower than the volume of the laser cavity due to the sharp cone-like structures, which strongly grow with the pulse count. Each successive pulse enhances the roughness of the irradiated area and modifies the absorption of the laser energy. This agrees with the evidence reported by Stern [137], since the increase of the roughness leads to an increase of the laser absorption due to multiple reflexions of the light in the surface microcavities [138]. Further studies should be performed in order to explore the different distributions and sizes of the ripples observed in the irradiated samples. According to the measured Abbott-Firestone curves and R_k values, the sample irradiated with 20 pulses (1 μm depth) is considered as the best configuration for load bearing due to the formation of regular cavities and the absence of sharp holes and disoriented asperities, as shown by the WLI analysis and SEM pictures. Homogeneous cavities are better for load bearing than heterogeneous because the load will be more homogeneously distributed on the surface. This claim is in agreement with similar studies performed on metallic [139] and silicon substrates [37, 140]. For a low number of pulses, the morphology only presented nanoscale roughness, while for a high number of pulses, a higher roughness was observed. The last two works stated that the formation of spikes is due to the ablation phenomenon, and Her *et al.* correlated the formation of cones with the random presence of protective elements (sputtering-resistant impurities), which prevent a uniform ablation of the material. In the present work it is suggested that the combination of the random distribution of impurities [37] and the change in laser absorption [38] might lead to the observed non-linear relation between the ablated volume and the number of pulses.

In the previous section, the oleophilic behaviour of the femtosecond laser irradiated surfaces was studied using the fluid FVA 2. The attention was focused on only two distinct geometrical parameters: the maximum depth and the period between the laser cavities. This study could be performed be-

cause it was chosen to keep the diameter of the laser holes constant ($110\ \mu\text{m}$). Nevertheless, this choice can be discussed, since smaller and bigger diameters could be created. Indeed, tests were performed to create 60 et $250\ \mu\text{m}$ diameter patterns, but it was almost impossible to obtain regular round-shaped structures. Seemingly the set-up limited the creation of small diameters because of a complex aperture and lens arrangement, which did not allow to create repeatable patterns. The $250\ \mu\text{m}$ diameter configuration was easier to set up but it finally lead to anisotropic patterns i.e. elongated circles. Indeed, the tunable-aperture allows the elaboration of such large patterns, but precision decreased due to the light dispersion. The choice of such diameters (60 , 110 and $250\ \mu\text{m}$) was previously established since it was important to obtain patterns with dimensions, which enable the period to have a significant influence on the wetting. Indeed, close diameters would not allow an interesting study of the period. Finally, it was chosen that the periodicity had to be almost twice greater than the lowest diameter in order to see an effect of both diameter and periodicity. The comparison of different maximum depths (1 , 3 and $5\ \mu\text{m}$) showed that the $5\ \mu\text{m}$ configuration provided the highest contact angle after $6\ \text{s}$ measurement. As shown before, this pattern configuration provides a very steep and sharp profile due to the cones' structures. For this reason, it is obviously more difficult to wet the entire cavity (from top surface to the bottom of the structure) in comparison to the 1 and $3\ \mu\text{m}$ depth profiles. Indeed, the droplet requires more time to overpass all these obstacles. The $3\ \mu\text{m}$ depth configuration provides the fastest spreading behaviour because its profile is less steep than the former $5\ \mu\text{m}$ but mostly because the profile does not show cone structure at all. The profile appears to be very regular and homogeneous. Finally, the intermediate behaviour of the $1\ \mu\text{m}$ configuration can be attributed to its tendency to be similar to a flat surface in comparison to the other configurations. The $1\ \mu\text{m}$ depth cavities act as *reservoir* in comparison to the flat and polished surfaces. Since the potential volume of lubricant is the smallest in this present case, the *reservoir* effect is limited in comparison to the $3\ \mu\text{m}$ configuration. Nevertheless, it is an advantage since it provides the smallest error-bar i.e. the most constant wetting behaviour. Deeper structures could be created in order to observe when the oleophilic behaviour could turn into an oleophobic behaviour and at which depth a Cassie-Baxter regime (i.e. composite interface) could be observe. This study has not been performed due to the motivation of this work which was to design structures which could be available for industrial applications. Then, since the time and costs requested and involved to create the $10\ \mu\text{m}$ depth patterns were already considerable to irradiate the samples, it was not worth trying it with higher pulse numbers. It might be better to use a different method such as embossing or milling techniques to design the

surface of the material while huge heating effects have to be considered in this case, since this kind of process affects the whole microstructure of the samples inducing residual stresses and preferential orientations etc.

By tuning the structure period and then the structure density, CA measurements showed an interesting effect which confirms partially the former statements. Indeed, as the period increases, the CA increases too confirming that a dense patterned surface with well designed cavities provides a faster spreading of the fluid on the surface. The *reservoir* role of the structures having a positive effect on the wetting behaviour is obvious yet. It proves that a dense structure (with optimized geometrical parameters) is not a succession of obstacles preventing a fast spreading of the liquid. This experiments showed that the fluid is trapped and its wetting is slowed down by the irregularities (cones and corresponding sharp asperities) present at the surface of the samples and the *reservoir* cavities are beneficial to spread the liquid.

4.2.2 Chemical analyses

The chemical analyses performed on the 100Cr6 samples showed that the femtosecond laser irradiation modified the composition of the surface. The XPS analysis revealed a growth of the iron-oxide layer thickness up to 6.9 nm, whereas other metal oxides might also be present even at 15 nm in depth. Moreover, a pronounced chemical gradient of carbide compounds was observed as a function of the ablation depth. The oxidation is based on thermal and non-thermal excitations of molecules at the surface [141]. In the present case, no thermal excitation is induced due to the ultrafast pulse time of the laser and the ablation process extracts the native oxide layer as well as the atoms below [142]. According to the works of Mott [143] and Cabrera [144], it is assumed that the O₂ molecules present under room conditions dissociate upon contact with the reactive surface, and the adsorbed oxygen ions lead to metallic oxidation. More detailed elemental analysis of the samples irradiated with femtosecond laser will be carried out using atom probe microscopy in further work.

The Raman analyses have confirmed the presence of iron and chromium oxides in the irradiated zones. Also, the main carbon-carbon bands (D and G) have been observed in the modified samples. The current research-interests focus on the different forms of carbon induced by the laser irradiation, mainly in view of the wetting properties of the surface that might be tailored by producing specific carbon species [145]. In this work, the presence of both amorphous and crystalline carbon was proved. Moreover, the degree of crys-

tallinity of the ablated carbon increases from the unstructured region towards the center of the irradiated zone. It is claimed that this fact, as well as the disordered carbon distributions are related to the Gaussian intensity profile of the laser beam. Thus, Fe atoms are removed and C atoms can easily recombine in the middle of the irradiated zones, while the formation of crystalline C at the edges is less probable due to the lower laser fluence. Considering that the binding energy of Fe-C is higher than that of Fe-Fe [146], a dissociation of the latter requires lower energy. Thus, increased ablation of Fe and agglomeration of C in its most stable configuration are expected. Moreover, the presence of cementite clusters in the steel matrix released from ferrite grains might also contribute to increase the proportion of carbon after the laser irradiation. For the samples irradiated with 66 pulses, the fluorescence of the signal highly increases, indicating the abundance of more amorphous (less crystalline) compounds in the ablation zone. This evidence agrees with the XRD results reported by Hirayama and Obara [23], which show that the sample is amorphized after the laser treatment. Moreover, it was assumed that this transformation is due to the melt-quenching phenomenon present in the ablation process.

By using the APT to analyze the effects of the femtosecond laser irradiation, the understanding of the wetting phenomena involved in the wettability of the samples is complete. The atomic resolution gives a detailed and complete chemical reconstruction of the atom arrangement at the surface of the samples. The presence of Fe_2O_3 in the non-irradiated zone can be due to the metallographic preparation, while for the irradiated zones it is most likely due to a recombination process generated by the ablation of Fe in the presence of O_2 [143, 144]. Indeed, the laser ablation creates reactive zones and the dioxide molecules recombine with atoms in these areas. Due to the Gaussian intensity profile of the laser beam, the ablation and recombination phenomena are concentrated in the full width at the half maximum (FWHM) region, leading to the most significant changes in topography and chemistry. Moreover, the 1D concentration profiles revealed that the C content at the surface of the irradiated samples significantly increases according to the laser intensity distribution. This also correlates with the crystallinity of the C found in these zones revealed by Raman spectroscopy [103]. These results confirm that the ablation of Fe atoms generates the recombination of C atoms in their most stabilized form and thus, the laser irradiation transforms the metal surface into a reactive area [147]. After the laser radiation, the roughness of the surface does not allow to obtain clear Kikuchi patterns in order to create the data. Thus, no relevant information was obtained in the irradiated zones. This deformation shows that the laser irradiation induces a

small lattice deformation in the steel bulk after fs laser ablation. Therefore, irradiation does not induce a grain refinement but rather deformations in the lattice. The dislocations introduce internal strains that locally deform the planes. As the quantity of dislocations is very important in each deformed grain, internal “sub-grains” appear in this region and thus change the shape of the diffraction spots. Similar SAD observations were realized by Shin *et al.* a low C steel after equal channel angular pressing (ECAP) [148]. While the mechanical process was different from laser irradiation, the microstructure analysis of their samples showed mechanical deformation of the steel and induced low-angled boundaries. Indeed, Hirayama and Obara observed that the fs laser irradiation on metallic samples (Au, Ag, Cu, Fe) partially changes the crystalline structure into amorphous in the ablated region avoiding recrystallization [23].

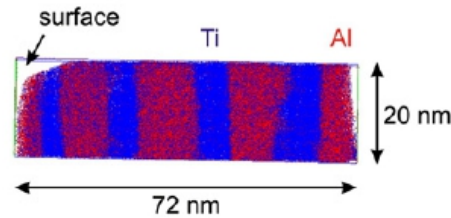


Figure 58: Results of the local chemical analysis in minimum zone positions obtained by Atom Probe Tomography [149]. The sandwich arrangement is clearly recognizable in the low energy zone allowing chemical composition measurements and a trustable statistical study.

Moreover, even if the concentrations of the species involved in the chemical wetting strongly varies with the laser intensity distribution, the first layer of each APT sample, which will be then in contact with the fluid, is made of oxygen, iron and carbon without depending on the laser distribution. This observation allows to affirm that the wetting of the 100Cr6 steel is not controlled by the surface chemistry but only by the topography. The APT gave crucial and novel informations regarding the effects of laser irradiation at an atomic scale but the present studies show its limitations, which are well known in the community. First of all, the time and cost requirements are huge in comparison to other methods of surface analysis such as Raman or XPS techniques. For this reason, a statistical study cannot be achieved as it would be the case by using Raman spectroscopy or topographical methods such as SEM or AFM. Furthermore, the 3D reconstructions shown in the results cannot be considered as representative results. As it was observed in the ripples zone, the geometrical distribution of the oxide and carbon clus-

ters is strongly asymmetric in comparison to the non-irradiated and ablation samples. The results were statistically verified by repeating the measurement three times per area, but the roughness has to be taken into account in this present case as this asymmetric repartition proves it. Secondly, the analysis of the 100Cr6 samples revealed that the initial composition of the steel could not be found in any of the three zones investigated and also not in the non-irradiated samples. The presences of oxygen and carbon enhanced by the metallographic preparation and the laser irradiation have also clearly influenced the chemical composition. Thus, it makes sense to remark that the APT technique might be more adapted to samples with predictable behaviours and simple composition ratio such as the titanium and aluminium multilayer thin films studied in the work of Detemple *et al.* [149]. In this case, the effects of the laser, or more generally the thermal treatment, are more easily evaluated and discussed. The samples were treated by means of the LIMET procedure, which lead to regular line patterns. APT and TEM micrographs showed that the chemical "sandwich" composition of the thin films was clearly measurable and found in the minimum energy zone. As it is obviously represented in figure 58, the sandwich composition of the Ti-Al samples allows more valuable and statistically relevant APT analyses.

4.3 Conclusions

The previous studies showed that the surface chemistry and the morphology of the samples drastically changed after the femtosecond laser irradiation. First, it was observed that the ablation process induces a significant change of the topography, if the experience was performed using low or high pulse numbers. Indeed, as the number of pulses increases, the maximal depth increases too but the shape and profile of the laser cavities significantly evolve. Most of all, the walls of the cavity become clearly steeper by high pulse numbers. Moreover, the ablation process induces randomly distributed spikes in the centre of the irradiated zone. Finally, the chemical composition of the first atomic layer at the surface of each zone is always made of C, O and Fe atoms independently of the laser intensity distribution. The contact angle measurements have first confirmed that the femtosecond laser irradiation has a beneficial effect to increase the spreading of the FVA 2 oil on the surface of the 100Cr6 steel. The choice of geometrical parameters such as depth and distance between cavities is of prior importance since it determines how fast the liquid will wet the surface. The cones resulting from the laser ablation play an important role in the wetting of the surface by the fluid, since they trap the liquid and then influence the wetting behaviour. Nevertheless, the diameter and period studies proved that the laser structures act obviously as *fluid-reservoir* which are beneficial to induce a fast and homogeneous wetting of the metallic surface.

5 Nanosecond laser structures

5.1 Results

The present chapter resumes the analyses performed on the samples irradiated using the nanosecond laser. Topographical and chemical studies were performed in order to investigate the influence of the LIMET process. Finally, the hydrophobic and oleophilic behaviours of the surfaces were investigated.

5.1.1 Topographical analyses

The topography of each sample was characterized using WLI and SEM. They were compared and can be divided into three groups: short (3.5 and 5 μm) averaged (7.5, 10 and 13 μm) and long periods (15.5 and 22 μm). A three-dimensional WLI picture presented in figure 59 shows the sample surface before the laser-patterning. It is worth to note that the metallographic preparation resulted in a flat surface with no preferential orientation, no significant topographic artefacts and around 50 nm root-mean-square roughness (R_q).

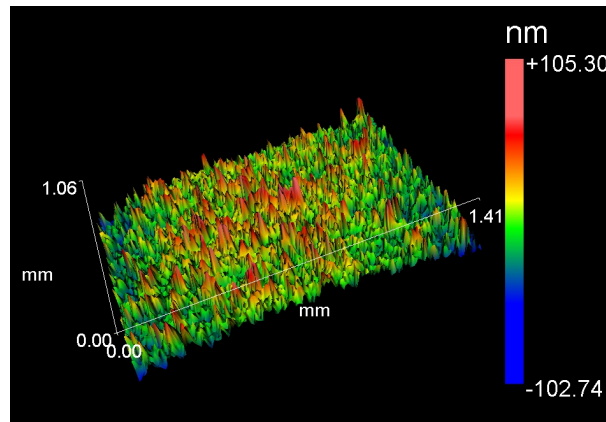


Figure 59: WLI picture of the grinded and polished steel surfaces prior to LIMET modification. The metallographic preparation resulted in a flat surface with a roughness of 50 nm (R_q) [102].

In order to study the effects of the pattern periodicity on the wetting behaviour, several patterns with seven different periodicities were fabricated with fluence about $2 \text{ J}\cdot\text{cm}^{-2}$. The irradiated area of each sample was approximately 1 cm^2 and composed of several adjacent spots of 3 mm^2 . The laser structured surfaces presented an averaged R_q value of around 580 nm.

Figures 60 and 61 show SEM images and depth profiles of the patterns produced on the flat surfaces after LIMET modification using 3.5, 13 and 22 μm of period, respectively.

The tallest topographic structures (peaks) of each sample were found to have similar height ($\sim 1 \mu\text{m}$) related to the lowest topographical regions (valleys) independent of the periodicity. The slope of the structures was calculated and corresponds to the distance from the highest point of the peak to the valleys divided by the corresponding horizontal distance. The periodicity and slopes of the different patterns are resumed in table 7. As shown in the SEM pictures and WLI depth profiles (figures 60 and 61), the pattern with 3.5 period is very regular in height and width. The peak pattern is rough and presents the highest slope. The 13 μm periodicity pattern shows irregular structures that present two distinct parts: a small and a big peak (figure [?] b). Their height and width vary along the line-patterns, and also present topographical “ramifications” or “bridges” between them. The 22 μm sample is homogeneous, with only one height peak induced by the laser irradiation, and the line structure provides the lowest slope of all the patterns (table 7).

Period [μm]	3.5	5	7.5	10	13	15.5	22
Slope	0.83	0.81	0.36	0.35	0.36	0.3	0.11

Table 7: Geometrical parameters of the LIMET structures used for the CA measurements. The height was kept constant around 1 μm for all the structured samples [102].

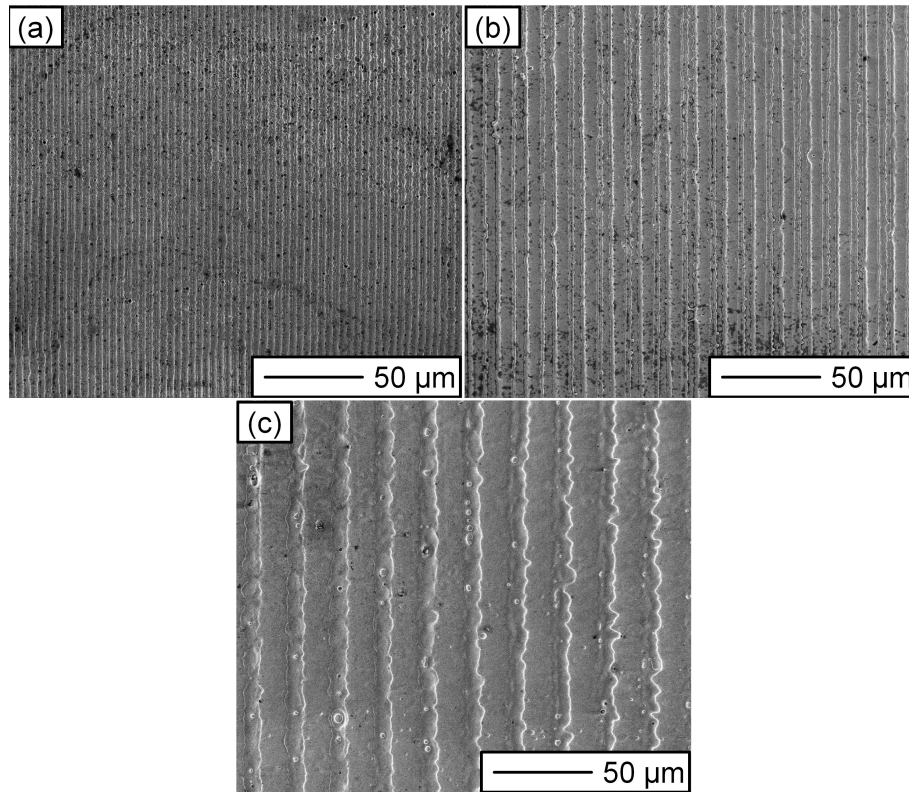


Figure 60: SEM pictures of the laser line patterns with 3.5 (a), 13 (b) and 22 μm (c) periods. The 3.5 and 22 μm structures are homogeneous compared to the 13 μm configuration which clearly shows irregularities due to the laser irradiation [102].

5.1.2 Chemical analyses

The surface of the samples irradiated by nanosecond laser was analyzed using x-ray photoelectron spectroscopy. In comparison to the femtosecond laser structuration, the LIMET method leads to a complete irradiation of the metallic surface. For this reason, the surfaces of the irradiated samples are considered to be chemically homogeneous because the whole surface was affected by laser, which is not the case in the femtosecond laser configuration.

In the present case, the XPS data in figure 62 reveal that similar species (metallic oxides and carbides) as the ones found for femtosecond laser ablation appear at the surface of laser structured samples. The thermal process induced by nanosecond laser results in an increase of the thickness of the oxide layer from 4.1 to 6.9 nm.

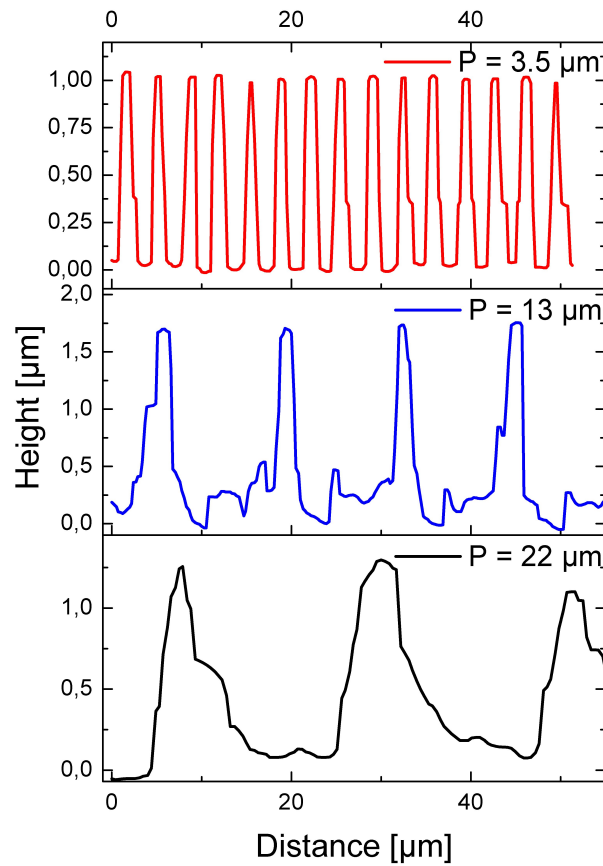


Figure 61: WLI depth profiles of the laser line patterns with 3.5 (a), 13 (b) and 22 μm (c) periods. The 3.5 μm profile is very regular; the 13 μm presents numerous irregularities and “shallow” peaks. They both have rough patterns. The 22 μm structure is more regular and provides the lowest slope of all patterns [102].

5.1.3 Wetting properties

In the present section, the wetting behavior of nanosecond laser structured samples was studied using the drop shape analysis method. The oleophilic and hydrophobic behaviours of the laser textured surfaces were characterized using the FVA 2 oil and distilled water as fluids. All the experiments were performed under room conditions. As previously reported, the choice of the laser pattern can drastically influence certain surface properties such as the reduction of friction [78]. Indeed, the contact angle was measured on the surfaces of line patterns; the samples were oriented perpendicular and parallel to the triple line as described before.

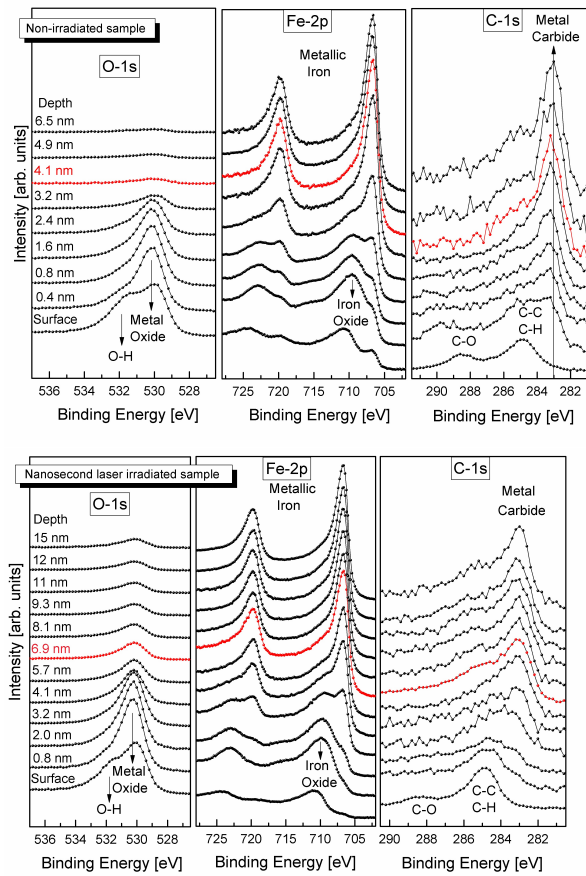


Figure 62: XPS signals of oxygen (O1-S), iron (Fe-2p) and carbon (C1-S) of the (left) unstructured and (right) nanosecond laser-irradiated samples. The thickness of the surface layer containing iron oxide is defined by the depth at which the oxide satellite contribution vanishes (red line).

Figure 63 compares the evolution of the CA of a distilled water droplet for the non-irradiated and laser-irradiated samples. This comparison was performed with a certain structure orientation and period. The non-irradiated surface has a hydrophilic behaviour because the contact angle of the water droplet at the deposition time is $\sim 99.2^\circ$ while after 6 s it becomes $\sim 87.8^\circ$ (figure 63). Compared to the unstructured surface, the laser patterns (perpendicular and parallel) have mostly a hydrophobic behaviour excepted for large periods (figure 64). The laser structure orientation does not have a significant influence on the CA. Both curves have a similar evolution as the period of the laser pattern increases. Regarding to the wetting behaviour, a certain tendency appears, showing that the parallel configuration provides a

smaller CA than the perpendicular orientation except for the $22\ \mu\text{m}$ periodicity (figure 64). Compared to the non-irradiated surface, the laser structure with the $22\ \mu\text{m}$ periodicity always provides a hydrophilic behaviour for both orientations. The perpendicular line patterns induce the smallest contact angle after 6 s (CA $\sim 59.2^\circ$). The perpendicular orientation also provides the most stabilized wetting configuration because of the weak contact angle transition ($\sim 61.4^\circ$ to $\sim 59.2^\circ$ from 0 to 6 s) observed in figure 63.

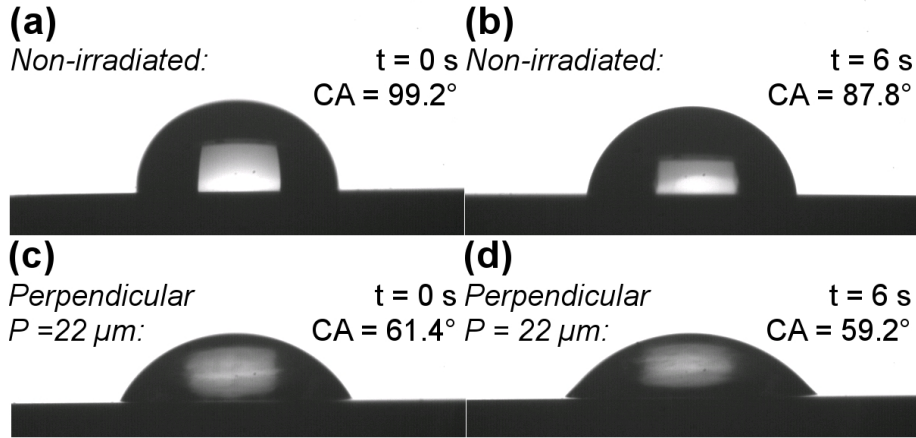


Figure 63: Water droplet evolutions on non-irradiated (a, b) and laser structured surfaces (c, d). On the unstructured surfaces, a transition from hydrophobic (a) to hydrophilic (b) regime is observed in 6 s. The perpendicular structure ($P = 22\ \mu\text{m}$) has a hydrophilic behaviour and also tends to minimize the contact angle (CA) [102].

Considering both perpendicular and parallel orientations, the contact angle decreases while the structure period increases as shown in figure 64. Three distinct zones can be distinguished in the CA curves: the small periods: 3.5 and $5\ \mu\text{m}$; the “middle” periods: 7.5 , 10 and $13.5\ \mu\text{m}$ and the largest periods: 15.5 and $22\ \mu\text{m}$. The highest CA of a water droplet on a structured sample was found to be after 6 s $\sim 106.3^\circ$ for the $5\ \mu\text{m}$ period, while the $3.5\ \mu\text{m}$ structure provides a similar CA around 106.2° . The $13.5\ \mu\text{m}$ period also appears to be strongly hydrophobic with contact angles of about $\sim 101.8^\circ$ and $\sim 95.1^\circ$ for perpendicular and parallel orientations, respectively. Finally, the largest structures provide the smallest contact angles after 6 s and especially the $22\ \mu\text{m}$ patterns.

The previous analyses have shown the strong differences between a flat surface and a precisely controlled topography. It highlights the fact that creating a topography is not sufficient to induce a significant change in the

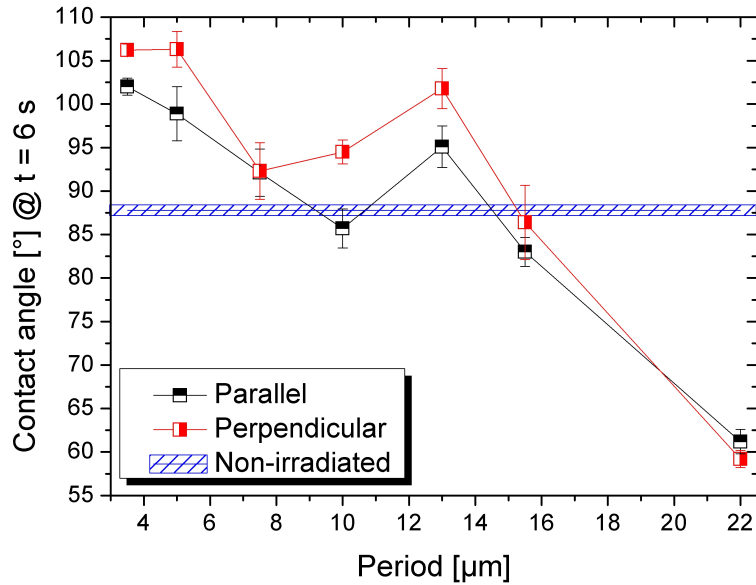


Figure 64: Effect of the laser structure on the contact angle of a water droplet after 6 s. The structure orientation does not have a significant effect on the hydrophobic behaviour while the CA decreases as the period increases [102].

wetting behaviour. Indeed, the hydrophilic tests prove that all the geometrical parameters involved in the patterning process have to be clearly identified and precisely designed. Therefore, it was intended to minimize the roughness at the surface of the non-irradiated/reference samples. In the present study, a one-direction orientation pattern with only one degree of freedom (period) has led to a complicated and unexpected wetting behaviour evolution. A random roughness, characterized by the presence of asperities with various dimensions (pattern, period, high, sharpness), structure densities and orientations (isotropic, circular, concentric, crossed) can then not be used as reference to compare the influence of a controlled topography.

Figure 65 shows FVA 2 droplets on the surface of non-irradiated and laser structured samples. The laser structure is parallel to the surface and was designed with a $22 \mu\text{m}$ period. The parallel orientation leads to the smallest contact angles compared to the perpendicular orientation and non-irradiated state (figure 66). Three configurations ($P = 10; 13; 15.5 \mu\text{m}$) have a contact angle higher than the unstructured state and all of them are perpendicular oriented. Independently of the structure period (figure 66), the parallel structure always provides the smallest contact angle (compared to the unstructured configuration) except for the $13 \mu\text{m}$ period, which is in the same order as the unstructured surface.

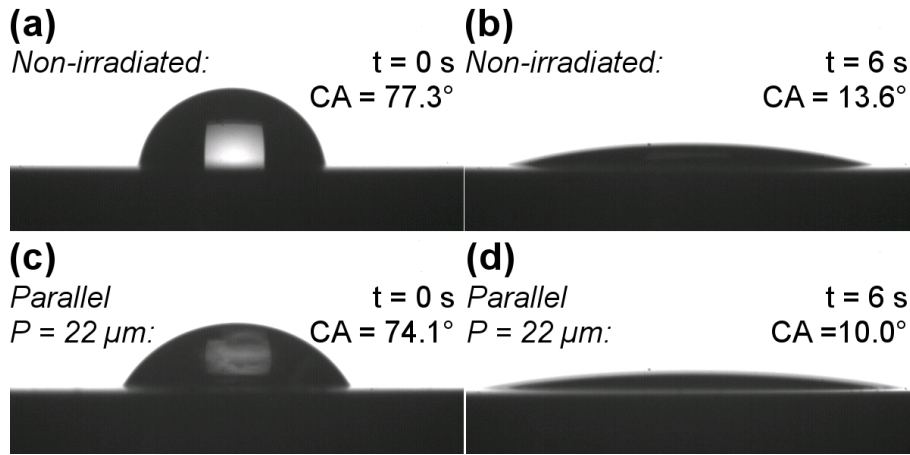


Figure 65: FVA 2 droplet evolutions on non-irradiated (a, b) and laser structured surfaces (c, d). Both surface states have an oleophilic behaviour. The wetting of the non-irradiated surface leads to a 82 % reduction of the CA. The parallel line patterns ($P = 22 \mu\text{m}$) lead to the smallest contact angle after 6 s [102].

In figure 66, the contact angles of an oil droplet after 6 s are represented depending on the structure period. For the perpendicular configuration, the CA increases as P increases and they reach a maximum value for $P = 13 \mu\text{m}$. Then, the contact angle decreases. For the periods between 8 and $16 \mu\text{m}$, the contact angles are greater than in the non-irradiated configuration. In the parallel configuration, it seems that the period of the structure does not have a significant effect on the contact angle. Only the periods 13 and $15.5 \mu\text{m}$ led to angles higher than 10.5° . The maximum value was found for $P = 13 \mu\text{m}$ as for the perpendicular pattern and is in the same range as the unstructured samples.

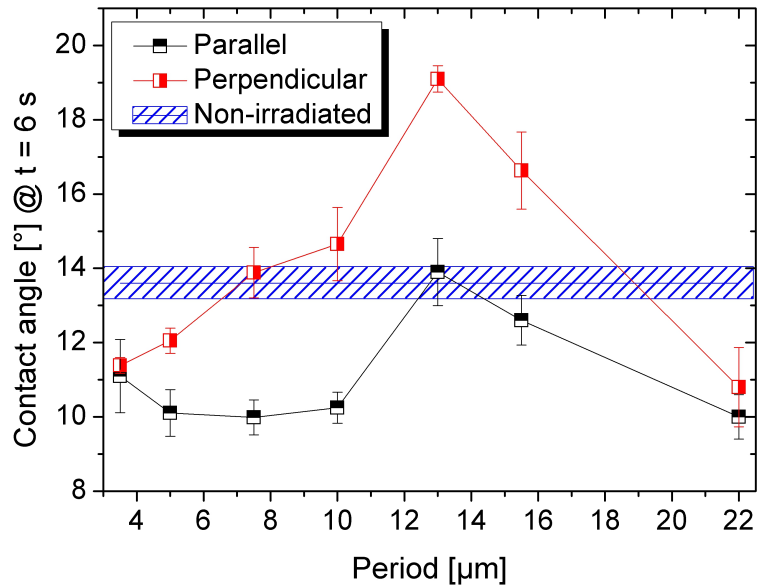


Figure 66: Effect of the laser structure on the contact angle of an oil droplet after 6 s. The structure orientation has a significant effect on wetting behaviour. The parallel line pattern always provides a lower contact angle compared to the perpendicular orientation [102].

In this paragraph, the contact angle measurements showed that the periodicity and the orientation of the line patterns are geometrical parameters, which have major influences on the wetting behaviour of metallic samples. Indeed, it was observed first that when the drop spreads in a direction parallel to the line patterns (i.e. the triple line is perpendicular to the grooves), the CA value tends to be lower than in the perpendicular orientation case. Secondly, the former studies showed that the largest groove provides the smallest contact angles for water and oil.

5.2 Discussion

5.2.1 Chemical analyses

Raman spectroscopy analyses performed on the 22 μm samples revealed that the same species were detected in the non-irradiated, structured-maxima (laser-minima) and structured-minima (laser-maxima) regions. Thus, the chemical compositions of the peak/liquid and valley/liquid interfaces are similar. The high concentration of oxides and carbides in the peak regions can be explained by the formation of the laser line structures. This phenomenon is governed by the Marangoni convection, which is explained as follows: by interacting with the metallic surface, the laser beam induces molten material, which is transferred to the “hottest” region and then solidifies in the “coldest” region. Lu *et al.* used direct laser patterning method in order to structure silicon samples [61]. The Gaussian profile of the laser intensity distribution induced a Marangoni effect in the molten area. Two effects were observed, a thermocapillary effect, which drives the matter from the hot center to the border of the irradiated zone, and a chemicapillary effect that moves the material towards the center. In this work, the laser irradiation was not performed under controlled gas atmosphere but under atmospheric conditions (about $25^\circ\text{C} \pm 2^\circ\text{C}$ and $50\% \pm 5\%$ relative humidity). The molten metal is highly reactive and the oxygen is strongly adsorbed at the surface [143, 144].

5.2.2 Topographical analyses

For this reason, the structured samples are considered as chemically homogeneous. Thus, the control of the topography is the key parameter to study the wetting phenomena. Considering that the behaviour of a perfectly flat surface is hydrophilic (figure 63 b), the generation of roughness by laser texturing ($Rq_{\text{non-irradiated}} \sim 50\text{ nm}$, $Rq_{\text{laser-irradiated}} \sim 580\text{ nm}$) should lead to a more hydrophilic behaviour, according to the model of Wenzel [81]. However, this assumption is not completely valid for all the structures and the wetting behaviour shows to be dependent on the laser periodicity. The Cassie-Baxter model explains the wetting behaviour of rough surfaces [80] by assuming that the droplet deposited on a rough surface cannot completely wet the surface and leads to the formation of composite surfaces. The composite air-solid surfaces are the results of a non-complete wetting, which leads to the superhydrophobic behaviour of micro- [150] and nano-pillars [151]. The hydrophobic behaviour observed for almost all the laser-irradiated samples may be explained by this hypothesis. Nevertheless, Differential Interference Contrast

(DIC) experiments were performed on the wet surfaces as it is shown in the figure 67. No difference in contrast between the peaks and valleys could be observed. Thus, it can be concluded that there is no composite surface and that the Cassie-Baxter model does not explain the results. In contrast to

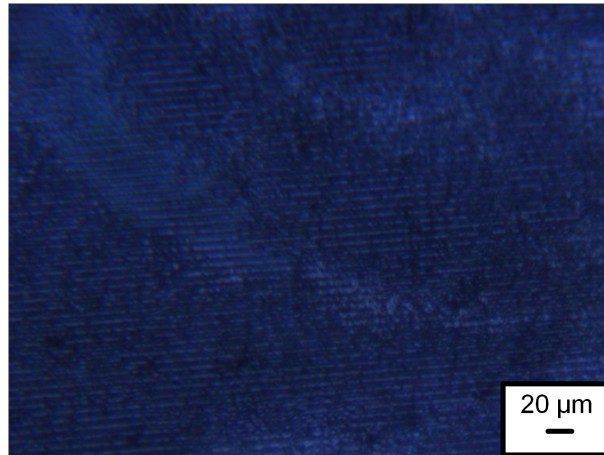


Figure 67: DIC micrographs performed at the surface of nanosecond laser structures using distilled water. The measurements were performed using the $3.5 \mu\text{m}$ periodic samples which have a hydrophobic behaviour. No contrast can be observed between the peak and valley regions, which proves that the Cassie-Baxter model is not valid in the present case.

water, the wetting behaviour of the FVA 2 oil presents a significant dependence of the pattern-orientation. De Gennes, based on the work of Mason [84] and Cox [152], proposed to explain the anisotropy showed by the periodical line-patterns in *Wetting: statics and dynamics* [83]. He affirmed that in the case of parallel orientation (triple-line perpendicular to the grooves), the fluid would be free to flow inside the groove acting as a capillary channel. This effect was previously observed by Shuttleworth [153] and Oliver [154]. In the case of perpendicular orientation (triple line parallel to the grooves), the droplet is pinned by the grooves, acting as a physical barrier. De Gennes proposed that the overlapping of these energy barriers [155] is not an “overall jump” of the line but a jump in a single point. After having passed these barriers, the liquid flows inside the grooves. These phenomena justify the observations that the parallel orientation provides a better wetting of the surface because the laser line pattern acts as capillary flow channel, while the perpendicular orientation requests more energy to cover the same distance. The CA of the water droplet on the structured surfaces shows a strong dependency on the pattern periodicity (figure 64). This phenomenon

is correlated with the “effect of the edge” [156] as found by Oliver and Mason after measuring the wetting behaviour of a droplet on triangle and sinusoidal profiles [154]. The configurations of 13 and 15.5 μm of period showed higher CA for both perpendicular and parallel orientations. In figures 60 and 61, it is clearly observed that the 13 μm patterns present irregularities compared to the other structures. Even if these topographical faults are smaller than the regular peaks (around 0.5 μm), they increase the number of energy barriers and prevent wetting. Moreover, the heterogeneities in the 13 μm patterns act as a *reservoir* by retaining oil in all the topographical “cavities and ramifications” leading to the CA maxima observed in both parallel and perpendicular configurations.

5.2.3 Simulation analyses

Simulation studies were performed and revealed the difficulties and limits of three-dimensional simulation yet. The wetting behaviour of nanosecond laser structures was studied using Comsol MultiPhysics ©. The design of the laser patterns was made using HyperMesh ©, a finite element pre-processor, since a three-dimensional resolution was necessary to simulate the effects of the pattern orientation (perpendicular and parallel) and of the geometrical parameters (depth and period). As shown in figure 68, the effect of the struc-

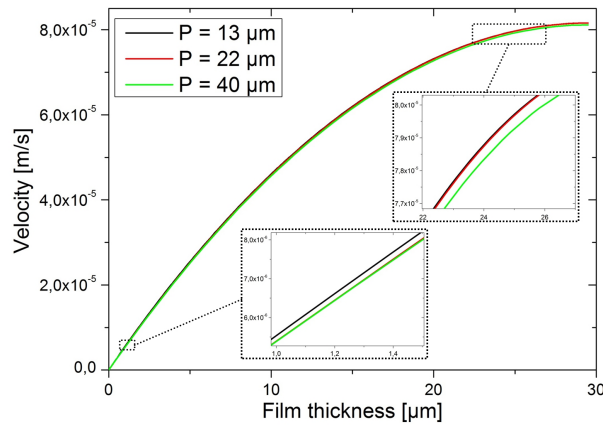


Figure 68: Simulated fluid velocity gradients as a function of the fluid thickness and depending on the period of the laser groove in a parallel pattern orientation. As the period of the structure increases, the velocity decreases, which confirms the Jurin’s law. The speeds were calculated using the Comsol Multiphysics © software.

ture period was demonstrated for a parallel configuration. Indeed, simulation

curves prove that as the period increases, the fluid velocity decreases. This observation confirms that the spreading of fluid in laser grooves is related to the capillarity effect represented in the Jurin's law. Finally, the simulation

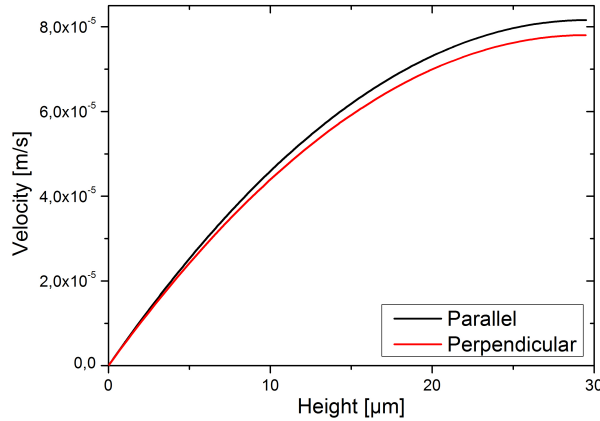


Figure 69: Simulated fluid velocity gradients as a function of the fluid thickness and depending on the laser pattern orientation. The parallel orientation shows a higher speed gradient than the perpendicular orientation. This observation confirms that the perpendicular patterns are energetic barriers to the fluid spreading and slow down its velocity.

revealed that the orientation of the pattern is a key parameter to understand and control the wetting phenomena, since it is shown in figure 69 that the fluid velocity is slowed down by the presence of obstacles (i.e. the perpendicular orientation). The simulation confirmed that these phenomena might be related to the capillarity effects and the obstacles induced by topographical grooves oriented parallel to the triple line.

First, errors occurred due to the three-dimensional modelization. Limitations appeared to design precisely the grooves due to the complicated geometrical dimensions and irregularities such as the radius of curvature that were taken into account. Moreover, the simulation was performed assuming that a limited volume would be representative of the effects occurring at the surface of the irradiated samples while the fluid was spreading on it. The limited volume dimensions are an important issue since they did not allow finer meshing and simulations. Secondly, the boundary conditions applied such as the free wall and more precisely the fluid velocity are a reason of the incomplete achievement of this algorithm. Indeed, the fluid velocity applied was extrapolated from the videos taken during the contact angle measurements. The speed was calculated using the original diameter of the deposited drop subtracted from the drop size at a certain time divided by the corresponding time period.

Since the contact angle measurement itself requires the identification of the syringe diameter, the diameter calculated at each time could be converted from a pixel scale to a meter scale as it is represented in the figure 70. The fluid velocity was then calculated at the basis of the droplet and precisely represents the speed evolution of the triple point. Nevertheless, it has to be considered that, since in the algorithm the speed was applied inside the fluid and even if the height of fluid volume simulated was not consequently high, this difference might induce a probable "scale" problem.

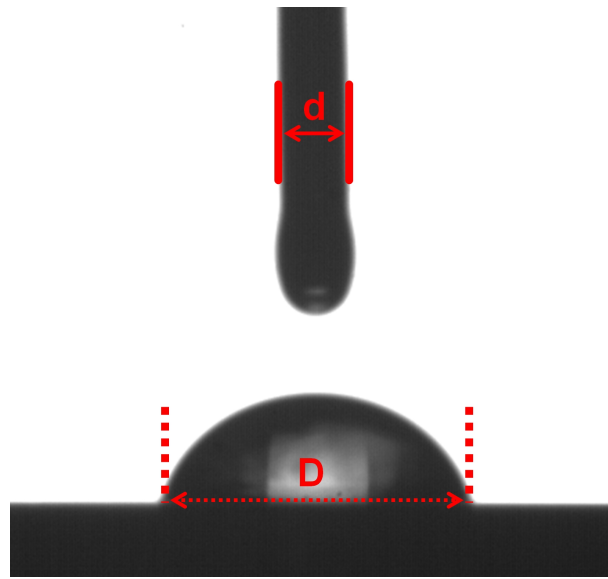


Figure 70: Snapshot used for the determination of the fluid velocity at the deposition time. The diameter of the syringe (d) is known and recognized before each measurement. D , the diameter of droplet is converted, from a pixel to a mm scale using d as a reference for the conversion. At various times, D varies and then the velocity can be extrapolated.

5.3 Conclusions

In this section it was shown that the nanosecond laser and steel interactions have an influence on the concentrations of oxides and carbides at the surface of the laser irradiated. Since the LIMET process involves the melting of the irradiated matter and its transfer (from high intensity to low-intensity regions) under ambient atmospheric conditions, oxidation phenomena occur leading to a chemically homogeneous surface. The wetting analyses showed an anisotropy in the spreading of the fluid according to the theory developed by de Gennes. The geometrical parameters such as period, height i.e. slope of the grooves and of course the regularity of the patterns control the wetting of the surface by acting as barriers or capillary channels. Finally, fluid flow simulations were performed in order to confirm the phenomena involved in the wetting of surfaces irradiated using LIMET. While boundary conditions can still be discussed and the algorithm can also be improved, the velocity curves confirm theoretical and experimental phenomena. First, the increase of the period shows a decrease of the fluid velocity in the parallel configuration, which proves that the wetting of parallel oriented laser grooves is linked with the capillarity behaviour of the Jurin's law. Then, the effects of the groove orientation were highlighted since the fluid spreading velocity was slowed down by the perpendicular laser lines. It also confirms that they act as energetic barriers and obstacles in comparison to parallel oriented grooves.

6 Optimized structures: femto- and nanosecond structure combination

6.1 Results

The goal of this section is to report the effects and benefits of a structure elaborated with femtosecond and nanosecond laser. The principle of this combination is to irradiate the surface of a sample previously structured using femtosecond laser by means of LIMET.

6.1.1 Topographical analyses

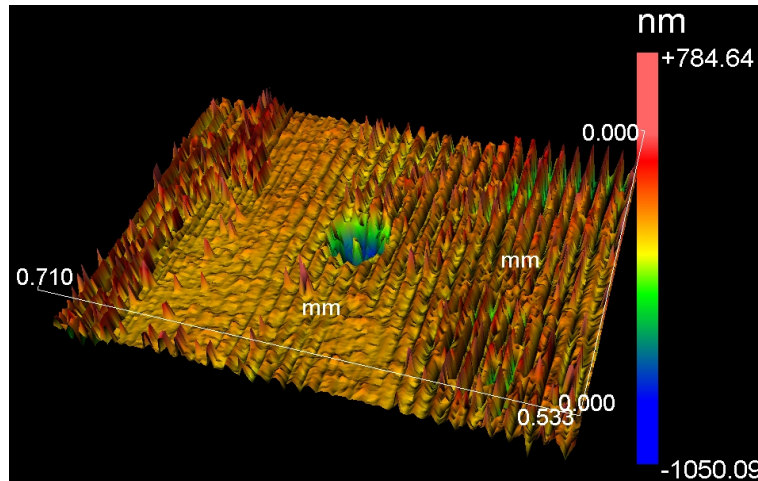


Figure 71: Tridimensional overview of the surface of the combined patterns taken using the WLI. The superposition of the two structures can be easily recognized.

Regarding to the former studies, it was decided that the so-called "femtostructure" chosen for these experiences will have the following dimensions resumed in the table 8. It has then been irradiated with a line pattern with $22 \mu\text{m}$ periodicity. These dimensions were chosen in order to create a structure combining the advantages of the preferential oriented wetting due to the LIMET patterns and the role of *reservoir* allowed by the femtostructure.

The topography of the combined structures was investigated using the WLI and a tridimensional overview and a profile snapshots are represented in figures 71 and 72. The observation of the 3D picture shows that the crater,

	$[\mu\text{m}]$
Depth	1
Diameter	110
Periode	500

Table 8: Dimensions of the femtosecond laser patterns used for the combined structure.

even with a depth in the order of magnitude of the grooves height can still be easily distinguished from the other patterns. Furthermore, as visible in the 3D overview and more clearly in the two-dimensional profile, the line patterns are precisely structured on the surface of the sample and even partially at the bottom of the "femto" craters. The whole patterns are not completely structured on the walls and at the basis of the cavities but there is a certain continuity of the grooves inside, which can be recognized in picture 73. This observation has to be carefully considered regarding the potential influence it might have on the wetting behaviour.

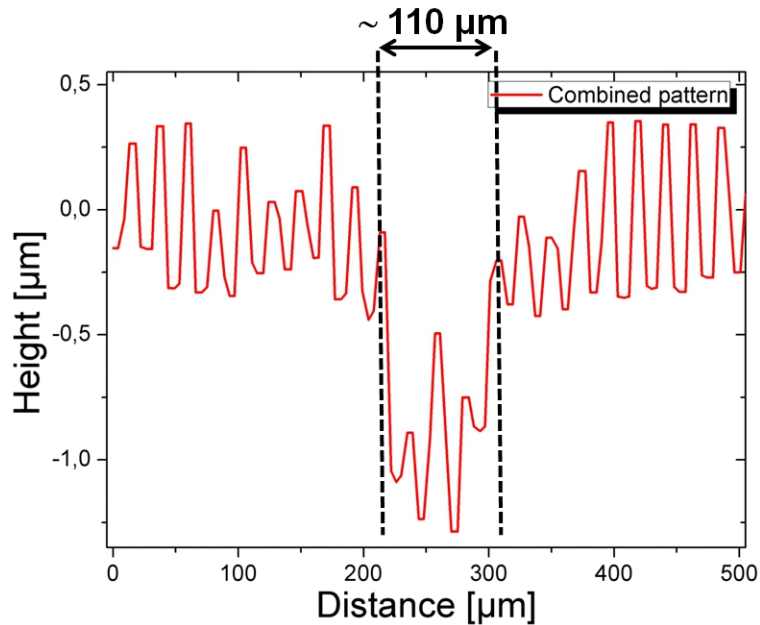


Figure 72: Profile of the combined patterns taken using the WLI. The two "superposed" patterns (line and crater) of the two structures can be easily recognized.

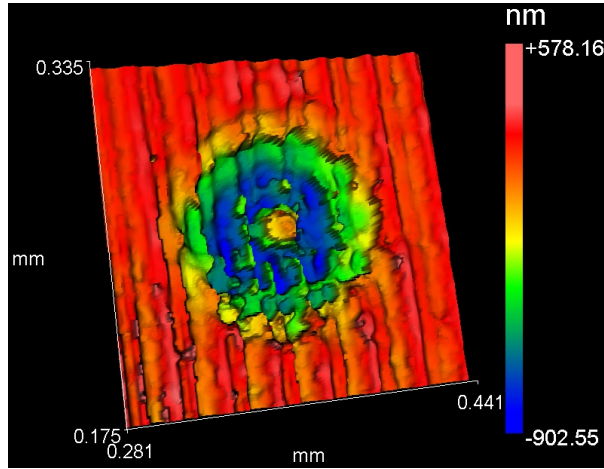


Figure 73: 3D magnification of a crater using WLI after femto and nanosecond irradiations. The 3D picture shows the partial continuity between the line patterns outside and inside of the cavity.

6.1.2 Wetting properties

The wetting behaviour of the combined structures was studied using the FVA 2 oil. The curves plotted in figure 74 confirm that the line patterns governed the wetting of the oil droplet. Indeed, the anisotropy shown by the LIMET structures is also clearly demonstrated according to the time evolutions. The CA measured in the parallel configuration are permanently lower than in the perpendicular configuration. A difference of 1° is observed between the two final values of the CA and the error bars are in the same order of magnitude. Besides, they show a similar tendency as for the LIMET behaviour, due to the superposition of the values observed in the figure 66 for both $22 \mu\text{m}$ periodicity configurations. In the figure 75, the wetting behaviour of the combined structure is compared to the behaviour of line and dot patterns created by nano- and femtosecond laser irradiation, respectively. The curves show, first, that the combined patterns provide the highest CA values during the initial phase of the wetting (from the deposition and during almost 1 s). Then, the optimized surface seems to have a wetting behaviour similar to the dot patterns. The final measurement magnified in the inset (6 s after deposition) shows that the CA of the optimized structure is not more stable than the dot patterns. Finally, the inset highlights the fact that the optimized structure has a wetting behaviour for oil, which is a compromise between the femto- and nanostructure behaviours.

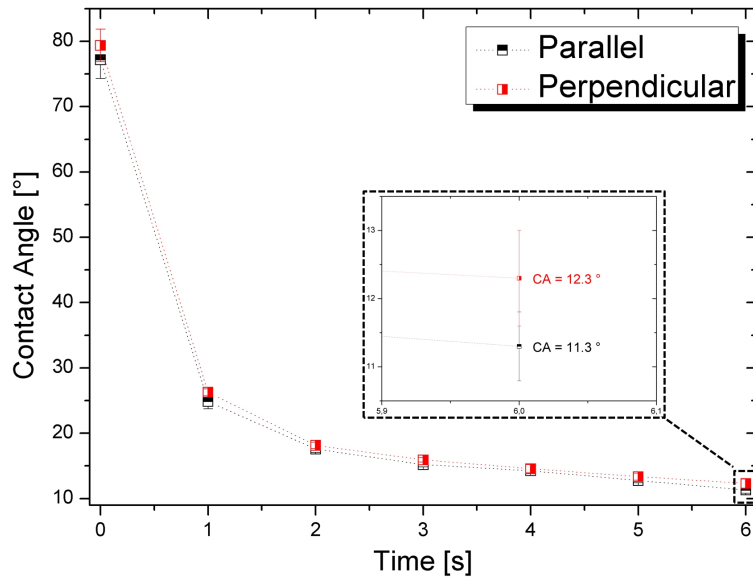


Figure 74: Contact angle measurements using FVA 2 oil performed on the surface of the combined patterns depending on their orientation. The curves and the inset clearly show that the line pattern orientation has a crucial effect on the value of the contact angle.

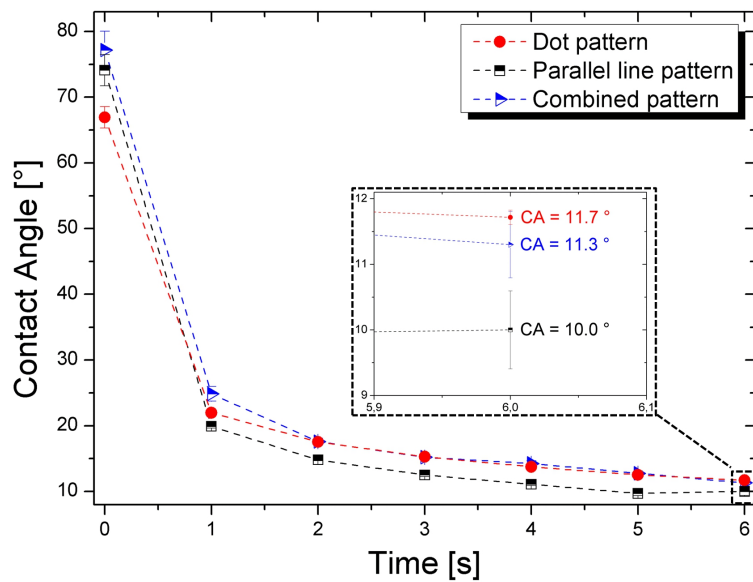


Figure 75: Contact angle measurements using FVA 2 oil performed on the surface of the combined, line and dot patterns. The combined patterns have a wetting behaviour combining the effects of both dot and line structures.

6.2 Discussion

The topographical analyses performed previously have revealed that the overlapping of both femto- and nanosecond laser structures induces very precise patterns. The choice of the geometrical dimensions of the two laser structures is of crucial importance, obviously for the wetting properties but also for the topographical analysis. The grooves must be easily distinguished in comparison to the former created structures in order to understand the effects of the laser patterns. Indeed, the nanosecond laser irradiated surface is made of the juxtaposition of square areas between 2 and 4 μm^2 each. As it has been detailed in the *Experimental* part of this thesis and in a previous work [78], a consequent area is then treated. Each laser spot of this area entirely recovers a single femtosecond laser cavity, since the femtosecond laser irradiated area is of about $1 \times 10^{-2} \mu\text{m}^2$ with a theoretical diameter of 110 μm . Moreover, since the LIMET is based on the principle of interference of light, the minimum and maximum of laser light intensity affect the whole femtosecond irradiated zones. Consequently, no area is kept non-irradiated but the nanosecond laser do not destroy any femtosecond laser hole. The forming process related to the LIMET has the advantage to be easily controlled and to preserve the created cavities in comparison to other techniques such as microcoining or embossing processes. Kim *et al.* reported experimental and numerical studies performed on stainless steel using microcoining [157]. This study details the main effects observed after various coining procedures. The experimental procedure for the elaboration of samples consists of using a "*compression testing system*" and a "*die/punch*" as shown in the figure 76 at normal loads of about 650, 1000 and 2800 kN. Authors created various patterns by changing the geometrical parameters (height and width) of the embossed grooves. They finally observed that the material behaviour was influenced by two effects: the weakening of the material was changed due to the "*Hall-Petch relationship related to the effect of grain size*" and due to the small scale elaboration of the structures or so-called "*miniaturization of the features*". Authors summarized their work by concluding that the microcoining procedure allows the elaboration of well-defined geometries but the material behaviour is clearly changed in comparison to the original or as-received state of the samples. It has to be noticed that even if the laser patterning does not change the material behaviour, similar micro geometries cannot be easily created by LIMET actually. Indeed, the LIMET allows the creation of patterns with a maximal periodicity of about 30 μm while Kim *et al.* created patterns about ten times larger [157]. This quality is of prior interest for hard and soft bulk materials because the original topography is still intact after the procedure. Secondly, the microstructure of the material

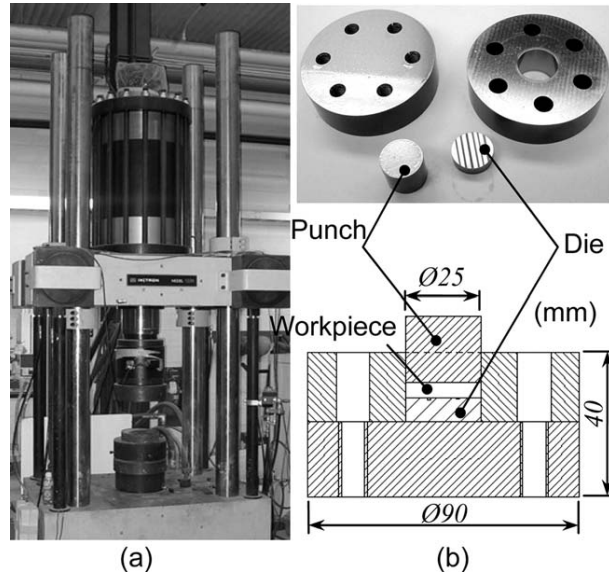


Figure 76: Experimental setup and fabricated punch/die set: (a) compression testing system and (b) die/punch set [157]. The embossing process involves normal forces higher than 650 kN and changes the average grain size from 64 originally to 51 and 135 μm .

is still intact after the laser irradiation, no internal stress is induced as it could be the case for materials which have been plastically deformed. Indeed, in addition to the lack of destruction due to the contact of two bulk materials, there is also no plastic deformation and no strong recrystallization phenomenon could be detected after using both femto- and nanosecond laser. Both laser irradiation procedures involved in this thesis were performed at low laser fluences, which were clearly not sufficient to induce recrystallization phenomena. Moreover, since the 100Cr6 steel has a large averaged grain size of about 19 μm , the energy brought by the laser could only locally change the microstructure, where the femtosecond laser fluence was the highest as in the ablation zone investigated using TEM. In the case of the nanosecond laser irradiation, the microstructural study of laser patterned bulk copper showed that a misorientation zone appeared randomly inside the laser irradiated area and directly below the surface [78]. It proves the presence of plastic strain fields as it is showed in figure 77. The maximum misorientation detected in the laser irradiated zone is about 9.8 $^\circ$, which corresponds to a small proportion of orientation according to Badji *et al.* [158]. These small misorientation zones are generated due to the typical quenching rates of laser treatment which can reach 10^{10} K/s [16]. Despite the lack of statistical studies, these observations reveal that the laser irradiation cannot tailor

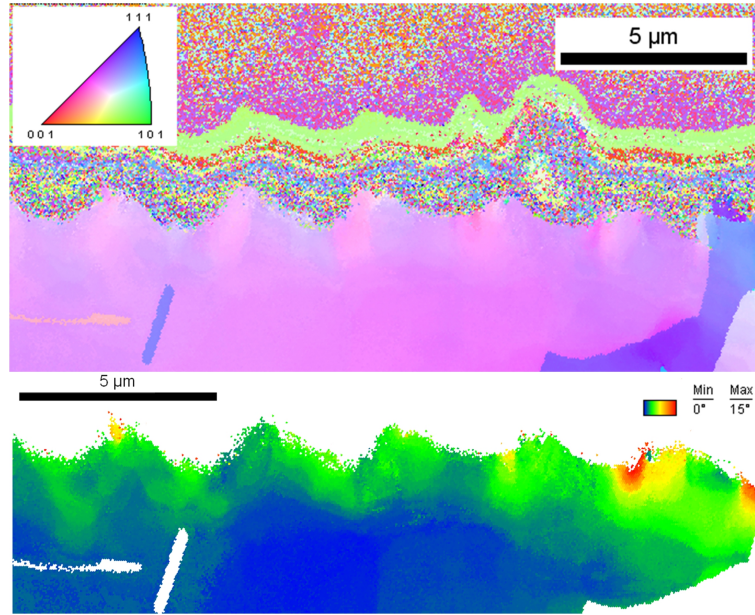


Figure 77: Inverse pole figure map of laser structured samples perpendicular to the surface and corresponding crystal orientation map with a grain delimitation higher than 5° . The LIMET procedure did not induce any preferential orientation. The maximum misorientation is detected below the surface [78].

the texture and grain orientation of bulk metallic samples. However, it can be considered as an important advantage since these previously-mentioned properties stay unchanged and in their original states. Nevertheless, since one of the motivations of this thesis was to create an "*optimized structure*" for wetting applications, the attention was focused on microscopic aspects of the laser patterning. Indeed, the nanosecond laser irradiation has certainly deleted certain femtosecond structures such as the ripples. The ripples probably do not affect the spreading properties of the combined structures in comparison to the nanosecond laser grooves since their height and period are around $0.1/1$ and $1/22 \mu\text{m}$ for ripples and nanosecond lines, respectively. Meanwhile, prior to the LIMET irradiation, the samples treated by femtosecond laser were oriented in order to have the same preferential orientation for the both previously mentioned structures.

6.3 Conclusions

These prior experiments were performed in order to combine the wetting behaviours of both patterning methods, the femtosecond laser ablation and the nanosecond laser interference metallurgy. Topographical analyses showed that a smart choice of the geometrical parameters (period, depth, diameter, and orientation) allows a superposition of both structures leading to a hierarchical pattern at a micro-scale and based only on light sources. Such combination allows the development of an optimized structure with the advantages of both patterning techniques: a *reservoir* effect and an increased spreading velocity. Indeed, the CA measurements showed that the optimized surfaces have a CA evolution between the femtosecond and nanosecond laser structures with similar geometrical parameters. It confirms that this superposition of both laser patterns was successfully employed, leading to an optimized structure which combines the best of both laser techniques

7 Conclusions and outlook

7.1 Conclusions

In the present thesis, two distinct methods based on different laser-material interactions were set-up in order to tailor the wetting properties of bulk 100Cr6 steel samples.

First of all, a Ti:sapphire femtosecond laser was used to design the chemical and topographical surfaces of the steel samples with a very high precision. This patterning method is based on the ablation phenomena of metallic materials interacting with ultrashort laser pulses. Various patterns were obtained by changing the geometrical parameters of the structures such as depth, periodicity i.e. structure density. Moreover, a significant tailoring of the wetting and bearing behaviours was observed which are both directly related to the topographic modifications. Despite significant changes of the chemical concentrations were detected, too.

Laser interference metallurgy experiments were also performed using a nanosecond Nd:YAG laser. While this patterning technique is known and was well developed at the chair of *Functional Materials* for more than a decade, the anisotropic properties of the line structures were used as an innovative step to design and control the wetting behaviour of the samples. The wetting of a droplet on a line-patterned surface is dependent on the angle between the triple-line and the material grooves according to the theoretical considerations of de Gennes. Indeed, the LIMET patterns have a fundamental influence on the wettability. The periodicity and the orientation of the structures were both studied and showed a significant influence on the contact angle measurements.

Both femtosecond and nanosecond laser irradiation processes allow to create chemical gradients. Since the laser intensity varies according to a Gaussian distribution, the laser-matter interactions change according to a similar repartition. The ablation phenomena using the femtosecond laser system induced laser-matter interactions which are directly related to this spatial distribution in comparison to the nanosecond laser and the LIMET process. The analyses performed showed a higher quantity of metallic oxides and carbides in the irradiated zones in comparison to the non-irradiated state. Moreover, the presence of amorphous carbon was found to decrease

from the outer region of the irradiated samples (unstructured) to the centre of the laser-irradiated zone (ablation zone). It was also demonstrated that the formation of amorphous and crystalline carbon depends on the distribution of the laser intensity and that the use of a high number of pulses lead to the amorphization of the irradiated zones according to the melt-quenching phenomena. APT analyses also demonstrate that the fs laser irradiation induces chemical modifications in the first few nanometres of steel surfaces. Moreover, it confirms that the chemical changes are highly dependent on the laser intensity distribution. The irradiation induces oxidation of Fe into Fe_2O_3 and generates depletion regions. The ablation process modifies the spatial distribution of C in the steel matrix. Finally, microstructural modifications were revealed by the TEM analyses performed in the laser ablation zones. TEM showed that the laser irradiation induced a crystallographic deformation of the steel bulk in the high laser-intensity region (ablation zone). The effects of the nanosecond laser irradiation were also investigated using XPS and Raman spectroscopy. It was concluded that the surfaces irradiated using LIMET are favorable to the oxidation, since the oxide layer became thicker after the laser process. The Raman spectroscopy showed that the chemical species detected in the laser irradiated and non-irradiated surfaces are similar. A comparison between the high and low intensity regions was also performed and the Raman spectra showed similar species in both regions. Nevertheless, a difference in iron oxide concentrations was found depending on the laser intensity distribution and was due to the Marangoni convection phenomenon.

The chemical analyses of the different irradiated surfaces have shown that the femto and nanosecond laser induced a significant increase in the oxide and metallic species concentrations. Nevertheless, no concentration change can be defined as significant for the control of the wetting behaviour since all chemical species detected in the laser irradiated zones were already present at the surface of the material before laser treatment.

It has been successfully demonstrated in this thesis that the wetting behavior of 100Cr6 industrial steel surfaces can be tailored by designing precise interference patterns using nanosecond-laser radiation. Indeed, since the laser irradiation procedures under normal atmosphere conditions did not induce new chemical species at the surface of the samples, the wettability of the material is controlled by geometrical effects. The experiments performed have showed two distinct paths to create different patterns involving laser matter interactions. First, it was demonstrated that the laser ablation is an interesting way to tune the wettability of metallic materials. By changing

the periodicity i.e. the density and the pattern (e.g. depth, diameter, profile), the spreading of the fluid can be accelerated or slowed down. Indeed, the fluid requires more energy to overpass the different obstacles (energetic barriers) if the cavity profile is too abrupt. Experiments proved that increasing the structure density (i.e. reduce the periodicity) decreases the contact angle. It shows that the laser cavities (with optimal diameter and depth) are preferential sites which did not reduce the spreading velocity of the fluid in comparison to extended flat surfaces. The contact angle measurements have clearly showed that the laser cavity had a *reservoir* role, which is an interesting property to create regular fluid pockets at the surface of the material. Secondly, LIMET patterns also showed their ability to tune the spreading speed of a fluid. Depending on the pattern orientation and periodicity, the surface modification can lead to hydrophobic and/or hydrophilic behavior. The parallel orientation provides a better wetting of the surface because the laser line-patterns act as capillary flow channels, while the perpendicular orientation imposes energy barriers that prevent wetting. The wetting coverage is more effective for large than for small period structures. This effect leads to tailor the hydrophobic (small periods) or hydrophilic (large periods) behavior, depending on the kind of liquid to be used. Similar wetting effects occur for oil after laser structuring, but no transition from oleophilic to oleophobic was observed. The change of structure periodicity has also induced modifications of the pattern slope and regularity. Indeed, non-desired defaults of the patterns have a negative effect on the fluid spreading since they act as "micro" energetic barriers which prevent a regular and constant wetting of the droplet. Finally, the orientation of the line patterns is obviously the most determinant parameter for line patterns. Indeed, the results showed that it determines if the triple line will be blocked or free to move according to the theory of de Gennes.

To conclude, the combination of two laser methods which are fundamentally different regarding their interactions and their usual applications is a success to provide new laser patterns at the surface of metallic materials. The interlocking of both patterns lead to a perfect mix of the properties observed separately. Indeed, instead of annihilating the effects of each other, the ablation cavities have a *reservoir* role with a preferential spreading orientation. This combination technique clearly offers new patterning opportunities to correct the disadvantage of each method.

7.2 Outlook

In this thesis, new approaches were successfully developed to characterize the effects of laser irradiation and to design new wetting properties of metallic materials. Nevertheless, some points could probably be improved in the future in order to take significant advantages of this work.

First of all, since the LIMET and mostly the femtosecond laser ablation have an effect on the chemical composition of the material surface, it could be very promising to use samples with a precise, regular and periodic repartition of chemical species. Indeed, the *choice of the material* is of crucial importance for further studies. The random distribution of the chemical species (oxides, carbides) was a negative point in order to tailor the material surface chemically. Secondly, the choice of a material with a regular chemical surface could be a solution to prevent the formations of cone structures. Indeed, their formation is related to the random presence of impurities at the surface of the irradiated area. The choice of thin "*sandwich*" films to be irradiated could be a very interesting alternative since the ablation and LIMET processes may precisely remove or create compounds. Since the femtosecond laser ablation allows to remove material at a very precise depth, it may be promising to remove a certain quantity of matter in a thin film sample. For example, in the case of a Ni/Al configuration, the top layer of Ni could be periodically removed creating a surface with precisely distributed Al areas. This combination of laser ablation and chemical texturing might be very interesting in the future, since the femtosecond laser ablation can create shallow cavities (0.4 μm depth in 100Cr6 bulk samples) without changing the microstructure of the material.

The laser treatment under ambient *atmospheric conditions* is also an obvious field of discussions. Indeed, since metallic materials are exposed to dioxide molecules under non-controlled atmosphere, oxidation may irregularly occur depending on the ambient temperature and relative humidity. Then, the laser treatment under vacuum or gas atmosphere is of prior interest since it might be a solution to combine reactive sites (i.e. irradiated material surfaces) with gas molecules, which could thus become sites with new and different compounds from the non-irradiated areas. In this case, the procedure might be the solution to add at the surface of the material compounds which could further have an influence on the wetting properties.

All along this thesis, two distinct techniques involving different laser technologies were used to design the topography of the material. In both cases

defaults appeared at the surface after laser irradiation. Since they directly influence the wetting phenomena, the homogeneity of the structures has to be improved. It is mainly possible to do this by improving the irradiation processes. Meticulous calculations have to be performed in order to determine the most adapted set-up parameters chosen for the laser irradiation. In this conditions, for example the bridges of molten matter observed between the LIMET lines, could be avoided.

Using these considerations, it might be helpful to find the *physical limits* of each laser system. For example, the extreme period and height for the grooves should be calculated and then applied to a chosen metallic surface in order to study and compare the effects and interactions observed in this thesis.

Finally, it was showed that all the geometrical parameters (shape, period and depth) of the patterns determining the *design* of the structure are the key parameters to understand and tune the wettability. In the future, the elaboration of complex patterns based on the design of the optimized structures might be a solution to improve self-cleaning applications or lubrication phenomena for example. Hierarchical structures involving laser and embossing techniques have already been used for tribological applications and the success of the optimized patterns to combine different effects has to be scientifically and industrially considered.

References

- [1] L.O. Lucifora, R.C. Menni, and A.H. Escalante. Analysis of dental insertion angles in the sand tiger shark, *carcharias taurus* (chondrichthyes: Lamniformes). *Cybium*, 25(1):23–31, 2001.
- [2] A.V. Singh, A. Rahman, NVG Sudhir Kumar, AS Aditi, M. Galluzzi, S. Bovio, S. Barozzi, E. Montani, and D. Parazzoli. Bio-inspired approaches to design smart fabrics. *Materials and Design*, 36:829–839, 2012.
- [3] B. Bhushan. Biomimetics: lessons from nature—an overview. *Philosophical Transactions of the Royal Society A: Mathematical, Physical and Engineering Sciences*, 367(1893):1445–1486, 2009.
- [4] J. Oeffner and G.V. Lauder. The hydrodynamic function of shark skin and two biomimetic applications. *The Journal of Experimental Biology*, 215(5):785–795, 2012.
- [5] R. Grüneberger and W. Hage. Drag characteristics of longitudinal and transverse riblets at low dimensionless spacings. *Experiments in Fluids*, 50(2):363–373, 2011.
- [6] D.W. Bechert, M. Bruse, and W. Hage. Experiments with three-dimensional riblets as an idealized model of shark skin. *Experiments in fluids*, 28(5):403–412, 2000.
- [7] E.A. Favret. *Functional properties of bio-inspired surfaces: characterization and technological applications*. World Scientific Pub Co Inc, 2009.
- [8] T. Hollstein, W. Pfeiffer, and R. Zeller. Mechanical properties and wear behaviour of differently machined silicon nitride and silicon carbide ceramic surfaces. *Ceramic materials and components for engines*, pages 157–161, 2001.
- [9] E. Willis. Surface finish in relation to cylinder liners. *Wear*, 109(1):351–366, 1986.
- [10] U. Pettersson and S. Jacobson. Influence of surface texture on boundary lubricated sliding contacts. *Tribology International*, 36(11):857–864, 2003.
- [11] A. Erdemir. Review of engineered tribological interfaces for improved boundary lubrication. *Tribology International*, 38(3):249–256, 2005.

- [12] C. Gachot, P. Leibenguth, and F. Mücklich. Tribological properties of laser interference induced microstructural architectures in metallic systems. *Friction, wear and wear protection*, pages 59–66, 2009.
- [13] Y. Gerbig, G. Dumitru, V. Romano, V. Spassov, and H. Haefke. Effects of laser texturing on technical surfaces. In *MATERIALS RESEARCH SOCIETY SYMPOSIUM PROCEEDINGS*, volume 750, pages 455–460. Cambridge Univ Press, 2003.
- [14] F. Mücklich, A. Lasagni, and C. Daniel. Laser interference metallurgy:- using interference as a tool for micro/nano structuring. *International journal of materials research*, 97(10):1337–1344, 2006.
- [15] M. Hans, C. Gachot, F. Müller, and F. Mücklich. Direct laser interference structuring as a tool to gradually tune the wetting response of titanium and polyimide surfaces. *Advanced Engineering Materials*, 11(10):795–800, 2009.
- [16] C. Gachot, R. Catrin, A. Lasagni, U. Schmid, and F. Mücklich. Comparative study of grain sizes and orientation in microstructured au, pt and w thin films designed by laser interference metallurgy. *Applied Surface Science*, 255(10):5626–5632, 2009.
- [17] M. D’Alessandria, A. Lasagni, and F. Mücklich. Direct micro-patterning of aluminum substrates via laser interference metallurgy. *Applied Surface Science*, 255(5):3210–3216, 2008.
- [18] F.C. De Lucia, J.L. Gottfried, and A.W. Miziolek. Evaluation of femtosecond laser-induced breakdown spectroscopy for explosive residue detection. *Optics express*, 17(2):419–425, 2009.
- [19] B.C. Stuart, M.D. Feit, S. Herman, A.M. Rubenchik, B.W. Shore, and M.D. Perry. Optical ablation by high-power short-pulse lasers. *JOSA B*, 13(2):459–468, 1996.
- [20] S. Preuss, A. Demchuk, and M. Stuke. Sub-picosecond uv laser ablation of metals. *Applied Physics A: Materials Science & Processing*, 61(1):33–37, 1995.
- [21] C. Momma, B.N. Chichkov, S. Nolte, F. von Alvensleben, A. Tünnermann, H. Welling, and B. Wellegehausen. Short-pulse laser ablation of solid targets. *Optics communications*, 129(1):134–142, 1996.

- [22] B.N. Chichkov, C. Momma, S. Nolte, F. Von Alvensleben, and A. Tünnermann. Femtosecond, picosecond and nanosecond laser ablation of solids. *Applied Physics A: Materials Science & Processing*, 63(2):109–115, 1996.
- [23] Y. Hirayama and Obara M. Heat effects of metals ablated with femtosecond laser pulses. *Applied Surface Science*, 197–198(0):741 – 745, 2002.
- [24] S. D. Brorson, A. Kazeroonian, J. S. Moodera, D. W. Face, T. K. Cheng, E. P. Ippen, M. S. Dresselhaus, and G. Dresselhaus. Femtosecond room-temperature measurement of the electron-phonon coupling constant γ in metallic superconductors. *Phys. Rev. Lett.*, 64:2172–2175, Apr 1990.
- [25] B. Delobelle, F. Courvoisier, and P. Delobelle. Morphology study of femtosecond laser nano-structured borosilicate glass using atomic force microscopy and scanning electron microscopy. *Optics and Lasers in Engineering*, 48(5):616–625, 2010.
- [26] C.S. Nielsen and P. Balling. Deep drilling of metals with ultrashort laser pulses: A two-stage process. *Journal of applied physics*, 99(9):093101–093101, 2006.
- [27] J. Ihlemann, A. Scholl, H. Schmidt, and B. Wolff-Rottke. Nanosecond and femtosecond excimer-laser ablation of oxide ceramics. *Applied Physics A: Materials Science & Processing*, 60(4):411–417, 1995.
- [28] T.V Kononenko, S.V Garnov, S.M Klimentov, V.I Konov, E.N Loubnin, F Dausinger, A Raiber, and C Taut. Laser ablation of metals and ceramics in picosecond–nanosecond pulsewidth in the presence of different ambient atmospheres. *Applied Surface Science*, 109–110(0):48 – 51, 1997.
- [29] M. Huang, F. Zhao, Y. Cheng, N. Xu, and Z. Xu. Origin of laser-induced near-subwavelength ripples: interference between surface plasmons and incident laser. *ACS nano*, 3(12):4062–4070, 2009.
- [30] U. Chakravarty, RA Ganeev, PA Naik, JA Chakera, M. Babu, and PD Gupta. Nano-ripple formation on different band-gap semiconductor surfaces using femtosecond pulses. *Journal of Applied Physics*, 109(8):084347–084347, 2011.

- [31] S. Hou, Y. Huo, P. Xiong, Y. Zhang, S. Zhang, T. Jia, Z. Sun, J. Qiu, and Z. Xu. Formation of long-and short-periodic nanoripples on stainless steel irradiated by femtosecond laser pulses. *Journal of Physics D: Applied Physics*, 44(50):505401, 2011.
- [32] J. Homola and J. Dostálek. *Surface plasmon resonance based sensors*, volume 4. Springer, 2006.
- [33] R.W. Wood. Xlii. on a remarkable case of uneven distribution of light in a diffraction grating spectrum. *The London, Edinburgh, and Dublin Philosophical Magazine and Journal of Science*, 4(21):396–402, 1902.
- [34] U. Fano. The theory of anomalous diffraction gratings and of quasi-stationary waves on metallic surfaces (sommerfeld’s waves). *JOSA*, 31(3):213–222, 1941.
- [35] R.B.M. Schasfoort and A.J. Tudos. *Handbook of surface plasmon resonance*. Royal Society of Chemistry Cambridge, UK, 2008.
- [36] Y. Han and S. Qu. The ripples and nanoparticles on silicon irradiated by femtosecond laser. *Chemical Physics Letters*, 495(4):241–244, 2010.
- [37] T.H. Her, R.J. Finlay, C. Wu, and E. Mazur. Femtosecond laser-induced formation of spikes on silicon. *Applied Physics A: Materials Science & Processing*, 70(4):383–385, 2000.
- [38] D.V. Tran, Y.C. Lam, H.Y. Zheng, V.M. Murukeshan, J.C. Chai, and D.E. Hardt. Femtosecond laser processing of crystalline silicon. 2005.
- [39] W.T. Silfvast. *Laser fundamentals*. Cambridge University Press, 2004.
- [40] J. Ion. *Laser processing of engineering materials: principles, procedure and industrial application*. Butterworth-Heinemann, 2005.
- [41] A. Miotello and P.M. Ossi. *Laser-surface interactions for new materials production*, volume 130. Springer, 2010.
- [42] Z. Guosheng, PM Fauchet, and AE Siegman. Growth of spontaneous periodic surface structures on solids during laser illumination. *Physical Review B*, 26(10):5366, 1982.
- [43] F. Ma, J. Yang, C. Liang, H. Wang, et al. Femtosecond laser-induced concentric ring microstructures on zr-based metallic glass. *Applied Surface Science*, 256(11):3653–3660, 2010.

- [44] W. Wang, G. Jiang, X. Mei, K. Wang, J. Shao, and C. Yang. Damage mechanism and morphology characteristics of chromium film in femtosecond laser rear-side ablation. *Applied Surface Science*, 256(11):3612–3617, 2010.
- [45] B. Tan and K. Venkatakrisnan. A femtosecond laser-induced periodical surface structure on crystalline silicon. *Journal of Micromechanics and Microengineering*, 16:1080, 2006.
- [46] X.C. Wang, G.C. Lim, F.L. Ng, W. Liu, and S.J. Chua. Femtosecond pulsed laser-induced periodic surface structures on gan/sapphire. *Applied Surface Science*, 252(5):1492 – 1497, 2005.
- [47] C. Momma, S. Nolte, B. N Chichkov, A. Tünnermann, et al. Precise laser ablation with ultrashort pulses. *Applied surface science*, 109:15–19, 1997.
- [48] J.A. Bittencourt. *Fundamentals of plasma physics*. Springer, 2004.
- [49] U. Schumacher. Basics of plasma physics. *Plasma Physics*, pages 1–20, 2005.
- [50] J. Bonse, S. Baudach, J. Krüger, W. Kautek, and M. Lenzner. Femtosecond laser ablation of silicon-modification thresholds and morphology. *Applied Physics A: Materials Science & Processing*, 74(1):19–25, 2002.
- [51] D.V. Tran, H.Y. Zheng, Y.C. Lam, V.M. Murukeshan, J.C. Chai, and D.E. Hardt. Femtosecond laser-induced damage morphologies of crystalline silicon by sub-threshold pulses. *Optics and Lasers in Engineering*, 43(9):977 – 986, 2005.
- [52] G. Germain, F. Morel, J.L. Lebrun, A. Morel, and B. Huneau. Effect of laser assistance machining on residual stress and fatigue strength for a bearing steel (100cr6) and a titanium alloy (ti 6al 4v). In *Materials science forum*, volume 524, pages 569–574. Trans Tech Publ, 2006.
- [53] R. Paschotta. *Encyclopedia of laser physics and technology: A-M*, volume 1. Wiley-VCH, 2008.
- [54] T. Himmer, A. Techel, S. Nowotny, and E. Beyer. Recent developments in metal laminated tooling by multiple laser processing. *Rapid prototyping journal*, 9(1):24–29, 2003.

- [55] C. Hitz, J. Ewing, and J. Hecht. *An Overview of Laser Technology*. John Wiley & Sons, Inc., 2012.
- [56] S. Schreck and K.H. Zum Gahr. Laser-assisted structuring of ceramic and steel surfaces for improving tribological properties. *Applied surface science*, 247(1-4):616–622, 2005.
- [57] A.F. Lasagni. *Advanced design of periodical structures by laser interference metallurgy in the micro/nano scale on macroscopic areas*. PhD thesis, Universitätsbibliothek, 2006.
- [58] M.H. Shamos. *Great experiments in physics: firsthand accounts from Galileo to Einstein*. Dover Pubns, 1987.
- [59] F. Yu. *Laser interference lithography: micropatterning of polymer surface for cell adhesion*. PhD thesis, Universitätsbibliothek, 2006.
- [60] S. Lu, H. Fujii, and K. Nogi. Marangoni convection and weld shape variations in *Ar-O₂* and *Ar-CO₂* shielded *GTA* welding. *Materials Science and Engineering: A*, 380(1):290–297, 2004.
- [61] Y. Lu, S. Theppakuttai, and SC Chen. Marangoni effect in nanosphere-enhanced laser nanopatterning of silicon. *Applied Physics Letters*, 82:4143, 2003.
- [62] M. Rombouts, J.P. Kruth, L. Froyen, and P. Mercelis. Fundamentals of selective laser melting of alloyed steel powders. *Cirp annals-manufacturing technology*, 55(1):187–192, 2006.
- [63] B.J. Keene. Review of data for the surface tension of iron and its binary alloys. *International materials reviews*, 33(1):1–37, 1988.
- [64] J. De Boor, N. Geyer, J.V. Wittemann, U. Gösele, and V. Schmidt. Sub-100 nm silicon nanowires by laser interference lithography and metal-assisted etching. *Nanotechnology*, 21:095302, 2010.
- [65] J.M. Park, K.S. Nalwa, W. Leung, K. Constant, S. Chaudhary, and K.M. Ho. Fabrication of metallic nanowires and nanoribbons using laser interference lithography and shadow lithography. *Nanotechnology*, 21:215301, 2010.
- [66] C.H. Liu, M.H. Hong, H.W. Cheung, F. Zhang, Z.Q. Huang, L.S. Tan, and T.S.A. Hor. Bimetallic structure fabricated by laser interference lithography for tuning surface plasmon resonance. *Optics Express*, 16(14):10701–10709, 2008.

- [67] T. Geldhauser, P. Leiderer, J. Boneberg, S. Walheim, and T. Schimmel. Generation of surface energy patterns by single pulse laser interference on self-assembled monolayers. *Langmuir*, 24(22):13155–13160, 2008.
- [68] M.K. Kelly, J. Rogg, CE Nebel, M. Stutzmann, and S. Kátai. High-resolution thermal processing of semiconductors using pulsed-laser interference patterning. *physica status solidi (a)*, 166(2):651–657, 1998.
- [69] C. Daniel, F. Mücklich, and Z. Liu. Periodical micro-nano-structuring of metallic surfaces by interfering laser beams. *Applied Surface Science*, 208-209(0):317 – 321, 2003. Physics and Chemistry of Advanced Laser Materials Processing.
- [70] Y. Fayou, Ping L., S Hao, M. Sanjay, C.M. Lehr, U. Bakowsky, and Mücklich. Laser interference lithography as a new and efficient technique for micropatterning of biopolymer surface. *Biomaterials*, 26(15):2307 – 2312, 2005.
- [71] M. Heintze, PV Santos, CE Nebel, and M. Stutzmann. Lateral structuring of silicon thin films by interference crystallization. *Applied physics letters*, 64(23):3148–3150, 1994.
- [72] F. Mücklich, A. Lasagni, and C. Daniel. Laser interference metallurgy—periodic surface patterning and formation of intermetallics. *Intermetallics*, 13(3-4):437 – 442, 2005. <ce:title>International Workshop on Ordered Intermetallics and Advanced Metallic Materials</ce:title>.
- [73] L. Zhongfan, X.K. Meng, T. Recktenwald, and F. Mücklich. Patterned intermetallic reaction of ni₃al by laser interference structuring. *Materials Science and Engineering: A*, 342(1-2):101 – 103, 2003.
- [74] X.K. Meng, H. Vehoff, and A.H.W. Ngan. Hard multilayered thin films of metal–intermetallic ni/ni₃al. 2000.
- [75] C. Daniel, A. Lasagni, and F. Mücklich. Stress and texture evolution of ni/al multi-film by laser interference irradiation. *Surface and Coatings Technology*, 180-181(0):478 – 482, 2004. Proceedings of Symposium G on Protective Coatings and Thin Films-03, of the E-MRS 2003 Spring Conference.
- [76] M. D’Alessandria and F. Mücklich. Tailoring the chemical behavior of aluminum for selective etching by laser interference metallurgy. *Applied Physics A: Materials Science & Processing*, 98(2):311–320, 2010.

- [77] M. Duarte, A. Lasagni, R. Giovanelli, J. Narciso, E. Louis, and F. Mücklich. Increasing lubricant film lifetime by grooving periodical patterns using laser interference metallurgy. *Advanced Engineering Materials*, 10(6):554–558, 2008.
- [78] B. Raillard, C. Gachot, M. Hans, P. Leibenguth, and F. Mücklich. Microstructural characterization of laser-irradiated bulk copper under dry sliding conditions. *Proceedings of the Institution of Mechanical Engineers, Part J: Journal of Engineering Tribology*, 2012.
- [79] T. Onda, S. Shibuichi, N. Satoh, and K. Tsujii. Super-water-repellent fractal surfaces. *Langmuir*, 12(9):2125–2127, 1996.
- [80] A.B.D. Cassie and S. Baxter. Wettability of porous surfaces. *Trans. Faraday Soc.*, 40:546–551, 1944.
- [81] R.N. Wenzel. Resistance of solid surfaces to wetting by water. *Industrial & Engineering Chemistry*, 28(8):988–994, 1936.
- [82] R.L. Hoffman. A study of the advancing interface. i. interface shape in liquid—gas systems. *Journal of Colloid and Interface Science*, 50(2):228–241, 1975.
- [83] P.G. de Gennes. Wetting: statics and dynamics. *Reviews of modern physics*, 57(3):827, 1985.
- [84] SG Mason. Wetting and spreading—some effects of surface roughness. *Wetting, Spreading, and Adhesion*, page 323, 1978.
- [85] J.C. Berg. *An introduction to interfaces & colloids: the bridge to nanoscience*. World Scientific Pub Co Inc, 2009.
- [86] S. Abbott, J. Ralston, G. Reynolds, and R. Hayes. Reversible wettability of photoresponsive pyrimidine-coated surfaces. *Langmuir*, 15(26):8923–8928, 1999.
- [87] J. Lahann, S. Mitragotri, T.N. Tran, H. Kaido, J. Sundaram, I.S. Choi, S. Hoffer, G.A. Somorjai, and R. Langer. A reversibly switching surface. *Science*, 299(5605):371, 2003.
- [88] K. Landry and N. Eustathopoulos. Dynamics of wetting in reactive metal/ceramic systems: linear spreading. *Acta materialia*, 44(10):3923–3932, 1996.

- [89] K. László, O. Czakkell, and E. Geissler. Wetting and non-wetting fluids in surface-functionalised activated carbons. *Colloid & Polymer Science*, 286(1):59–65, 2008.
- [90] J.F. Oliver and S.G. Mason. Liquid spreading on rough metal surfaces. *Journal of Materials Science*, 15(2):431–437, 1980.
- [91] E. Salek. *Handbook of Lubrication and Tribology: Theory and Design*, volume 2. CRC Press, 2012.
- [92] Liqui-Moly. Oil additives. Technical report, Liqui-Moly-Australia.
- [93] C. Yang and K. Leong. Influences of substrate wettability and liquid viscosity on isothermal spreading of liquid droplets on solid surfaces. *Experiments in fluids*, 33(5):728–731, 2002.
- [94] A.A. Keller, V. Broje, and K. Setty. Effect of advancing velocity and fluid viscosity on the dynamic contact angle of petroleum hydrocarbons. *Journal of Petroleum Science and Engineering*, 58(1-2):201–206, 2007.
- [95] BP. Versuchsöl *FVA 2*. Technical report, BP Oil Deutschland GmbH.
- [96] W.M. Haynes and D.R. Lide. *CRC Handbook of Chemistry and Physics: A Ready-Reference Book of Chemical and Physical Data*. CRC Handbook of Chemistry and Physics. Taylor & Francis Group, 2010.
- [97] M. Bigerelle and A. Iost. A numerical method to calculate the abbot parameters: A wear application. *Tribology international*, 40(9):1319–1334, 2007.
- [98] F. Müller, C. Zeitz, H. Mantz, K.H. Ehses, F. Soldera, J. Schmauch, M. Hannig, S. Huüfner, and K. Jacobs. Elemental depth profiling of fluoridated hydroxyapatite: Saving your dentition by the skin of your teeth? *Langmuir*, 2010.
- [99] D. Briggs and P. Seah. *Practical Surface Analysis: Auger and X-ray photoelectron spectroscopy*. Practical Surface Analysis. Wiley, 1990.
- [100] D.J. Larson, T.F. Kelly, Imago Scientific, and Instruments Corporation. Nanoscale analysis of materials using a local-electrode atom probe. *Microscopy and Microanalysis*, 20(3):59–62, 2006.
- [101] T.T. Tsong. Field ion image formation. *Surface Science*, 70(1):211–233, 1978.

- [102] B. Raillard, J. Remond, E. Ramos-Moore, N. Souza, C. Gachot, and F. Mücklich. Wetting properties of steel surfaces modified by laser interference metallurgy. *Advanced Engineering Materials*, 2012.
- [103] B. Raillard, L. Gouton, E. Ramos-Moore, S. Grandthyll, F. Müller, and F. Mücklich. Ablation effects of femtosecond laser functionalization on steel surfaces. *Surface and Coatings Technology*, 2012.
- [104] E.J. Abbott and F.A. Firestone. Specifying surface quality: a method based on accurate measurement and comparison. *Mechanical Engineering*, 55:569–572, 1933.
- [105] R. Zimmermann, P. Steiner, R. Claessen, F. Reinert, S. Hufner, P. Blaha, and P. Dufek. Electronic structure of 3d-transition-metal oxides: on-site coulomb repulsion versus covalency. *Journal of Physics: Condensed Matter*, 11:1657, 1999.
- [106] E. Ramos-Moore, P. Ferrari, D.E. Diaz-Droguett, D. Lederman, and JT Evans. Raman and x-ray photoelectron spectroscopy study of ferroelectric switching in *Pb (Nb, Zr, Ti) O₃* thin films. *Journal of Applied Physics*, 111(1):014108–014108, 2012.
- [107] P. Frantz and S.V. Didziulis. Detailed spectroscopic studies of oxygen on metal carbide surfaces. *Surface science*, 412:384–396, 1998.
- [108] J.P. Palmquist, J. Birch, and U. Jansson. Deposition of epitaxial ternary transition metal carbide films. *Thin solid films*, 405(1):122–128, 2002.
- [109] R.K. Raman, B. Gleeson, and D.J. Young. Laser raman spectroscopy: a technique for rapid characterisation of oxide scale layers. *Materials science and technology*, 14(5):373–376, 1998.
- [110] A.M. Turek, I.E. Wachs, and E. DeCanio. Acidic properties of alumina-supported metal oxide catalysts: an infrared spectroscopy study. *The Journal of Physical Chemistry*, 96(12):5000–5007, 1992.
- [111] Z. Zhou, IM Ross, WM Rainforth, and P.E. Hovsepian. Tracing c changes in a c/crc pvd coating using raman spectroscopy and eels. In *Journal of Physics: Conference Series*, volume 241, page 012108. IOP Publishing, 2010.

- [112] Y.N. Kok, P.E. Hovsepian, R. Haasch, and I. Petrov. Raman spectroscopy study of c/cr coatings deposited by the combined steered cathodic arc/unbalanced magnetron sputtering technique. *Surface and Coatings Technology*, 200(1):1117–1122, 2005.
- [113] B.M. Weckhuysen and I.E. Wachs. Raman spectroscopy of supported chromium oxide catalysts. determination of chromium—oxygen bond distances and bond orders. *J. Chem. Soc., Faraday Trans.*, 92(11):1969–1973, 1996.
- [114] K. Toriumi and Y. Saito. Electron-density distribution in crystals of K_2CrO_4 . *Acta Crystallographica Section B: Structural Crystallography and Crystal Chemistry*, 34(11):3149–3156, 1978.
- [115] D. Blum, MT Averbuch-Pouchot, and JC Guitel. Un nouvel exemple d'anion du type $[\text{XCr}_2\text{O}_{10}](\text{x} = \text{As})$. structure de $\text{BaH}[\text{AsCr}_2\text{O}_{10}]$. *Acta Crystallographica Section B: Structural Crystallography and Crystal Chemistry*, 35(3):726–727, 1979.
- [116] F. Tuinstra and J.L. Koenig. Raman spectrum of graphite. *The Journal of Chemical Physics*, 53:1126, 1970.
- [117] D.S. Knight, R. Weimer, L. Pilione, and W.B. White. Surface-enhanced raman spectroscopy of chemical vapor deposited diamond films. *Applied physics letters*, 56(14):1320–1322, 1990.
- [118] B. Marcus, L. Fayette, M. Mermoux, L. Abello, and G. Lucazeau. Analysis of the structure of multi-component carbon films by resonant raman scattering. *Journal of applied physics*, 76(6):3463–3470, 1994.
- [119] E. Park, O. Ostrovski, J. Zhang, S. Thomson, and R. Howe. Characterization of phases formed in the iron carbide process by x-ray diffraction, mossbauer, x-ray photoelectron spectroscopy, and raman spectroscopy analyses. *Metallurgical and materials Transactions B*, 32(5):839–845, 2001.
- [120] D. Roy, ZH Barber, and TW Clyne. Ag nanoparticle induced surface enhanced raman spectroscopy of chemical vapor deposition diamond thin films prepared by hot filament chemical vapor deposition. *Journal of applied physics*, 91:6085, 2002.
- [121] A.N. Obraztsov, M.A. Timofeyev, M.B. Guseva, V.G. Babaev, Z.K. Valiullova, and V.M. Babina. Comparative study of microcrystalline diamond. *Diamond and related materials*, 4(7):968–971, 1995.

- [122] P. Guillory and T.O. Deschaines. *Raman Mapping of Single-walled Carbon Nanotube Distribution on Phase Separated Polystyrene and Polymethylmethacrylate*.
- [123] M.K. Miller and R.G. Forbes. Atom probe tomography. *Materials Characterization*, 60(6):461–469, 2009.
- [124] O. Dmitrieva, D. Ponge, G. Inden, J. Millán, P. Choi, J. Sietsma, and D. Raabe. Chemical gradients across phase boundaries between martensite and austenite in steel studied by atom probe tomography and simulation. *Acta Materialia*, 59(1):364–374, 2011.
- [125] S. Lozano-Perez, D.W. Saxey, T. Yamada, and T. Terachi. Atom-probe tomography characterization of the oxidation of stainless steel. *Scripta Materialia*, 62(11):855–858, 2010.
- [126] M. Bachhav, R. Danoix, F. Danoix, B. Hannoyer, S. Ogale, and F. Vurpillot. Investigation of *Wüstite* ($Fe_{1-x}O$) by femtosecond laser assisted atom probe tomography. *Ultramicroscopy*, 111(6):584–588, 2011.
- [127] M. Ngamo, S. Duguay, P. Pichler, K. Daoud, and P. Pareige. Characterization of arsenic segregation at Si/SiO_2 interface by 3d atom probe tomography. *Thin solid films*, 518(9):2402–2405, 2010.
- [128] Y.M. Chen, T. Ohkubo, and K. Hono. Laser assisted field evaporation of oxides in atom probe analysis. *Ultramicroscopy*, 111(6):562–566, 2011.
- [129] R. Lardé, E. Talbot, F. Vurpillot, P. Pareige, G. Schmerber, E. Beaurepaire, A. Dinia, and V. Pierron-Bohnes. Investigation at the atomic scale of the co spatial distribution in Zn (Co) on magnetic semiconductor oxide. *Journal of Applied Physics*, 105(12):126107–126107, 2009.
- [130] L. Yao, B. Gault, JM Cairney, and SP Ringer. On the multiplicity of field evaporation events in atom probe: A new dimension to the analysis of mass spectra. *Philosophical Magazine Letters*, 90(2):121–129, 2010.
- [131] F. De Geuser, B. Gault, A. Bostel, and F. Vurpillot. Correlated field evaporation as seen by atom probe tomography. *Surface science*, 601(2):536–543, 2007.
- [132] D. Hudson, A. Cerezo, and G.D.W. Smith. Zirconium oxidation on the atomic scale. *Ultramicroscopy*, 109(5):667–671, 2009.

- [133] M.K. Miller. Atom probe tomography. *Handbook of Microscopy for Nanotechnology*, pages 227–246, 2005.
- [134] J. Angseryd, F. Liu, H.O. Andrén, S.S.A. Gerstl, and M. Thuvander. Quantitative apt analysis of ti (c, n). *Ultramicroscopy*, 111(6):609–614, 2011.
- [135] P Bas, A Bostel, B Deconihout, and D Blavette. A general protocol for the reconstruction of 3d atom probe data. *Applied Surface Science*, 87:298–304, 1995.
- [136] D.R. Kingham. The post-ionization of field evaporated ions: A theoretical explanation of multiple charge states. *Surface Science*, 116(2):273–301, 1982.
- [137] *Absorptivity of CW CO₂, CO and YAG-laser beams by different metallic alloys*, 1990.
- [138] L.K. Ang, Y.Y. Lau, R.M. Gilgenbach, and H.L. Spindler. Analysis of laser absorption on a rough metal surface. *Applied physics letters*, 70:696, 1997.
- [139] X.Y. Tan, D.M. Zhang, F. Mao, Z.H. Li, D. Yi, and X.Z. Zhang. Theoretical and experimental study of energy transportation and accumulation in femtosecond laser ablation on metals. *Transactions of Non-ferrous Metals Society of China*, 19(6):1645–1650, 2009.
- [140] B.R. Tull, J.E. Carey, E. Mazur, J.P. McDonald, and S.M. Yalisove. Silicon surface morphologies after femtosecond laser irradiation. *MRS bulletin*, 31(08):626–633, 2006.
- [141] D. Bäuerle. *Laser processing and chemistry*. Springer Verlag, 2011.
- [142] R. Hohenstein, S.E. Kirkwood, R. Fedosejevs, and Y.Y. Tsui. Simulation of femtosecond laser ablation of silicon. volume 5579, pages 688–695. SPIE, 2004.
- [143] N.F. Mott. The theory of the formation of protective oxide films on metals.—iii. *Trans. Faraday Soc.*, 43(0):429–434, 1947.
- [144] N. Cabrera and N.F. Mott. Theory of the oxidation of metals. *Reports on Progress in Physics*, 12:163, 1949.
- [145] A.M. Kietzig, S.G. Hatzikiriakos, and P. Englezos. Patterned superhydrophobic metallic surfaces. *Langmuir*, 25(8):4821–4827, 2009.

- [146] L. Pauling. Atomic radii and interatomic distances in metals. *Journal of the American Chemical Society*, 69(3):542–553, 1947.
- [147] G. Roberts. Femtosecond chemical reactions. *Philosophical Transactions of the Royal Society of London. Series A: Mathematical, Physical and Engineering Sciences*, 358(1766):345–366, 2000.
- [148] D.H. Shin, B.C. Kim, Y.S. Kim, and K.T. Park. Microstructural evolution in a commercial low carbon steel by equal channel angular pressing. *Acta materialia*, 48(9):2247–2255, 2000.
- [149] E. Detemple, P. Leibenguth, C. Gachot, and F. Mücklich. Large-area patterned formation of intermetallic phases on ti/al multilayer systems by laser interference metallurgy. *Thin Solid Films*, 519(2):736–741, 2010.
- [150] M. Callies, Y. Chen, F. Marty, A. Pépin, and D. Quéré. Microfabricated textured surfaces for super-hydrophobicity investigations. *Microelectronic engineering*, 78:100–105, 2005.
- [151] W. Lee, B.G. Park, D.H. Kim, D.J. Ahn, Y. Park, S.H. Lee, and K.B. Lee. Nanostructure-dependent water-droplet adhesiveness change in superhydrophobic anodic aluminum oxide surfaces: From highly adhesive to self-cleanable. *Langmuir*, 26(3):1412–1415, 2009.
- [152] RG Cox. The spreading of a liquid on a rough solid surface. *Journal of Fluid Mechanics*, 131(1):1–26, 1983.
- [153] R. Shuttleworth and G.L.J. Bailey. The spreading of a liquid over a rough solid. *Discussions of the Faraday Society*, 3:16–22, 1948.
- [154] J.F. Oliver, C. Huh, and S.G. Mason. The apparent contact angle of liquids on finely-grooved solid surfaces—a sem study. *The Journal of Adhesion*, 8(3):223–234, 1976.
- [155] R.J. Good. A thermodynamic derivation of wenzel’s modification of young’s equation for contact angles; together with a theory of hysteresis1. *Journal of the American Chemical Society*, 74(20):5041–5042, 1952.
- [156] J.F. Oliver, C. Huh, and S.G. Mason. Resistance to spreading of liquids by sharp edges. *Journal of Colloid and Interface Science*, 59(3):568–581, 1977.

- [157] M. Koç and J. Ni. Experimental and numerical investigations on microcoining of stainless steel 304. *Ann Arbor*, 1001:48109, 2008.
- [158] R. Badji, B. Bacroix, and M. Bouabdallah. Texture, microstructure and anisotropic properties in annealed 2205 duplex stainless steel welds. *Materials Characterization*, 62(9):833–843, 2011.